GENERALIZED CRITICAL POINTS ANALYSIS OF ACETYLENE VIBRATIONAL DYNAMICS

by

XINLI DING

A DISSERTATION

Presented to the Department of Chemistry
and the Graduate School of the University of Oregon
in partial fulfillment of the requirements
for the degree of
Doctor of Philosophy

March 2004

"Generalized Critical Points Analysis of Acetylene Vibrational Dynamics", a dissertation prepared by Xinli Ding in partial fulfillment of the requirements for the Doctor of Philosophy degree in the Department of Chemistry. This dissertation has been approved and accepted by:

Dr. Jeffrey A. Cina, Chair of the Examining Committee

Dr. Michael E. Kellman, Advisor of the Examining Committee

Date

Committee in charge:
Dr. Jeffrey A. Cina, Chair
Dr. Michael E. Kellman, Advisor
Dr. David R. Herrick
Dr. Michael M. Haley
Dr. Jens U. Nöckel

Accepted by:

Dean of the Graduate School

An Abstract of the Dissertation of

Xinli Ding for the degree of Doctor of Philosophy

in the Department of Chemistry to be taken March 2004

Title: GENERALIZED CRITICAL POINTS ANALYSIS OF ACETYLENE VIBRATIONAL DYNAMICS

Approved: _____

Dr. Jeffrey A. Cina

Classical tools of nonlinear dynamics are used to study the highly excited vibrations of small molecules. For effective Hamiltonians with one polyad number (approximate constant of motion), previously developed methods locate new anharmonic modes using the critical points in the reduced classical phase space. Theoretical arguments are given for generalizing the method to more than one polyad number. As the simplest classical invariant structure, critical points of the reduced phase space are solved analytically without relying on either integrating trajectories or visual inspection. These critical points, especially those that are linearly stable, are expected to indicate regions with the same type of classical dynamics as well as quantum modes of vibration.

The pure bending Hamiltonian of acetylene (C_2H_2) is analyzed to demon-

strate the effectiveness of critical points analysis. Four families of critical points are born in distinct bifurcations, each corresponding to a novel anharmonic mode. These modes are visualized with custom computer-generated animations. Their origin and nature are qualitatively explained through separate consideration of DD-I and ℓ resonance alone. Quantum survival probability verifies that the Local and Counter Rotator modes are the stable modes of vibration at high excitation.

The same analysis is extended for the first time to the acetylene stretch-bend system, which has never been analyzed classically with all the resonance couplings. Preliminary results are obtained for the polyad series containing the C-H stretch overtones. The local C-H stretch critical points family, induced by the stretch-stretch ($K_{11/33}$) resonance, is located and shown to bifurcate into at least 4 new families when the stretch-bend resonances are included. The new families indicate that the mixing between the stretch and bend may result in novel vibrational modes.

This dissertation includes my previously co-authored materials.

CURRICULUM VITA

NAME OF AUTHOR: Xinli Ding

GRADUATE AND UNDERGRADUATE SCHOOLS ATTENDED:

University of Oregon
Peking University, Beijing, China

DEGREES AWARDED:

Doctor of Philosophy in Chemistry, 2003, University of Oregon
Bachelor of Science in Chemistry, 1997, Peking University

AREAS OF SPECIAL INTEREST:

Nonlinear Dynamics
Chemical Physics
Computer Aided Visualization

PROFESSIONAL EXPERIENCE:

Research Assistant, Department of Chemistry, University of Oregon, Eugene, 1997-2003

Teaching Assistant, Department of Chemistry, University of Oregon, Eugene, 1997-1998

PUBLICATIONS:

[1] Y. Shuangbo, V. Tyng, and M.E. Kellman. Spectral patterns of isomerizing systems. *J. Phys. Chem. A.*, 112:4162, 2003.

[2] M.E. Kellman, M.W. Dow, and V. Tyng. Dressed basis for highly excited molecular vibrations. *J. Chem. Phys.*, 118:9519, 2003.

[3] J.F. Svitak, V. Tyng, and M.E. Kellman. Bifurcation analysis of higher m:n resonance spectroscopic Hamiltonian. *J. Chem. Phys.*, 106:10797, 2002.

[4] M.E. Kellman and V. Tyng. Bifurcation effects in coupled Bose-Einstein condensates. *Phys. Rev. A*, 66:013602/1, 2002.

[5] C. Zhou, D. Xie, R. Chen, G. Yan, H. Guo, V. Tyng, and M.E. Kellman. Quantum calculation of highly excited vibrational energy levels of CS_2 ($\tilde{X}$) on a new empirical potential energy surface and semiclassical analysis of 1:2 Fermi resonance. *Spectro. Acta. A*, 58A:727, 2002.

[6] M.E. Kellman, J.P. Rose, and V. Tyng. Spectral patterns and ultrafast dynamics in planar acetylene. *European Physical Journal D*, 14:225, 2001.

[7] M. Joyeux, D. Sugny, V. Tyng, M.E. Kellman, H. Ishikawa, R.W. Field, C. Beck, and R.Schinke. Semiclassical study of the isomerization states of HCP. *J. Chem.Phys.*, 112:4162, 2000.

GLOSSARY

DOF	.....	Degrees of Freedom
IVR	.....	Intramolecular Vibrational Redistribution
PES	.....	Potential Energy Surface
PO	.....	Periodic Orbit
PPS	.....	Polyad Phase Sphere
RRKM	.....	Rice-Ramsperger-Kassel-Marcus model
SOS	.....	Surface of Section
ZOS	.....	Zero-Order States

TABLE OF CONTENTS

LIST OF FIGURES

LIST OF TABLES

CHAPTER I

INTRODUCTION

1.1 Molecular Dynamics Encoded In Spectra

In its earlier years, spectroscopy was an important tool in the structure determination of molecules. Today, the equilibrium structure, as well as the spectroscopic constants, continues to be actively pursued. Moreover, the accumulated theory, techniques and data have also enabled researchers to use spectroscopy as a probe of dynamical processes, such as collisions, energy transfer, and chemical reactions.

The question is how to decode dynamical information from the resulting spectra. Spectra recorded in either frequency domain or time domain should reflect the same physical behavior. These domains are formally connected by a Fourier transform [1]. Electromagnetic radiation affects molecules on at least four levels in the order of increasing energy: the nuclear spin, rotational, vibrational and electronic *degrees of freedom* (DOF). The interactions among even these four levels within a molecule make it nontrivial to analyze the total dynamics. The focus of this thesis is the vibrational dynamics of small polyatomic (3-4 atoms)

molecules. We are not implying that other DOF are unimportant or irrelevant. For chemists, however, the vibrational DOF are of special interest since they are closely related to chemical reaction processes.

1.2 Modes of Vibration

We start with the frequency-domain spectra. Each resolved level in the spectra corresponds to one quantum eigenstate of the molecular Hamiltonian. The decoding of dynamics involves assignment of these levels with *quantum numbers* corresponding to their modes of vibration. The word "mode" has been rather liberally used to designate patterns in vibrations. The conventional meaning is that there are certain coordinates in which the vibration appears particularly simple. Especially it refers to the case when the vibration can be separated into independent oscillations in these coordinates. Such a separation is crucial for comprehending molecular vibrations that may be too complex to be directly visualized. Therefore, mode designation is more than mere labeling because it reflects the pattern of underlying dynamics.

A well-known case is the *normal modes*. When the amplitudes of vibration remain small, forces among atoms can be approximated as harmonic, i.e. proportional to the displacement from equilibrium configuration. Diagonalization of the resulting force constant matrix yields $3N-6$ (or $3N-5$ for linear molecules) normal mode coordinates, N being the number of atoms in the molecule [2]. The

classical motion of the atoms (determined by Newtonian mechanics) is decomposable into oscillations along these normal mode coordinates with characteristic frequencies. In the quantum system, the nodes of the corresponding eigenstates are aligned along these same coordinates. A set of normal mode quantum numbers can be assigned from counting these nodes.

At higher energy, as the vibrational amplitudes increase, inter-atomic forces deviate from the harmonic approximation. This requires the inclusion of additional terms, such as anharmonicity and resonance couplings. The former distorts the normal modes, while the latter not only distort but also mix them. Eventually, the mixing would become so extensive that the normal mode picture ceases to be a valid approximation.

It is believed that at *sufficiently* high energy, the vibrational dynamics enters the "bag of atoms" regime [3], which is characterized by a total lack of regular modes. In practice, however, this may not be easily attained. In at least some and perhaps most molecules, the spectra turn out to be regular even when the normal modes break down. The dynamics are then encoded in other new modes of vibration. For example, in H_2O [4] and O_3 [5], the stretching states exhibit a transition from normal to *local mode* behavior as the energy of excitation is increased. In Fig. 1.1, the normal symmetric and anti-symmetric modes have two A-B bonds vibrate in synchronization, while in the local mode only one A-B bond is vibrating. Eigenstates in this regime appear as separable in the

local mode coordinates. Here the local mode is not just another way to describe the molecule, but a special one that directly reflects the underlying dynamics. More exotic modes, such as the "precessional" mode [6] and more complicated collective motions [7], are also known to exist.

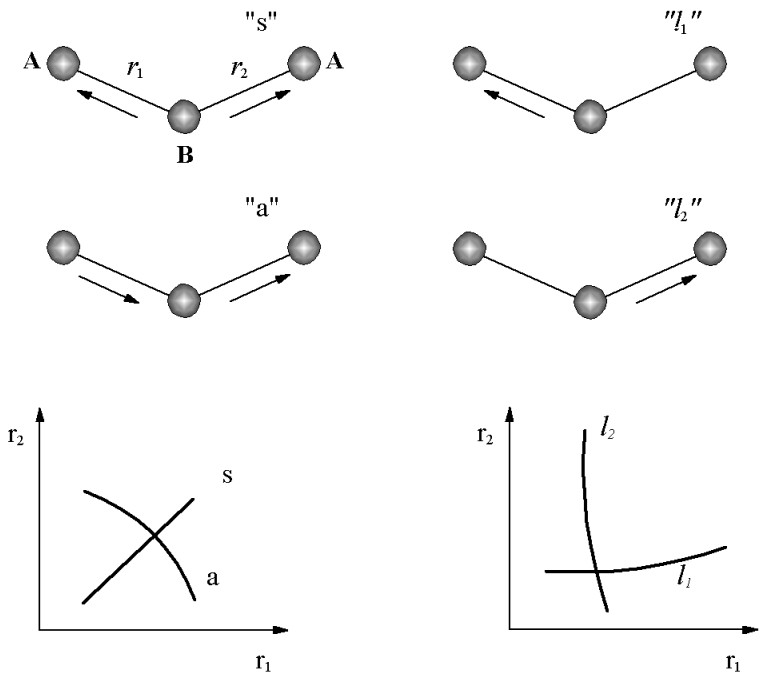

FIGURE 1.1 Normal and local stretching modes in an ABA molecule. In the normal symmetric ("s") and antisymmetric ("a") modes, the two A-B bonds vibrate in concert. In contrast, the local modes 1 ("ℓ_1") and 2 ("ℓ_2") have most vibrational amplitude in only one bond.

These vibrational modes strongly influence the molecules' chemical behavior. When a molecule is between collisions and free of other external interactions, its intrinsic reaction rate, if one exists, is determined by the flow of vibrational energy within the molecule, a process termed *Intramolecular Vibrational Relaxation*

(IVR) [3,8]. The complete characterization of IVR requires a "map" of all possible paths of energy flow. Yet, in actual modeling of reactions, such a detailed description is often simplified into a statistical treatment. A most popular assumption is the *Rice-Ramsperger-Kassel-Marcus* (RRKM) model, which assumes unrestricted IVR flow among all vibrational DOF [9]. This model is assumed increasingly valid at high internal energy and coupling (the "bag of atoms" limit). The corresponding classical dynamics is chaotic [10].

In contrast, energy in a stable mode remains trapped in a small part of the energetically accessible phase space. If the molecule has a significant probability of getting into these trapped regions, IVR flow would be restricted. One then has to be cautious about using a statistical model. These stable modes may be of great use in coherently controlling chemical reactions [11] because excitation energy may remain in these modes long enough for optical manipulation.

Since the famous Fermi-Ulam-Pasta simulation in 1953 [12], molecular systems have served as an application for the mathematical theory of nonlinear dynamics, and a motivation for its continued development. The past 50 years has seen an increasing interest in applying classical nonlinear mechanics in studying dynamics in microscopic systems.

1.3 Overview of Thesis Structure

The identification and assignment of vibrational modes are crucial for analyzing the spectra of highly excited molecules. For over a decade, the Kellman group has been using the mathematical tools of bifurcation [13] and catastrophe theory [14] in analyzing classical and quantum dynamics in the vibration of small molecules. The group developed the method of critical points analysis in order to uncover the nonlinear, anharmonic modes at high excitation via analytical detection (as opposed to numerical search). Its earliest formulation aims at classifying the dynamics in a two-oscillator-single-resonance system (which is integrable) according to the critical point(s) in its reduced classical phase space [15]. This was later extended to the *large-scale bifurcation analysis* that considers coupled 3-oscillator systems that are nonintegrable [16]. These two methods are reviewed in references [17,18]. This thesis is a further generalization that takes into account Hamiltonians with multiple polyad numbers, as well as providing a more solid mathematical foundation to the method. The pure bending acetylene (C_2H_2) system is used as a chemically significant test case.

Chapter 2 reviews the relevant background information: the effective quantum Hamiltonian and polyads, basic tools in classical mechanics, and topics on the quantum-classical correspondence.

Chapter 3 first describes existing procedures of critical points analysis for treating integrable and nonintegrable systems with one polyad number. Then

general discussions are given regarding the behavior of critical points, including the novel complexity introduced by multiple polyad numbers.

Chapter 4 applies the bifurcation analysis to C_2H_2 pure bending system (2 polyad numbers). The analysis reveals the existence of new families of critical points, born in bifurcations at increasing energy. The result is compared to those from the separate consideration of single resonances, giving a qualitative description of the nature of the new critical points. The stable families of critical points correspond to stable quantum modes of vibration. Additional interpretation is given

Chapter 5 extends the analysis to the stretch-bend acetylene system including all the resonances. The fate of the C-H normal stretch modes is considered under increasing excitation. The preliminary result suggest that a chain of bifurcations first create a local C-H stretch mode which then bifurcate into complex stretch-bend modes.

Chapter 6 summarizes contributions made in this thesis, and discusses possible future directions of research.

CHAPTER II

BACKGROUND INFORMATION

2.1 Effective Quantum Hamiltonian and Polyads

In this thesis, vibrational dynamics is modeled by an effective Hamiltonian obtained from fitting spectral levels [1]. The general form of an effective Hamiltonian is

$$\hat{H}_{eff} = \hbar\hat{H}_0 + \sum \hat{V}_2^{ij} + \sum \hat{V}_3^{ijk} + ... \tag{2.1}$$

$\hbar = 1$ unless stated otherwise.

$$\hat{H}_0 = \sum_i \omega_i \left(\hat{n}_i + \frac{d_i}{2}\right) + \sum_{i,j;i\leq j} x_{ij} \left(\hat{n}_i + \frac{d_i}{2}\right)\left(\hat{n}_j + \frac{d_j}{2}\right) + \cdots \tag{2.2}$$

$$\hat{V}_2^{ij} = V_{ij}[(\hat{a}_i^\dagger)^m(\hat{a}_j)^n + (\hat{a}_j^\dagger)^n(\hat{a}_i)^m] \tag{2.3}$$

$$\hat{V}_3^{ijk} = V_{ijk}[(\hat{a}_i^\dagger)^m(\hat{a}_j)^n(\hat{a}_k)^p + (\hat{a}_j^\dagger)^n(\hat{a}_k^\dagger)^p(\hat{a}_i)^m] \tag{2.4}$$

The zero-order part $\hat{H}_0$ is in the form of a Dunham expansion. $\hat{n}_i$ is a zero-order (e.g. normal or local) mode number operator whose eigenvalue is n_i.

[1] The fit is to either the resolved experimental spectra or the spectra from theoretical calculations [19].

d_i is the degeneracy of mode i: 1 for non-degenerate modes and 2 for doubly degenerate modes such as the bending of a linear molecule. Each $\hat{V}_2^{i,j}$ term in eqn. (2.1) represents a resonance that couples the i and j modes. It exchanges m quanta in mode i and n quanta in mode j. $\hat{V}_3^{i,j,k}$ acts in a similar manner among three modes i, j and k.

The operators $\hat{a}_i^\dagger$, $\hat{a}_i$ have matrix elements identical to those of harmonic raising and lowering operators, i.e.

$$\hat{a}_i^\dagger |n_i\rangle = \sqrt{n_i + 1}\, |n_i + 1\rangle \tag{2.5}$$

$$\hat{a}_i |n_i\rangle = \sqrt{n_i}\, |n_i - 1\rangle \tag{2.6}$$

$$\hat{a}_i^\dagger \hat{a}_i |n_i\rangle = \hat{n}_i |n_i\rangle = n_i\, |n_i\rangle \tag{2.7}$$

The $|n_1, n_2, \cdots, n_N\rangle$ comprise a set of eigenstates of $\hat{H}_0$. They are referred to as *Zero Order States* (ZOS). In this basis, the matrix form of $\hat{H}_{eff}$ is obtained from eqns. (2.5,2.6). Diagonalization of this matrix yields quantum eigenfunctions in terms of the ZOS. In order to compare these eigenfunctions to the molecular coordinate space (such as bond length and angle), one needs to assume an oscillator model for each n_i. For example, this representation could be taken as that of a harmonic [20] or Morse [21] oscillator.

The resonance coupling terms $\hat{V}$ cause the ZOS to mix the eigenfunctions. The quantum numbers n_i then are no longer good quantum numbers. However, certain linear combinations of them, known as the *polyad numbers*, may remain

conserved in the fitting Hamiltonian (and approximately conserved in the exact molecular Hamiltonian). In ABA-type triatomic molecules like H_2O, there is often an approximate 2:1 frequency ratio between one of the two normal stretching modes n_1 and the bending n_2 [22], leading to the inclusion of a *Fermi resonance* term in $\hat{H}_{eff}$. The resonance either (1) takes out one quantum of n_1 and adds two quanta of n_2, or (2) takes out two quanta of n_2 and adds one quantum of n_1. Meanwhile, the other non-interacting stretching normal mode n_3 can be regarded as a "spectator". Because the number of quanta in it is constant, it is absorbed into the other parameters when we only consider a specific n_3 manifold. When the stationary configuration of the molecule is non-linear, the bending n_2 mode is singly degenerate ($d_2 = 1$). The effective two-mode Hamiltonian is

$$\begin{aligned}\hat{H}_{Fermi} =&\omega_1(\hat{n}_1 + \frac{1}{2}) + \omega_2(\hat{n}_2 + \frac{1}{2}) + x_{11}(\hat{n}_1 + \frac{1}{2})^2 + x_{12}(\hat{n}_1 + \frac{1}{2})(\hat{n}_2 + \frac{1}{2}) \\ &+ x_{22}(\hat{n}_2 + \frac{1}{2})^2 + V_{Fermi}[\hat{a}_1^\dagger(\hat{a}_2)^2 + (\hat{a}_2^\dagger)^2\hat{a}_1]\end{aligned} \tag{2.8}$$

The polyad number

$$\hat{P} = 2\hat{n}_1 + \hat{n}_2 \tag{2.9}$$

remains conserved since it commutes with the Hamiltonian

$$[\hat{P}, \hat{H}_F] = \hat{P}\hat{H}_F - \hat{H}_F\hat{P} = 0 \tag{2.10}$$

In the quantum Hamiltonian, the presence of $\hat{P}$ means that the resonance coupling only couples ZOS with the same polyad number. For example, there

are four ZOS (n_1, n_2) interacting within $P = 3$:

$$(3,0) \leftrightarrow (2,2) \leftrightarrow (1,4) \leftrightarrow (0,6)$$

and states belong to the same polyad appear in clusters in the spectra, as illustrated in Fig. 2.1. Experimentally, it is often the observation of such clustering that leads to the adoption of a polyad model [23].

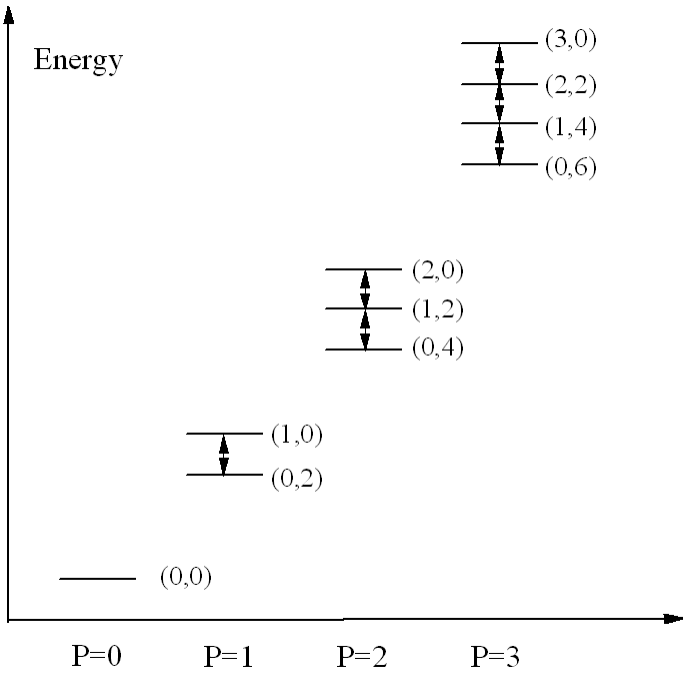

FIGURE 2.1 Schematic illustration of polyad structure in spectra. The states with the same polyad number P are clustered together, while the energy spacing between different polyads is relatively large.

Since there is no coupling between two polyads, the Hamiltonian matrix is block-diagonal and the intra-polyad couplings are confined to the polyad blocks.

The blocks can be individually diagonalized, substantially reducing the amount of computation. In the time domain, the existence of polyad(s) imposes an approximate restriction on the energy flow: IVR only happens within the same polyad [24].

Kellman devised a systematic method to locate polyad numbers [25]. The method is closely related to an earlier van Vleck perturbation study by Fried and Ezra [26]. Suppose there are N zero-order vibrational modes, excluding the spectator ones. Each resonance term in $\hat{H}_{eff}$ is represented by a *resonance vector* in the N-dimensional linear space $\{n_1, n_2, \cdots n_N\}$. All the resonance vectors $\vec{V}_i$ form a linear subspace with M dimensions ($M \leq N$). Orthogonal to this subspace is another $(N-M)$-dimensional subspace from which the $(N-M)$ polyad numbers are found. The coefficients in the polyad number are determined by the set of linearly independent vectors $\vec{P}_j$ which span the subspace orthogonal to the resonance vectors. This is graphically illustrated in Fig. 2.2 for $N = 3, M = 2$. In the Fermi resonance system, the resonance vector $\vec{V}_F = \{1, -2\}$ gives the polyad number $P = 2n_1 + n_2$, in accordance with the orthogonal vector $\vec{P} = \{2, 1\}$.

Although the total number of polyad numbers is fixed, each of them is not uniquely defined. There is the liberty of multiplying the coefficients by a factor or linearly combining two polyad numbers vectors. The usual choice is to match them to the approximate integer ratio among the zero-order mode frequencies.

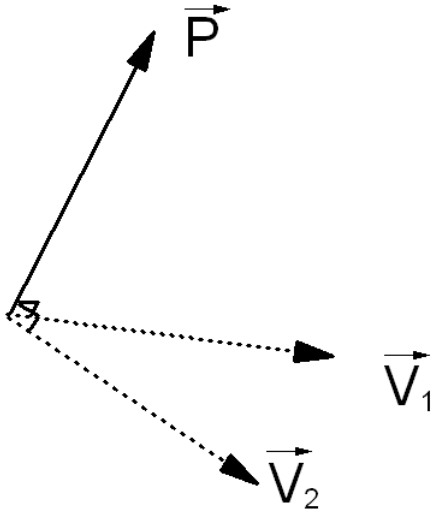

FIGURE 2.2 Schematic illustration of the method to locate polyad number(s), adapted from Fig. 1 of [18] with changes.

These integer ratios lead to the inclusion of the respective resonance terms in $\hat{H}_{eff}$ [27]. In eqn. (2.8), $\omega_1 : \omega_2 \approx 2 : 1$, so $P = 2n_1 + n_2$.

The effective Hamiltonian can be constructed from the more comprehensive Potential Energy Surface (PES) using perturbative methods [28,29]. However, the effective Hamiltonian obtained from fitting experimental data is not only a more reliable model for the highly excited states in triatomic or larger molecules, but also easily gives the useful insight of the polyad structure. The conservation of polyad numbers is never exact, though, due to additional small couplings in the PES. The degree of their conservation can be estimated by the uncertainty relationship $\Delta E \cdot \Delta t \geq \hbar$. Spectral data recorded at relatively low frequency (larger ΔE) decodes dynamics at shorter timescale (smaller δt), and vice versa. In molecules such as acetylene, it has been observed that spectral peaks well-described

by a polyad Hamiltonian may break into finer structures when scrutinized at high frequency resolution. This is caused by the smaller couplings not included in the effective Hamiltonian (and likely to break the polyad number), which exercise their effect at longer time scales [30]. As an example, the C_2H_2 pure bending Hamiltonian of Chapter 4 is fitted to spectra recorded with a maximum of 2 cm^{-1} resolution. The corresponding uncertainty $\Delta t = 2.6$ picosecond is much longer than the bending vibration period (50 femtoseconds). Since the polyad structure is still present at this time scale, the polyad numbers predicted from the effective Hamiltonian can be assumed valid at the same time scale or longer.

2.2 Basic Concepts in Classical Mechanics

Although microscopic systems are governed by quantum mechanics, classical mechanics continues to be an important tool in understanding molecular dynamics. There are both fundamental and empirical and reasons: (1) Quantum mechanics is built upon classical mechanics, rather than being a self-consistent theory. The real behavior of the molecules may be derived through semiclassical methods, which is a bridge between the quantum and classical worlds. (2) To the human researcher, classical mechanics proves to be a more intuitive tool in understanding the microscopic phenomena. (3) In large and/or highly excited systems, treating the whole system quantum mechanically can be challenging. Classical and semiclassical methods thus become useful supplements.

Below we discuss some basic concepts in classical mechanics that are pertinent to the central topic in this thesis. The reader is referred to Tabor [31] for a general introduction to classical mechanics with emphasis on the nonlinear dynamics. The textbook by Goldstein [32] may serve as a more comprehensive reference.

2.2.1 Heisenberg's Correspondence Principle

Heisenberg's Correspondence Principle [33] provides an important connection between the quantum and classical worlds. It relates raising and lowering operators in quantum mechanics to Fourier components of the action-angle variables in classical mechanics [34]:

$$\begin{aligned} \hat{a}_i^\dagger &\to \sqrt{n_i + \frac{d_i}{2}} e^{i\phi_i} = \sqrt{I_i} e^{i\phi_i} \\ \hat{a}_i &\to \sqrt{n_i + \frac{d_i}{2}} e^{-i\phi_i} = \sqrt{I_i} e^{-i\phi_i} \end{aligned} \tag{2.11}$$

The N-mode quantum Hamiltonian $\hat{H}_{eff}$ is mapped to an N DOF classical Hamiltonian in canonical variables (I_i, ϕ_i). The n_i terms in H_0 transform as

$$I_i = n_i + \frac{d_i}{2} \tag{2.12}$$

Substitution of eqn. (2.11) into (2.8) gives

$$H_F = \omega_1 I_1 + \omega_2 I_2 + x_{11} I_1^2 + x_{12} I_1 I_2 + x_{22} I_2^2 + 2V_{Fermi} \sqrt{I_1^2 I_2} \cos[\phi_1 - 2\phi_2] \tag{2.13}$$

2.2.2 Hamiltonian Classical Dynamics

The (I_i, ϕ_i) variables form a set of canonically conjugate coordinates in Hamiltonian mechanics. Their time evolution (also known as equations of motion) has the elegant form

$$\dot{I}_i = \frac{dI_i}{dt} = -\frac{\partial H}{\partial \phi_i} \tag{2.14}$$

$$\dot{\phi}_i = \frac{d\phi_i}{dt} = \frac{\partial H}{\partial I_i} \tag{2.15}$$

Once the initial condition $\{I_i(0), \phi_i(0)\}$ is given, the subsequent solution $\{I_i(t), \phi_i(t)\}$ is determined by integrating eqns. (2.14,2.15). $\{I_i(t), \phi_i(t)\}$ is known as a *phase space trajectory* or trajectory. When the Hamiltonian H is independent of time, a trajectory cannot intersect with itself in phase space, although it could retrace the same closed orbit over and over.

An important property of Hamiltonian systems is that the equations of motion remain formally invariant. After a transformation between two sets of canonical coordinates (called a *canonical transformation*), e.g. $(I_i, \phi_i) \rightarrow (J_i, \Phi_i)$ we have:

$$\dot{J}_i = -\frac{\partial H}{\partial \Phi_i} \tag{2.16}$$

$$\dot{\Phi}_i = \frac{\partial H}{\partial J_i} \tag{2.17}$$

2.2.3 Constants of Motion

In a time-independent Hamiltonian, the energy is conserved, i.e. is a *constant of motion*. Additional constants of motion may be present due to the polyad numbers. In the Fermi resonance system, the polyad number $\hat{P} = 2\hat{n}_1 + \hat{n}_2$ corresponds to a constant of motion through eqn. (2.12):

$$I = 2I_1 + I_2 = P + \frac{3}{2} \tag{2.18}$$

Like the quantum commutator in eqn. (2.10), the Poisson bracket between I and H also vanishes

$$\{I, H\} = \sum_i \left(\frac{\partial I}{\partial \phi_i} \frac{\partial H}{\partial I_i} - \frac{\partial I}{\partial I_i} \frac{\partial H}{\partial \phi_i} \right) = 0 \tag{2.19}$$

The angle θ conjugate to I must satisfy

$$\dot{I} = -\frac{\partial H}{\partial \theta} = 0 \tag{2.20}$$

and does not appear explicitly in the Hamiltonian. Such a variable is known as a *cyclic variable* [31]. This property naturally leads to a canonical transformation

$$(I_1, \phi_1, I_2, \phi_2) \rightarrow (I, \theta, I_z, \Psi)$$

with

$$I = \frac{2I_1 + I_2}{2} \qquad \theta = \phi_1 + 2\phi_2 \tag{2.21}$$

$$I_z = \frac{2I_1 - I_2}{2} \qquad \Psi = \phi_1 - 2\phi_2 \tag{2.22}$$

In the new coordinates, the classical Hamiltonian in eqn. (2.13) is expressed as

$$\begin{aligned} H_F =& \omega_1(I + I_z) + \omega_2(I - I_z) + x_{11}(I + I_z)^2 + x_{12}(I^2 - I_z^2) + x_{22}(I - I_z)^2 \\ &+ 2V_F\sqrt{(I + I_z)^2(I - I_z)}\cos\Psi \end{aligned} \tag{2.23}$$

I can be regarded as an external parameter as it does not change with time. θ is absent from the Hamiltonian, and has limited physical significance. The non-trivial part of the dynamics is captured in a 2-dimensional phase space (I_z, Ψ), which is called a *reduced phase space*. In general, with $(N - M)$ constants of motion in an N DOF Hamiltonian, the phase space can be *reduced* from $2N$ to $2M$ dimensions by a similar transformation. The details of such transformations are discussed in Appendix A.

When there are as many constants of motion as the DOF, a system is called *integrable*. In an integrable system, it is possible to express the Hamiltonian in terms of N constants of motion and cyclic variables. Then the trajectories can be solved analytically without recourse to numerical integration. A Hamiltonian with 1 DOF is always integrable when the energy is conserved.

2.2.4 Invariant Phase Space Structures

An *invariant phase space structure* is defined as any lower-dimensional subset of the phase space that is mapped onto itself by the equations of motion. These structures are "landmarks" that delineate regions in phase space with dif-

ferent dynamics. The qualitative description of all these regions can be called the *phase space portrait* [13].

Critical Points The simplest invariant phase space structure is a *critical point* [35]. These are defined as points where the equations of motion (2.14, 2.15) vanish[2]:

$$\frac{\partial H}{\partial \phi_i} = \frac{\partial H}{\partial I_i} = 0 \tag{2.24}$$

The critical points are the simplest invariant structure not only because they have the lowest dimensionality (zero), but also because they can be systematically determined as roots of simultaneous equations.

The *stability* of a critical point intuitively refers to the system's behavior when a trajectory deviates slightly from the point. A stable critical point can be compared to a potential minimum and an unstable one to a maximum. In the illustration of Fig. 2.3 (a), trajectories near a stable critical point are confined to the neighborhood, oscillating with small amplitude. Fig. 2.3 (b) shows that an unstable critical point behaves locally like a saddle point, with nearby trajectories deviating *exponentially* rapidly. Mathematically, the stability of a critical point (or other invariant structures) can be characterized in several ways to suit different purposes. The most important ones are Lyapunov, linear and spectral stabilities. Lyapunov stability implies linear stability, which in turn implies spectral stability

[2]The term "critical points" may also refer to where the gradient of a given function vanishes [36], and the function may not be related to any dynamical property. However, in Hamiltonian systems this definition coincides with the one in the text, because Hamilton's equations of motion coincide with the gradient of H with regard to the canonical coordinates.

[37]. The *linear stability* of a critical point has been widely used because it is easy to compute. Its exact derivation will be discusses in § 3.3.1.

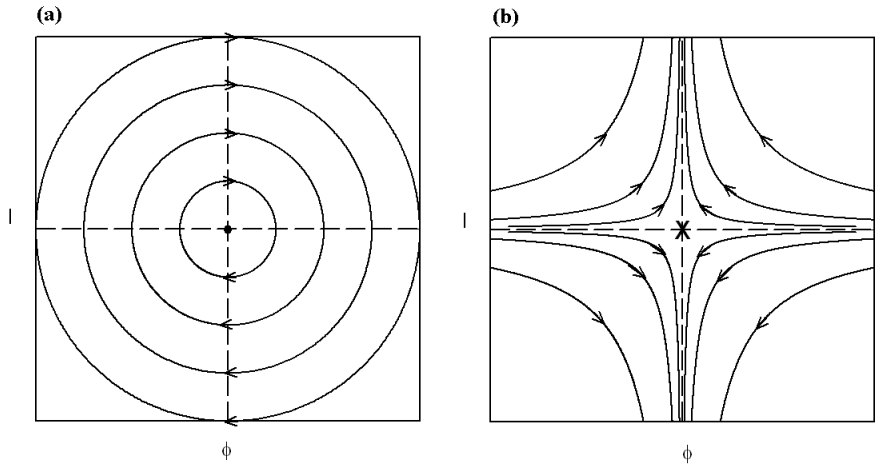

FIGURE 2.3 Trajectories near linearly stable and unstable critical points in a 1 DOF systems. Panel (a): near a linearly stable critical point. (b) near a linearly unstable critical point.

Periodic Orbits A closed *periodic orbit* (PO) is a trajectory that retraces itself with a finite period T:

$$\{I_i(nT), \phi_i(nT)\} = \{I_i(0), \phi_i(0)\} \quad \text{with n=1,2,3, } \ldots \tag{2.25}$$

A PO is a 1-dimensional invariant phase space structure. Unlike critical points, the only way to locate the POs in a general system is through an iterative numerical search [38].

Invariant Tori Another example of invariant phase space structure is the *invariant tori*. In an N DOF integrable system, if I_i are chosen as the N constants of motion,

then their conjugate angles θ_i evolve at constant frequencies $\dot{\theta}_i = \frac{\partial H}{\partial I_i}$ for any trajectory. These trajectories form a set of nesting N-dimensional tori, filling the (I_i, θ_i) phase space.

An $N = 2$ example is illustrated in Fig. 2.4. If $\dot{\theta}_1 : \dot{\theta}_2$ happens to be a rational number (also known as *commensurable*), the surface of the torus is covered by a family of PO [3]. Otherwise, any one trajectory will gradually fill the entire toroidal surface, instead of closing on itself within a finite time. This type of trajectory is called *quasiperiodic*.

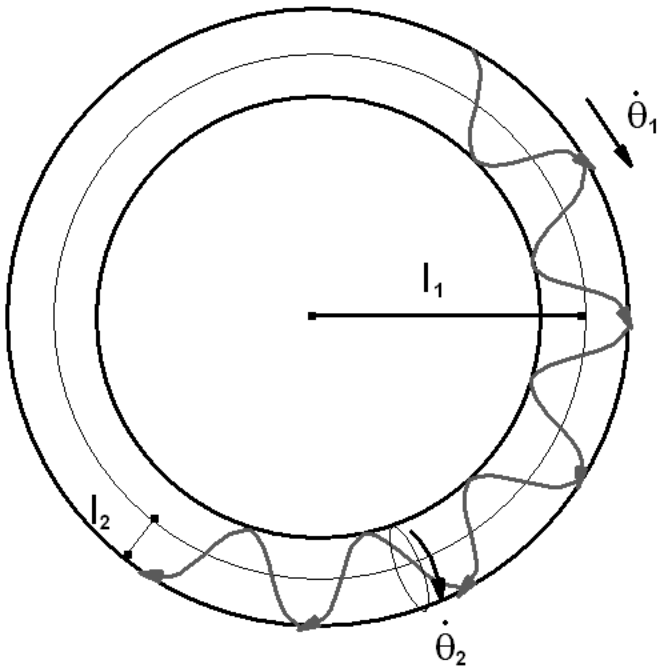

FIGURE 2.4 Trajectory on an invariant 2-torus.

[3]See the 3D model on the accompanying CD-ROM.

When small non-integrable perturbations are added to an integrable Hamiltonian, some invariant tori are destroyed and the rest remain in a deformed state . This is the result of the Kolmogorov-Arnold-Moser theorem [31]. Invariant tori in a non-integrable system generally indicate regions where the *local* dynamics closely resembles that in an integrable system.

In higher dimensions, there are also the *normal hyperbolic invariant manifolds* [39], which act as impenetrable barriers in the phase space. The constant energy shell is always an invariant structure in isolated systems.

2.2.5 Bifurcations

A bifurcation generally may refer to any qualitative change in the phase space portrait, as some external control parameter is being varied [13]. In practice, the "qualitative change" is labeled by the change in the number and/or stability of some well-defined objects, especially the invariant phase space structures. The "external control parameter" may refer to either a variable physical quantity (such as the energy), or coefficients in the Hamiltonian.

Fig. 2.5 depicts the so-called pitchfork bifurcation of critical points in a 1 DOF system. As the potential $V(x)$ in the Hamiltonian is continuously deformed, suddenly the single well (stable critical point) lifts to a barrier (unstable critical point), and two additional wells are born. The whole phase space portrait changes accordingly, adding two additional zones that correspond to confinement in the new local minima.

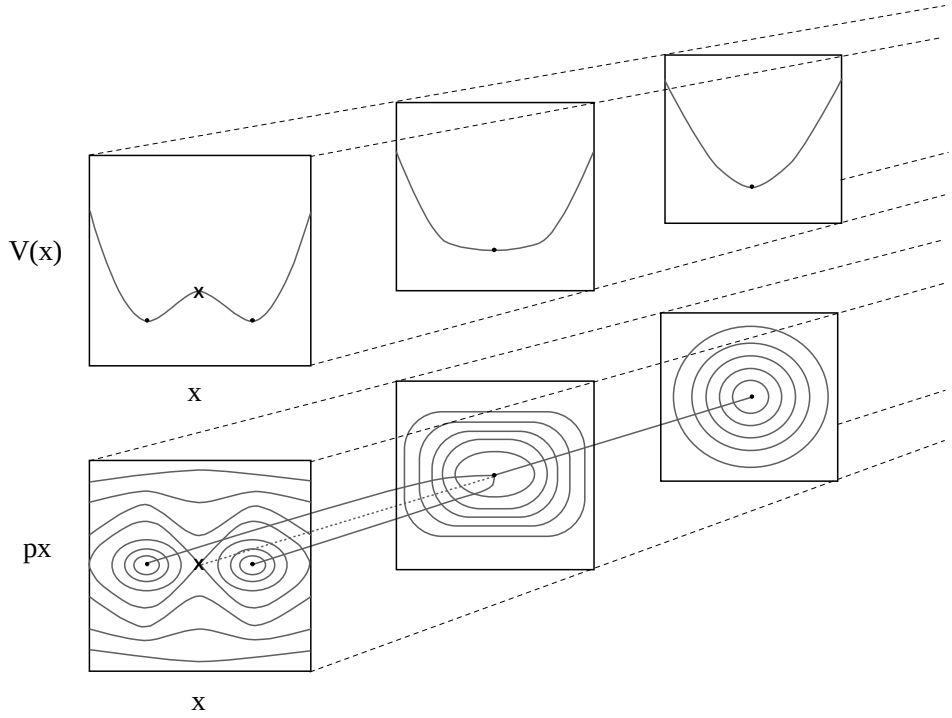

FIGURE 2.5 Pitchfork-type bifurcation in 1 DOF system and the associated phase space change. The back, middle and the front panels are before, at and after the bifurcation point.

The same principle holds throughout this thesis: *Qualitative changes in the classical phase space are tracked by solving for the bifurcations of critical points*. The parameters in the effective Hamiltonian are regarded as given, and the polyad number(s) varied as the control parameter.

2.2.6 Poincaré Surface of Section

In a 2 DOF system, the phase space is 4-dimensional and cannot be directly visualized as in the 1 DOF case. However, since the energy is conserved, the

phase space may be visualized by taking a series of 2-dimensional iso-energy slices. This technique is called *Poincaré Surface of Section* (SOS) [31].

The typical construction of a SOS in the phase space proceeds as follows. Let the 2 DOF canonical variables be of action-angle type I_1, ϕ_1, I_2, ϕ_2. First, an energy of interest is determined [4]. Then an ensemble of trajectories with this energy is integrated. Their intersections with a 2-dimensional dividing surface in the phase space (e.g. defined by $\phi_2 = 0$) are recorded by two other independent phase space variables (e.g. I_1, ϕ_1), as illustrated in Fig. 2.6. Due to time-reversal symmetry, only crossings in one direction, e.g. $d\phi_2/dt > 0$ are recorded.

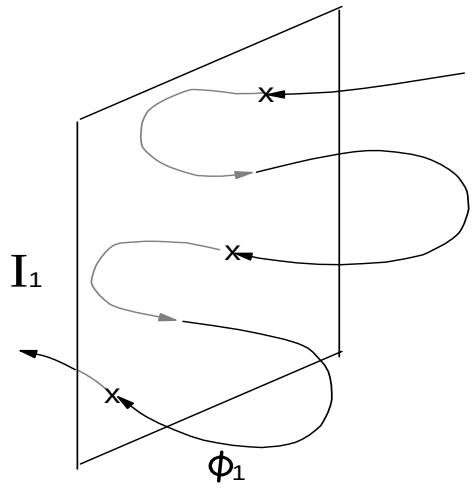

FIGURE 2.6 Construction of Poincaré Surface of Section.

[4]It can also be some other constant of motion that is held fixed instead of energy– see the footnote in § 3.1.2 later.

At a given energy, the classical dynamics is reflected in patterns of the corresponding SOS. Displayed in Fig. 2.7 are 4 SOS for the Henon-Heiles system [40], which is composed of two coupled 1-dimensional oscillators. There are two distinct types of trajectories in panel (a). For each of the red, black, blue and green trajectories, the crossings remain on two closed curves. Each pair of curves (e.g. the red ones on the p_y axis) can be thought of as the result of slicing the 2-dimensional invariant torus across the radius. This kind of phase space regions is called *regular*. The magenta trajectory, on the other hand, randomly fills an area complementary to the regular regions. Such a phase space region is called *chaotic*.

Panels (b)-(d) of Fig. 2.7 are taken for the same Hamiltonian with increasing energy. At the lowest energy (panel b), most of the SOS is regular. In panel (c) the portion of chaotic region increases. At the highest energy (d), most of the SOS is filled with trajectories that explore all the phase space volume allowed by the conservation of energy (the teardrop-shaped outline). This regular-to-chaotic trend is typical for dynamical systems that are nonintegrable. In this thesis, we focus on systems with mixed dynamics as in panel (c); with an important question being how to distinguish the regular regions from a sea of chaos.

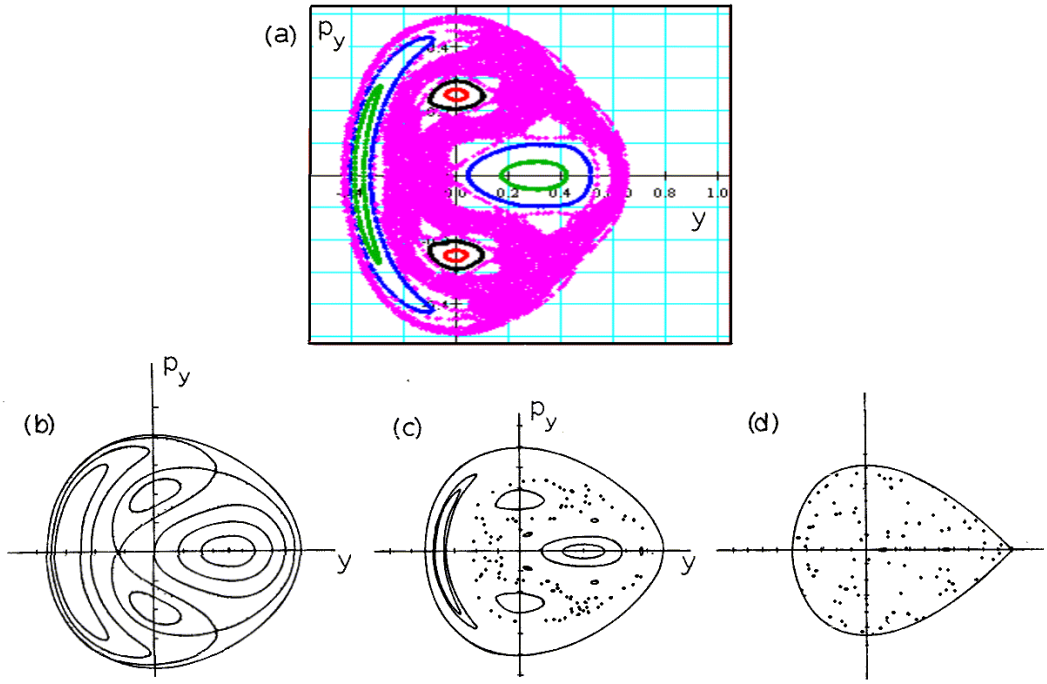

FIGURE 2.7 Regular, mixed and chaotic dynamics from an SOS of the Henon-Heiles Hamiltonian. Panel (a) (created by the online program at [41]) displays the contribution from 5 individual trajectories coded by color. Panels (b)-(d), adapted from [31], are taken with increasing energy, where the classical motion changes from regular to mixed to chaotic.

2.3 Quantum-Classical Correspondence

According to the well-known Bohr correspondence principle, when Planck's constant $\hbar \to 0$ or when the quantum number approaches infinity, the behavior of a quantum system converges to that of the corresponding classical system. A more recent theorem by Helton and Tabor concludes that in the limit $\hbar \to 0$, quantum eigenstates must localize into phase space regions supporting an "invariant measure", i.e. regions with invariant phase space structures [42].

The correspondence between classical invariant phase space structure and

quantum wavefunction has been observed at finite $\hbar$ in the phenomenon called *localization* [43]. Generally, a regular region of classical phase space corresponds to eigenfunctions with nodal structure aligned along the invariant phase space structures. In Fig. 2.8, for example, the nodal backbones of wavefunctions closely follow the periodic orbits labeled $[r]$, $[B]$, and $[SN]$. Wavefunction 4 corresponds to a combination of modes $[r]$ and $[B]$, and the nodes form a deformed rectangular grid along these two directions.

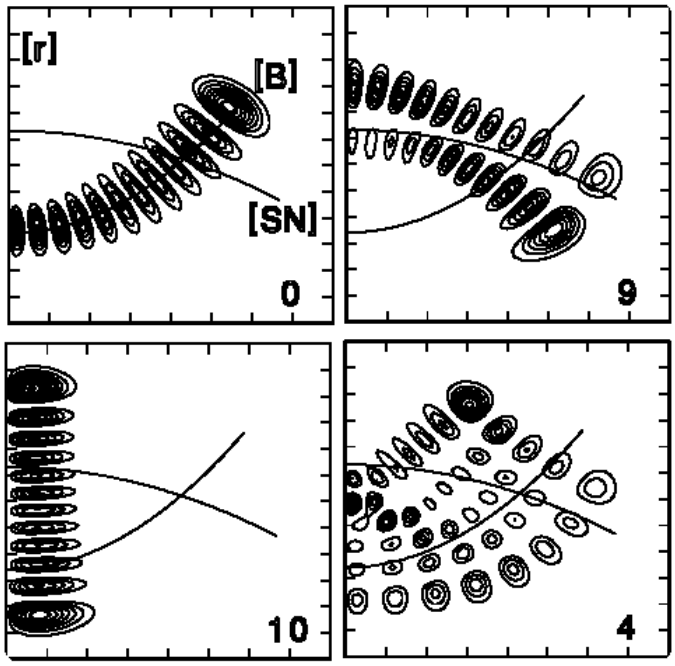

FIGURE 2.8 Localization of semiclassical wavefunctions in the HCP Hamiltonian, adapted from [19]. The lines labeled $[B]$, $[SN]$ and $[r]$ (which coincides with the left edge of the panel) are periodic orbits, which form the backbones of the wavefunctions. The axes are harmonic normal mode coordinates.

Most eigenfunctions in a classically chaotic system have randomly distributed nodes [44]. However, invariant phase space structures such as PO have been observed to have important influence even when the dynamics is dominated by chaos [45]. In the classical vibrational Hamiltonians, the presence of these phase space structures is indicative of the underlying patterns of vibration.

Such observations have led to renewed interest in using classical mechanics to understand excited molecular vibrations [46]. The goal is not only finding appropriate phase space structure to explain dynamics in an *a posteriori* manner, but also actively predicting the dynamics from analytic detection of classical phase space structures.

CHAPTER III

METHODOLOGY

In this chapter, we first review two existing methods of analyzing systems with one polyad number via classical critical points (§ 3.1, 3.2). Then in § 3.3 we address additional questions in order to formulate a generalized method of the critical points analysis. The analysis covers cases with arbitrary DOF and multiple polyad numbers. The method establishes that near a stable critical point in the reduced phase space, the classical trajectories are quasiperiodic. These critical points indicate the existence of regular quantum vibration modes.

3.1 Critical Points Analysis of Single $m : n$ Resonance

This systematic method was developed by Kellman *et al.* for analyzing an effective Hamiltonian with two modes coupled by a single resonance. A brief overview is given below on aspects that will be used in Chapter 4. For a more detailed description, the reader is referred to [17,47].

3.1.1 The $m : n$ Resonance Hamiltonian

In many triatomic molecules, the coupling between two vibrational modes 1 and 2 (which are not necessarily normal modes) can be approximated by an m :

n type resonance. Both m and n are positive integers. A third mode is relatively isolated, and is treated as a *spectator*. The effective two-mode Hamiltonian has the following form:

$$\hat{H}_{mn} = \hat{H}_0(n_1, n_2) + V_{mn}[(\hat{a}_1^\dagger)^m(\hat{a}_2)^n + (\hat{a}_2^\dagger)^n(\hat{a}_1)^m] \tag{3.1}$$

$\hat{H}_0$ is a Dunham expansion with the same form as in eqn. (2.2). The other term corresponds to a matrix element between ZOS $|n_1, n_2\rangle$ and $|n_1 + m, n_2 - n\rangle$. It removes m quanta from n_1 and adds n quanta to n_2, or vice versa. This coupling destroys both n_1, n_2 as exact quantum numbers, but preserves one polyad number

$$P_{mn} = \frac{n_1}{m} + \frac{n_2}{n} \tag{3.2}$$

Using Heisenberg's Correspondence Principle in eqn. (2.11), a classical Hamiltonian in action-angle variables (I_1, ϕ_1, I_2, ϕ_2) is obtained from eqn. (3.1). Then the following canonical transformation is carried out. Let σ be the largest common factor between m and n:

$$I = \frac{\sigma}{2}\left(\frac{I_1}{m} + \frac{I_2}{n}\right) \qquad \theta = \frac{m\phi_1 + n\phi_2}{\sigma} \tag{3.3}$$

$$I_z = \frac{\sigma}{2}\left(\frac{I_1}{m} - \frac{I_2}{n}\right) \qquad \Psi = \frac{m\phi_1 - n\phi_2}{\sigma} \tag{3.4}$$

I is the constant of motion differing from P_{mn} by a constant, while θ is its conjugate cyclic angle. The Hamiltonian becomes

$$H_{mn} = H_0(I, I_z) + 2V_{mn}(I + I_z)^{\frac{m}{2}}(I - I_z)^{\frac{n}{2}}\cos[\sigma\Psi] \tag{3.5}$$

In Chapter 2, eqn. (2.13) is one example with $m : n = 1 : 2$.

The 2 DOF Hamiltonian of (3.5) is integrable, since both the energy (H_{mn}) and I are constants of motion. The classical phase space can be formally reduced to 1 DOF with the equations of motion:

$$\dot{I}_z = -\frac{\partial H}{\partial \Psi}, \quad \dot{\Psi} = \frac{\partial H}{\partial I_z} \tag{3.6}$$

θ does not appear explicitly in the Hamiltonian, and I can be treated as a parameter. The reduced phase space is spanned by (I_z, Ψ).

3.1.2 The Polyad Phase Sphere and Critical Points

The reduced phase space in eqn. (3.5) has the same topology as the surface of a 2-dimensional sphere [6]. The sphere is called the *Polyad Phase Sphere* (PPS) [1]. On the PPS, the angle $\arccos[I_z/I]$ is the longitude while Ψ is its latitude, as shown in Fig. 3.1. According to their definitions in eqns. (3.4), I_z is a measure of the extent of mixing between the zero-order oscillators 1 and 2, and Ψ represents their relative phase angle. The north pole ($I_2 = 0$) is the mode 1 overtone, while the south pole ($I_1 = 0$) is the mode 2 overtone. At these two points, Ψ becomes unphysical, since the phase angle of an oscillator is ill defined when the amplitude is zero.

---

[1] Alternatively, (I_z, Ψ) could be regarded as a special SOS in the full phase space (I, θ, I_z, Ψ). Instead of energy, here I is held constant. The dividing surface is defined by a constant θ.

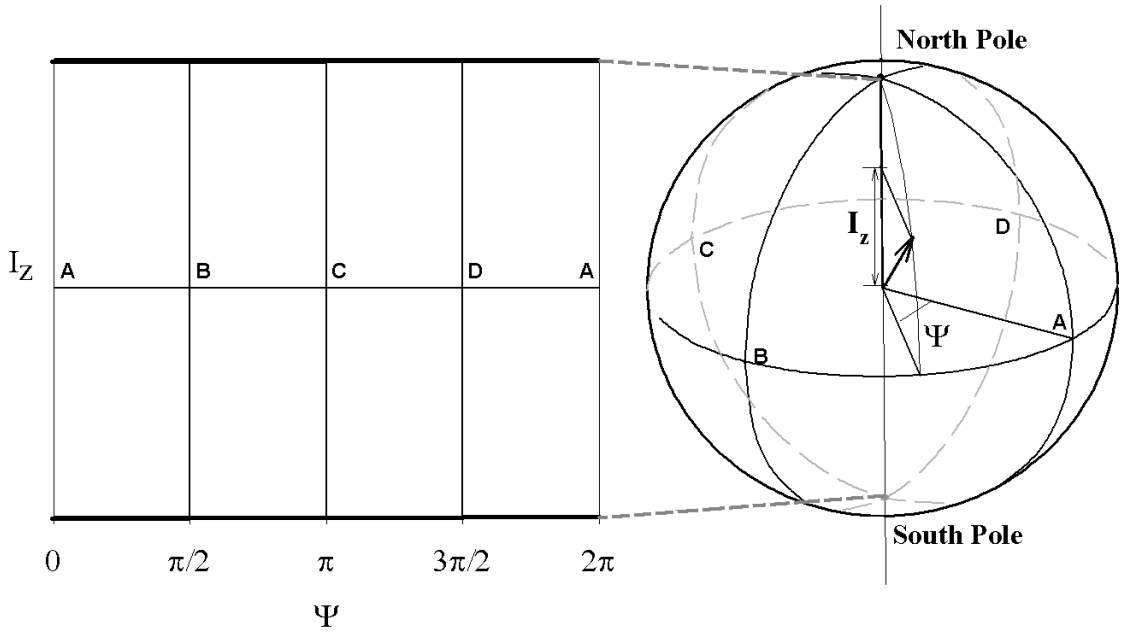

FIGURE 3.1 Coordinates on the polyad phase sphere (PPS). The rectangular plane in (a) is a Mecartor projection of the spherical surface in (b). Identical points are labeled by A-D in both panels to aid visualization.

In an integrable Hamiltonian, each quantum eigenstate of $\hat{H}_{mn}$ is associated with an invariant torus in (I, θ, I_z, Ψ) via the *Einstein-Brillion-Keller* (EBK) quantization procedure [48]. Each of these tori appears on the PPS as a closed semiclassical trajectory. In practice, this trajectory can be well approximated (within 1 cm $^{-1}$) by solving for points on the PPS that have the same energy as that of the quantum state [19].

All the semiclassical trajectories are organized by the critical points on the PPS. These points define where the flow of (I_z, Ψ) vanishes, i.e.

$$\dot{I}_z = -\frac{\partial H}{\partial \Psi} = 0 \qquad\qquad \dot{\Psi} = \frac{\partial H}{\partial I_z} = 0 \tag{3.7}$$

In the zero-order case ($V_{mn} = 0$), all trajectories are parallel to the equator on the PPS because H_{mn} has no dependence on Ψ. The only critical points are the north and south poles. This corresponds to the trivial case where the eigenstates are assigned with the zero-order quantum numbers n_1 and n_2. When the resonance is turned on, new critical points may emerge and the old ones may change their stabilities. This is called a bifurcation. The semiclassical trajectories, as well as the quantum states they represent, are organized around the critical points. A bifurcation therefore signals the birth, death and/or transformation of the vibrational modes in the system.

Fig. 3.2 shows a sample PPS for the HCP molecule ($m : n = 1 : 2$). Here modes 1 and 2 refer to the normal C-P stretch and normal H-C-P bend, respectively. In this particular polyad $P = n_1 + n_2/2 = 11$ there are 12 eigenstates, and their trajectories (labeled 0-11) are evenly spread over the surface of the PPS. The most prominent structure here is a separatrix (dashed line) with the unstable critical point $\overline{[SN]}$ ("**X**"). The separatrix is so-named because it separates the phase space into three regions: (1) levels 0-7 surrounding the stable critical point $[B]$; (2) levels 9,11 surrounding the stable critical point $[SN]$; and (3) levels 8,10 surrounding the stable critical point $[r]$ (normal mode 1). Each level can be assigned two quantum numbers: one is the polyad number P, the other is determined by the critical point its trajectory surrounds. Since the surface of the PPS is divided, the assignment is not uniform for all 11 states.

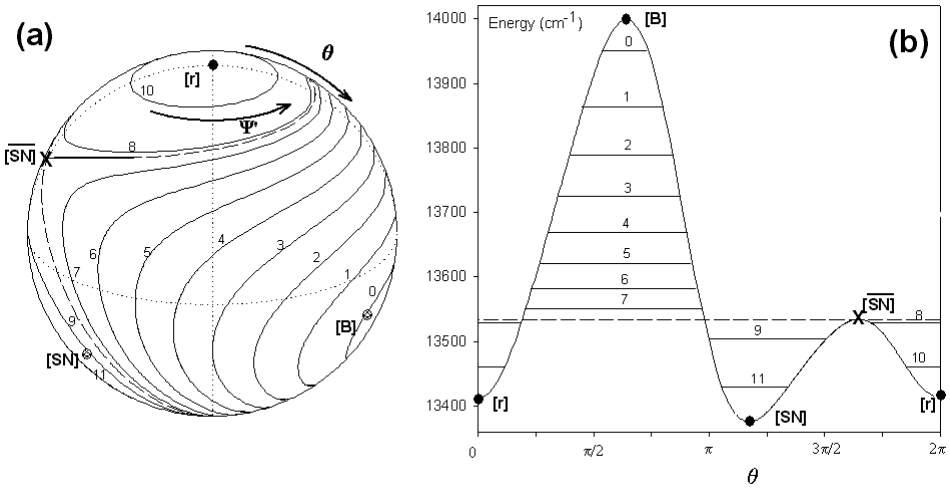

FIGURE 3.2 PPS and semiclassical trajectories adapted from [19]. (a) a view of the PPS. The points on the PPS labeled $[r]$, $[B]$ and $[SN]$ are stable critical points, while $\overline{[SN]}$ is an unstable critical point. The dashed line is the separatrix. Panel (b) presents a cut along the great circle defined by $\Psi = 0, \pi$, where $\theta \in [0, 2\pi]$ is a parameter around this great circle. Panel (b) also shows the relative energy of all 12 levels.

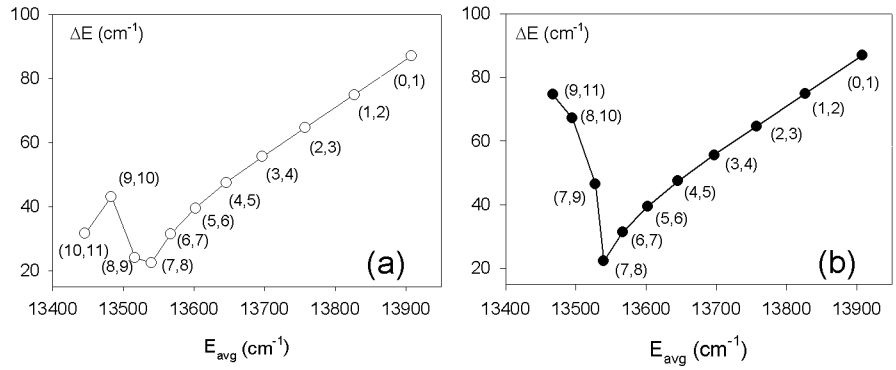

FIGURE 3.3 Gap in the spectral patterns induced by a classical separatrix for the PPS in Fig. 3.2.

In the full 4-dimensional phase space, although I, I_z and Ψ are fixed at the critical points, the cyclic angle θ is not. Instead, it precesses between 0 and 2π at a constant frequency. Hence, each critical point in the $m:n$ resonance Hamiltonian corresponds to a periodic orbit.

3.1.3 Spectral Patterns

The location of trajectories on the PPS reflects patterns in the quantum spectra. First, the ratio between n_1 and n_2 for each state corresponds to the time-averaged I_z of its trajectory. In the example of Fig. 3.2, levels 9,11 with $I_1 << I_2$ have a strong bending character, which are identified in experimental spectra by their large rotational constant B [49].

Second, a separatrix on the PPS acts like a barrier in phase space. Classically, the frequency traversing the top of a barrier is expected to drop to zero. The quantum equivalence of this frequency is the energy difference ΔE between adjacent levels. Therefore, the energy gap pattern is expected to exhibit a dip when a separatrix is crossed [50].

When the separatrix is in contact with more than 2 regions on the PPS (Fig. 3.2), the gaps should be taken only between eigenstates within the same region on the PPS. Otherwise, if the states are sorted by energy alone, levels 9, 11 are intermingled with 8,10. As shown in Fig. 3.3, this choice creates a zigzag

pattern in the energy gap of panel (a). The dip pattern is recovered when the energy differences is taken within the same zone(s) in panel (b). This resorting procedure was first discussed by Svitak *et al.* in [50].

3.1.4 Catastrophe Map

If the effective Hamiltonian only includes up to quadratic terms and V_{mn} is a constant, all possible PPS structures for a given type of $m : n$ resonance can be further summarized by just two independent parameters. The PPS up to a scaling factor can be reconstructed from these parameters. With the help of catastrophe theory in mathematics [14], this 2-parameter space (called *catastrophe map*) is divided into zones for any $m : n$ system [47], and within each zone the PPS have the same *qualitative* structure. As an example, Fig. 3.4 displays the catastrophe map as well as representative PPS for $m : n = 1 : 1$. In zone **I**, (cases 1, 5, 7, 8 and 9) the spheres share an undivided structure, while in zone **II** (cases 3, 4 and 6) the spheres are each divided by a separatrix. In going from spheres 1-2-3-4, the qualitative change happens at sphere 2 where its representative point crosses from **I** (normal mode dynamics) to **II** (local mode dynamics). 3D models of these spheres are also included on the accompanying CD-ROM.

The catastrophe map, however, is not suitable for extension to include high-order terms. In § 5.2 of [52], the inclusion of a single cubic term in H_0 adds

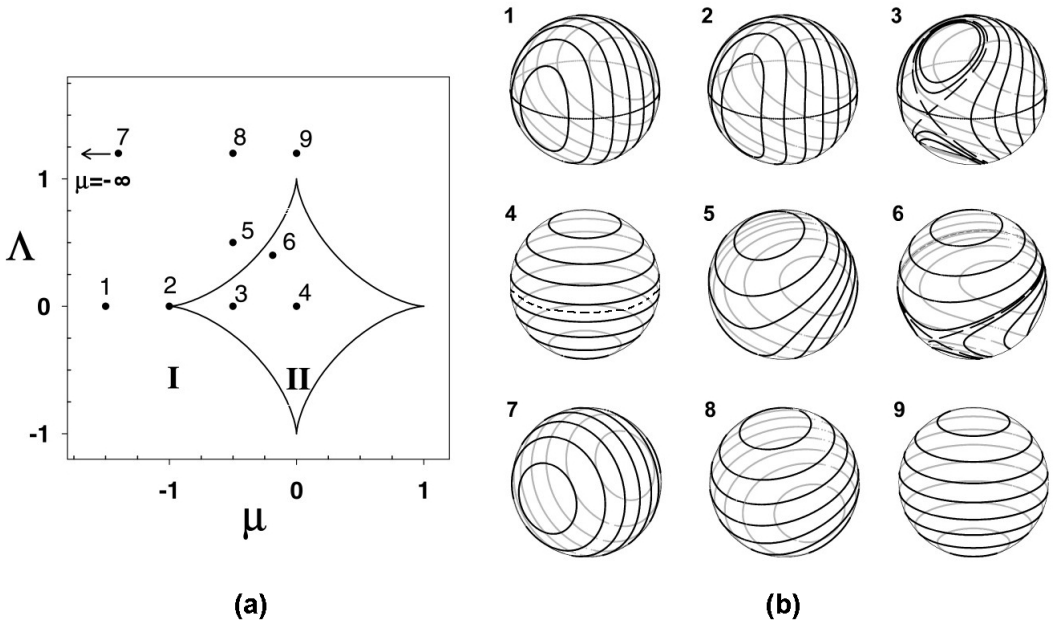

FIGURE 3.4 Catastrophe map of $1:1$ resonance system and associated PPS, adapted from [51]. Panel (a) is the catastrophe map with two independent parameters being μ and Λ. Panel (b) displays the PPS corresponding to each of the representative points on panel (a).

substantial complexity to the catastrophe map. When these high-order terms are indeed not ignorable, the more convenient alternative is analyzing the dynamics using the PPS and spectral patterns alone.

3.1.5 Summary

The above steps of the single resonance analysis are summarized in Fig. 3.5. The 2-dimensional reduced phase space is directly visualized with the PPS. Each quantum state corresponds to a semiclassical trajectory on the PPS. The trajectory can be assigned quantum numbers by the stable critical point it surrounds. The unstable critical points are associated with separatrices, which cause "dips" in the neighboring energy gap pattern among trajectories traversing them. All possible

divisions on the PPS with the same $m : n$ resonance can be further classified on the catastrophe map by two parameters.

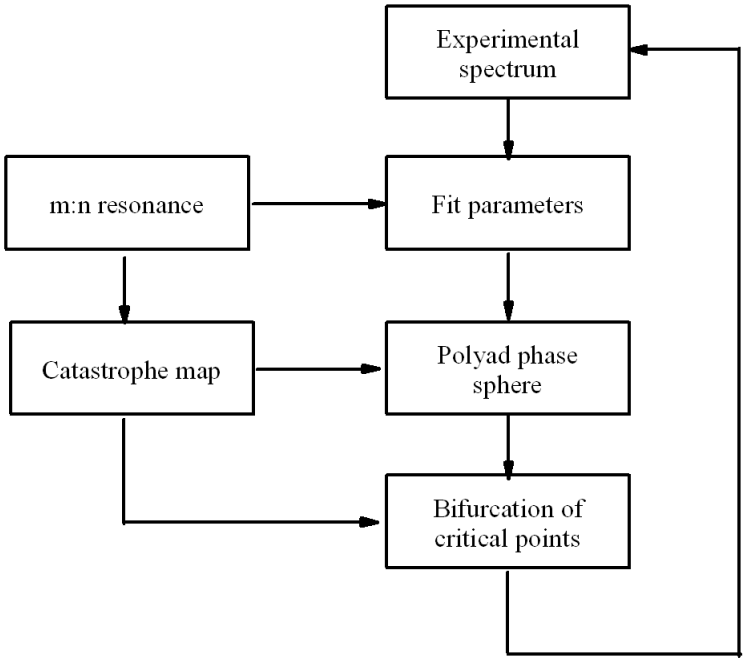

FIGURE 3.5 Bifurcation analysis of the single resonance Hamiltonian, adapted from Fig. 2 of [53] with modifications.

3.2 Large-Scale Bifurcation Analysis

In a non-integrable Hamiltonian, the main distinction in the classical phase space structure is between the regular and the chaotic regions. Even today, it remains a poorly understood field. The most challenging problems have multiple resonances acting simultaneously, preventing reduction of the dynamics to

less than 3 effective DOF and thus preventing direct visualization. For effective Hamiltonians with one polyad number (and arbitrary DOF), Lu and Kellman proposed the *large-scale bifurcation* analysis [16,54] as an extension of the above $m:n$ resonance analysis of integrable systems.

The main assumption of large-scale bifurcation analysis is that *"The large-scale bifurcation structure is defined by the lowest-order periodic orbits and their bifurcations."* [16]. In a 2 DOF Hamiltonian, phase space regions with different types of dynamics can be visually recognized on a SOS. Each regular region surrounds a "periodic orbit" on the SOS. Here the word "periodic" should not be confused with the continuous T in eqn. (2.25) for a PO. It refers to the trajectory that appears on the SOS at a few discrete points (as opposed to filling a continuous curve/area). The period is the integer number of steps between the returns. Those with period 1 are also known as *fixed points* on the SOS [2].

Consider a 3 DOF system with one polyad number (such as the Baggott H_2O Hamiltonian [55]). The polyad number enables one to rewrite the Hamiltonian in a 4-dimensional reduced phase space (I_1, ψ_1, I_2, ψ_2), plus a conserved action I_3 and a cyclic angle ψ_3. Dynamics in the reduced phase space can be visualized using a series of SOS. Without loss of generality, let the energy and

[2]In the existing literature, "fixed points" and critical points are often used interchangeably. In this thesis, to avoid confusion, "fixed point" is used in the context of a discrete mapping (such as an SOS) where the trajectory it represents is not stationery in the phase space. In contrast, critical points refer to stationery points in a continuous dynamical system.

coordinate ψ_2 be held constant in the construction of this SOS, and the crossings of trajectories be recorded in (I_1, ψ_1) space. A fixed point on the resulting SOS has all four action-angle variables (I_1, ψ_1, I_2, ψ_2) constant – therefore it must be a critical point of the reduced phase space:

$$\dot{I}_1 = \dot{\psi}_1 = \dot{I}_2 = \dot{\psi}_2 = 0 \tag{3.8}$$

Unless the cyclic angle ψ_3 has zero frequency, these critical points are closed POs in the full phase space.

Therefore, the large-scale phase space structure (i.e. fixed points on the SOS) can be found as critical points in the reduced phase space. This is done by solving the simultaneous analytic equations (3.8). It avoids numerical integration of many individual trajectories, as well as the subsequent problem of classifying their behavior into types of dynamics.

Ref. [16] solved the bifurcation structure of critical points for several similar systems. Fig. 3.6 is reproduced from [16] showing the bifurcation structure of H_2O. This structure is verified by two subsequent studies using methods that are more detailed [39,56]. In the limit of $P \to 0$, there are 3 branches of critical points corresponding to the 3 normal modes. In the lower right corner of Fig. 3.6, the normal bend family is aligned along the vertical line, while the two normal O-H stretches are on top of each other, along the short diagonal segment between the origin and point A. Then as P is increased, resonances cause the normal modes to bifurcate (at points A, B, B', etc.) into new families of critical points. These

critical points were then used to successfully assign all states in polyad $P = 8$ to quantum numbers consistent with the vibrational dynamics [54].

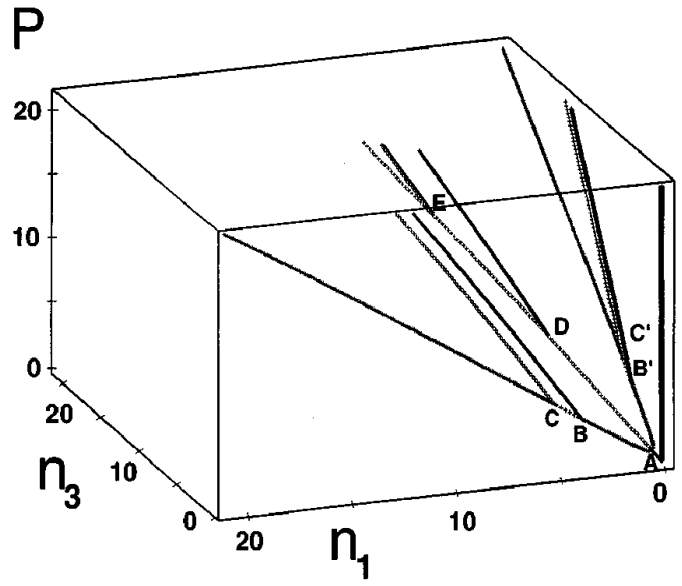

FIGURE 3.6 Large-scale bifurcation structure in H_2O, reproduced from Fig. 3 in [16].

3.3 Generalized Critical Points Analysis

In the previous subsections, the importance of critical points is illustrated for both integrable and nonintegrable Hamiltonians. In using the critical points to characterize modes of vibration in nonlinear systems, two aspects should be emphasized.

(1) The existence of polyad numbers is crucial for this analysis. Specifically, the polyad numbers make it possible to reduce the DOF of the classical Hamiltonian.

The cyclic angle(s) not explicit in the reduced phase space provide time evolution for the critical points in the full phase space. In comparison, a critical point defined in the *full* phase space usually conveys little information about the dynamics. For example, although two coupled anharmonic oscillators may exhibit a rich range of dynamical behavior, this is not apparent from examination of the equilibrium point (where there is no motion in either oscillator). With a *single* polyad number, critical points in the reduced phase space are POs in the full phase space, which form the "skeletons" of phase space [39]. In the presence of *multiple* polyad numbers, the critical points are expected to have the same importance, although they now correspond to invariant tori in the full phase space.

(2) The critical points are found by solving analytically defined equations. Because the method does not rely on numerical integration of Hamilton's equations, it circumvents the problem induced by unstable/chaotic trajectories. In addition, unlike most existing nonlinear methods, the equations can (at least theoretically) be extended to arbitrary DOF in a straightforward manner.

In § 3.1 - 3.2 we only considered systems with 1 polyad number and up to 3 DOF. The following 3 points need to be addressed in order to extend the critical points analysis to multiple polyad numbers and arbitrarily large number of DOF.

1. In a 2 DOF system, the consistency between critical points and large-scale phase space structure may be verified by direct inspection such as through SOS. These visual aids become increasingly impractical in higher dimensions. Although it was suggested that the large-scale bifurcation analysis

could be extended to > 3 DOF systems with one polyad number [17], it remains unclear how the "periodic orbits" defined on a SOS (see § 3.2) can be extended to arbitrary DOF. A dimensionality-independent description of the dynamics surrounding a critical point is strongly preferred.

2. With multiple polyad numbers, the critical points generally have multiple non-commensurable frequencies associated with the cyclic angles. Motion at these critical points is quasiperiodic in the full phases space, instead of being closed POs. To what extent would this difference affect the predictions of classical and quantum dynamics of the molecule?

3. In references [39,54], the eigenstate assignment was performed via the localization of the Husimi distribution function of the states, which is performed by visual inspection. As both the computation of these semiclassical wavefunctions and the visual assignment become increasingly difficult in higher dimensions, a more general consideration of how to assign wavefunction localization becomes necessary.

The next three subsections discuss these questions in their order. The result is a more generalized framework of critical points analysis, which will be used in Chapter 4 to analyze the C_2H_2 bending system.

3.3.1 Reduced Phase Space Trajectory Near A Critical Point

First, we consider an effective Hamiltonian of the most general form. Let the Hamiltonian have a total of N modes, M linearly independent resonance vectors, and $(N - M)$ polyad numbers. The classical Hamiltonian after a suitable canonical transformation has $(N - M)$ constants of motion, their conjugate cyclic angles $\{P_{M+1}, \cdots, P_N, \theta_{M+1}, \cdots, \theta_N\}$, and $2M$ action-angle variables J_i, Ψ_i spanning the reduced phase space

$$\vec{X} = \{x_i\} = \{\Psi_1, \cdots, \Psi_M, J_1, \cdots, J_M\}$$

Hamilton's equations of motion in the reduced phase space can be written in the following matrix form

$$\frac{d}{dt}\vec{X} = \begin{pmatrix} -\frac{\partial H}{\partial x_{M+1}} \\ \cdots \\ -\frac{\partial H}{\partial x_{2M}} \\ \\ \frac{\partial H}{\partial x_1} \\ \cdots \\ \frac{\partial H}{\partial x_M} \end{pmatrix} = \begin{pmatrix} 0 & -E_M \\ E_M & 0 \end{pmatrix} \begin{pmatrix} \frac{\partial H}{\partial x_1} \\ \cdots \\ \frac{\partial H}{\partial x_M} \\ \\ \frac{\partial H}{\partial x_{M+1}} \\ \cdots \\ \frac{\partial H}{\partial x_{2M}} \end{pmatrix} \tag{3.9}$$

with E_M being the $M \times M$ unit matrix. A critical point $\vec{X}_0$ in the reduced phase space is defined by the $2M$ simultaneous equations:

$$\left(\frac{\partial H}{\partial x_i}\right)_{X_0} = 0 \tag{3.10}$$

Linear stability is defined by the behavior of the *linearized* equations of motion at nearby points. Let the point be

$$\vec{X} = X_0 + \{dx_1, \cdots, dx_i, \cdots, dx_{2M}\} = \vec{X}_0 + d\vec{X} \tag{3.11}$$

The linearized equations of motion are obtained by expanding $\partial H/\partial x_i$ on the right hand of eqn. (3.9) into a Taylor series, and keeping only terms linear to the displacement

$$\left(\frac{\partial H}{\partial x_i}\right)_X = \left(\frac{\partial H}{\partial x_i}\right)_{X_0} + \sum_j \left(\frac{\partial^2 H}{\partial x_i \partial x_j}\right)_{X_0} dx_j = \sum_j \left(\frac{\partial^2 H}{\partial x_i \partial x_j}\right)_{X_0} dx_j \tag{3.12}$$

Then eqn. (3.9) is reduced to the linearized form:

$$\frac{d}{dt}\vec{X} = \begin{pmatrix} 0 & -E_M \\ E_M & 0 \end{pmatrix} \left(\frac{\partial^2 H}{\partial x_i \partial x_j}\right)_{X_0} d\vec{X} = A \cdot d\vec{X} \tag{3.13}$$

which is a set of homogeneous ordinary differential equations. The standard procedure of solving them requires first finding the $2M$ eigenvalues λ_i and eigenvectors $\vec{V}_i$ of matrix A [57]. The λ_i and corresponding $\vec{V}_i$ satisfy

$$A \cdot \vec{V}_i = \lambda_i \ \vec{V}_i \tag{3.14}$$

If none of the λ_i is equal to zero, the solutions have the following form:

$$\vec{X}(t) = \vec{X}_0 + \sum_{i=1}^{2M} a_i \ e^{\lambda_i t} \ \vec{V}_i \tag{3.15}$$

With a_i being arbitrary complex coefficients. The time evolution of $\vec{X}(t)$ therefore is separable into $2M$ directions, each indicated by the vector $\vec{V}_i$.

The linear stability of $\vec{X}_0$ is defined in terms of eqn. (3.13), through the eigenvalues λ_i. In a Hamiltonian system, the conservation of phase space volume (Liouville's theorem) leads to the result that the λ_i always appear in conjugate quadruplets ($\pm a \pm bi$), for which there are four cases described below.

A) When a pair of λ_i is purely imaginary ($a = 0$), all solutions in eqn. (3.15) would oscillate in the subspace spanned by $\vec{V}_i$ with a characteristic frequency determined by $|\lambda_i|$. The linear stability in this direction is known as *stable*, *elliptic* or (E).

B) When a pair of λ_i is real ($b = 0$), all solutions in eqn. (3.15) would be attracted to or repelled from $\vec{X}_0$ exponentially with time in the $\vec{V}_i$ subspace. This direction is known as linearly *unstable*, *hyperbolic* or (H). The names elliptic and hyperbolic originated from the shape of these linearized trajectories (Fig. 2.3).

C) When a quadruplet of $\lambda_i = \pm a \pm bi$ has $a, b \neq 0$, the solution contains *both* oscillating and exponential attraction/repulsion components in the subspace spanned by the four $\vec{V}_i$ corresponding to the quadruple λ_i. In two of the four directions the nearby trajectory "spirals" towards the critical point, while in the other two directions it "spirals" away from the critical point. This stability type is called *mixed* or (M) [16].

D) When a pair of $\lambda_i = 0$, the stability type is degenerate (D). In this case, the linearized equations eqn. (3.13) become insufficient, and higher-order terms in the Taylor expansion are needed to evaluate the stability near a critical point.

If all the eigenvalues fall into category (A), then the linearized trajectories defined by eqn. (3.15) oscillate with M distinctive frequencies. *Hence, near an all-stable critical point, the linearized equations of motion are quasiperiodic.* They are expected to resemble the trajectories of the true Hamiltonian for at least a finite time.

3.3.2 The Presence of Multiple Cyclic Angles

At a critical point, all the canonical variables are fixed except the $(N - M)$ cyclic angles θ_i. Unless any of their frequencies becomes zero or commensurable with another, the full phase space trajectory is quasiperiodic and restricted to an $(N - M)$ dimensional invariant torus. When there is more than one polyad number, the trajectory does not close onto itself within a finite time.

Intuitively, the role these critical points play in the phase space should not change whether there are one or more cyclic angles. As an example, consider the case of HCP where only 2 of the 3 normal modes are coupled by a Fermi resonance [19]. Excitation in the spectator mode 3 (C-H stretching) can be treated as a parameter in the effective Hamiltonian. Strictly speaking there are *two* polyad numbers and cyclic angles:

$$P_1 = n_1 + \frac{n_2}{2} \qquad \theta_1 = 2\phi_1 + \phi_2 \tag{3.16}$$

$$P_2 = n_3 \qquad \theta_2 = \phi_3 \tag{3.17}$$

Yet, in assigning e.g. the $n_3 = 1$ states, one could simply use the critical points found in this manifold, in spite of the fact that the frequency of θ_2 is *not* zero here.

We argue that in general the cyclic angles θ_i represent a trivial aspect of the dynamics, at least as far as quantum spectra are concerned. This is evident if one considers the semiclassical quantization. There they appear as a pre-factor with the form ($\Pi e^{iP_i\theta_i}$) in the resulting wavefunctions [7]. The θ_i angles do not have physical meaning on their own, since the polyad number P are not uniquely defined.

Critical points in a reduced phase space, especially those with non-zero frequencies in the cyclic coordinate, are known as *relative equilibria* in the mathematics community [58,59]. Near a relative equilibrium, classical dynamics in the full phase space can be rigorously separated into two parts: the *group orbit*,

which is motion along the cyclic angles; and motion in the reduced phase space [60]. The latter is a multidimensional "slice" transverse to the group orbit [61]. The slice contains all the "essential dynamics" (page 304 of [58]), in the sense that the full dynamics can be reconstructed from a point on the slice and appropriate initial conditions. This provides a further argument against making a distinction between systems with one and multiple polyad numbers.

In the field of physical chemistry, relative equilibria theory has been used to classify rotationally excited molecular spectra [62,63]. Total angular momentum J plays the same role as the polyad numbers in this thesis. At a relative equilibrium, the molecule rotates with a constant shape. Vibrational modes are defined by the normal form of the Hamiltonian near the *stable* relative equilibria. As J is increased, the bifurcations of relative equilibria correspond to predictions of the as yet unobserved rovibrational spectral patterns.

3.3.3 Semiclassical Localization Near A Critical Point

An eigenstate may be assigned meaningful quantum numbers based on the critical point, if its representation in the same (Ψ_i, J_i) space is localized near the critical point with a well-ordered nodal pattern. The semiclassical wavefunctions can be obtained through either (1) full phase space representations (e.g. the Wigner or Husimi function [64]) or (2) the angle-space *semiclassical quantization* proposed by Voth and Marcus in [65]. Examples of both methods are illustrated in Fig. 3.7. In panels (a) and (b), the localization is along the normal mode critical

points with ($n_1 = n_2 = 3.5, \psi_1 = \frac{\pi}{2}$ and $\frac{3\pi}{2}$). In panels (c) and (d), the localization is around the critical points at ($\psi_a = \pm\pi, \psi_b = \pm\pi$).

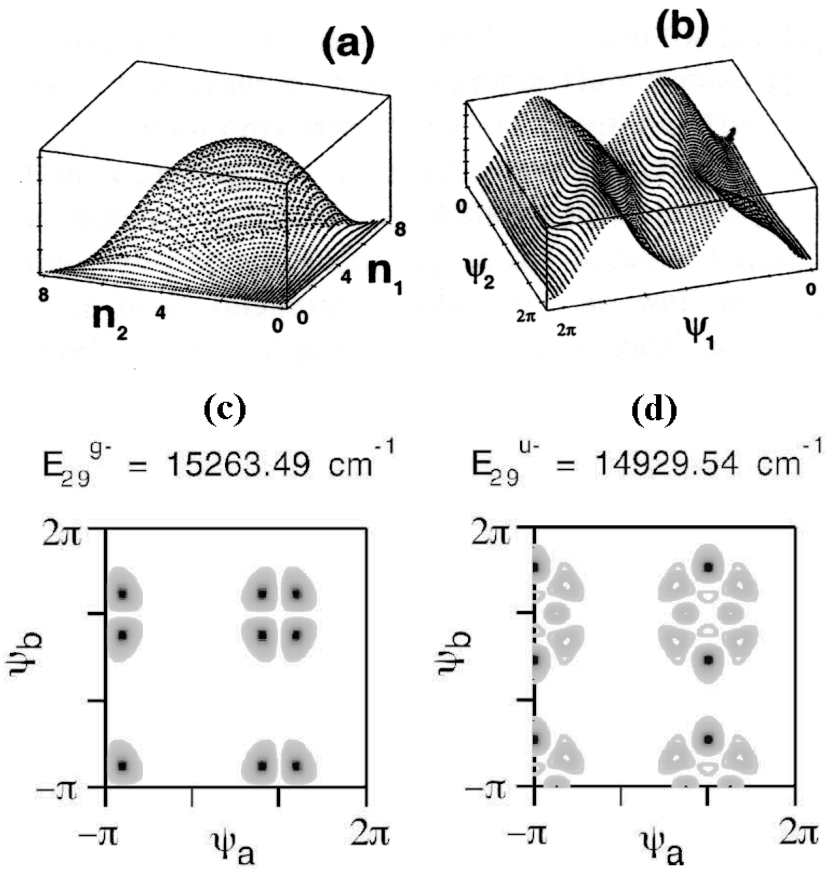

FIGURE 3.7 Semiclassical localization in action-angle phase space. Panels (a), (b) are reproduced from Fig. 3 of [54], displaying the two projections of the Husimi function of the same eigenstate in action (n_1, n_2) and angle (ψ_1, ψ_2) space, respectively. Panels (c) and (d) are reproduced from Fig. 5 of [66], which display the angle-space representation of two different wavefunctions both localized around ($\psi_a = \pm\pi, \psi_b = \pm\pi$).

Consider a local minimum or maximum (together referred to as *extremum*) in the reduced phase space (Ψ_i, J_i). This extremum point is necessarily a critical

point. Then if there is a quantum eigenstate whose energy is nearby, intuitively one expects the semiclassical representation of the eigenstate in (Ψ_i, J_i) or (Ψ_i) space to localize near the critical point, simply because of the limited volume of accessible phase space into which it can expand. This is illustrated schematically in Fig. 3.8.

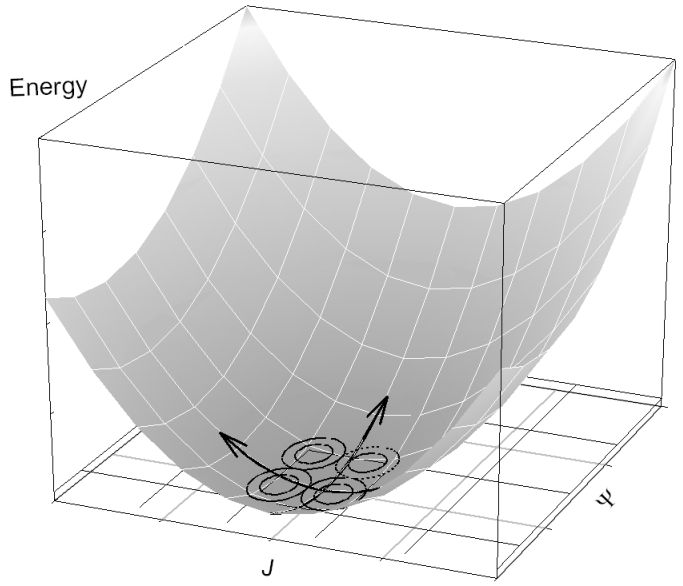

FIGURE 3.8 Localization near a minimum of the Hamiltonian, which is also an elliptic critical point. An eigenstate with energy nearby must be localized in nearby phase space.

There is no apparent reason why the same argument should not be valid for all choices of semiclassical representation, as well as for arbitrary dimensionality of the system, except for the following two scenarios. The localization may be

disrupted by tunneling when the local extremum is not prominent enough, or there are other local extrema nearby with similar energy.

In § 3.3.2 it was shown that the linearized motion near an all-stable critical point is quasiperiodic. If (1) it is a good approximation for the real classical trajectories in this region and (2) the region is large enough to support one quantizing invariant torus, then the semiclassical wavefunctions may be localized around the torus, with M quantum numbers assigned by EBK quantization. Therefore, one could expect the all-stable critical points to correspond to quantum modes around which semiclassical wavefunctions localize.

3.3.4 Summary

From § 3.3.1 - 3.3.3, we can draw the following conclusions about critical points in the reduced phase space:

1. Linearized classical trajectories near these points are quasiperiodic.
2. The existence of additional cyclic angles are not expected to affect the essential part of the classical dynamics or semiclassical localization.
3. Semiclassical eigenfunctions are expected to localize near the critical points if the latter correspond to local extrema in the reduced phase space.

The critical points can be used to assign vibrational modes to the quantum spectra. The change in their number and/or stability should correspond to the change in birth, death and transformations of the vibrational modes.

CHAPTER IV

BIFURCATION ANALYSIS OF C_2H_2 BENDS

4.1 Introduction

Acetylene (C_2H_2) is among the most-studied polyatomic molecules in spectroscopy. Its normal mode constants on the ground electronic state (S_0) have been refined over a long period [67,68]. At increased energy, however, its vibrational dynamics is rather complex. Recently the highly excited spectra of acetylene became more accessible due to techniques such as Stimulated Emission Pumping and Dispersed Fluorescence (DF). The observations include additional spectral features under enhanced resolution [30], signatures of both regularity and chaos in level statistics [69], and the emergence of local modes in H-C-C bending [28,66,70–73] and C-H stretching [24,74]. The stretch-bend system has also been investigated in a few studies [75–81]. Theoretical analysis of these results, however, remains challenging. While the coupled vibrational DOF are too numerous for many analytical tools, they are not enough to warrant a statistical approach.

The dynamics of acetylene vibration has an important role in combustion processes. Its interconversion with vinylidene, a marginally stable isomer, directly influences the outcome of reaction rate modeling [82]. Fig. 4.1 illustrates the geometry and energy change during the isomerization process. The transition

state is planar and involves mostly one C-H bond in acetylene bending over. It is believed that the highest bending levels recorded by Field *et al.* are within 5,000 cm^{-1} of the reaction barrier [83]. Decoding the dynamics hidden in these spectra is expected to shed light on this isomerization process.

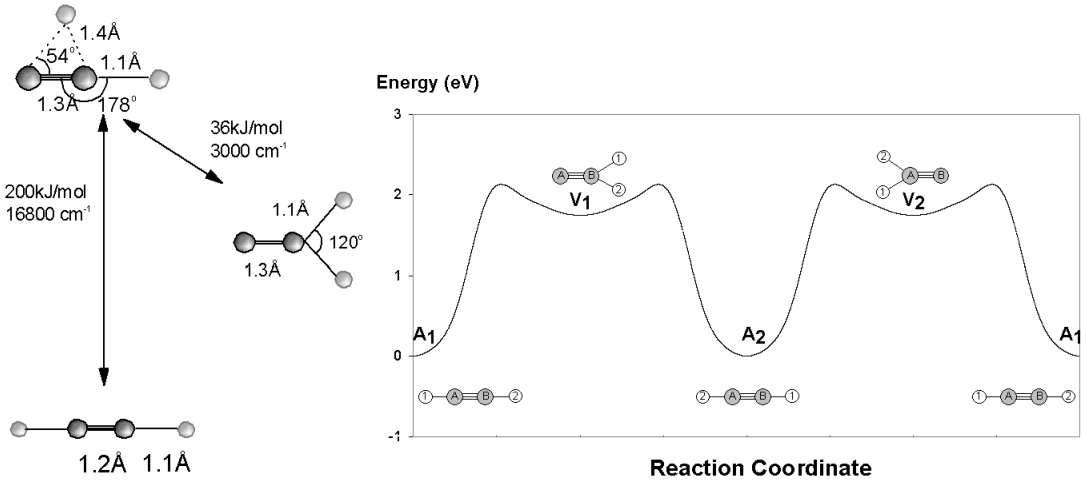

FIGURE 4.1 The acetylene-vinylidene isomerization on the S_0 electronic surface. The energy and configurations are averaged over compiled *ab initio* results in Table. 1 of [84]. Note that 1 eV = 8080 cm^{-1}.

For modeling highly excited states ($\approx$ 10,000 cm^{-1}), the effective Hamiltonians from fitting spectra are reliable than any existing *ab initio* PES. The best-known PES [85] barely reproduces the quantitative experimental results in this energy range [86]. A refined PES recently published by Bowman *et al.* is still not as accurate as a direct fit to the spectra [87,88].

Near its linear equilibrium configuration, acetylene has $3N - 5 = 7$ normal modes as shown in Fig. 4.2. Both ν_4, ν_5 bends are doubly degenerate. Two additional quantum numbers ℓ_4, ℓ_5 are used to label the respective *vibrational angular momenta*.

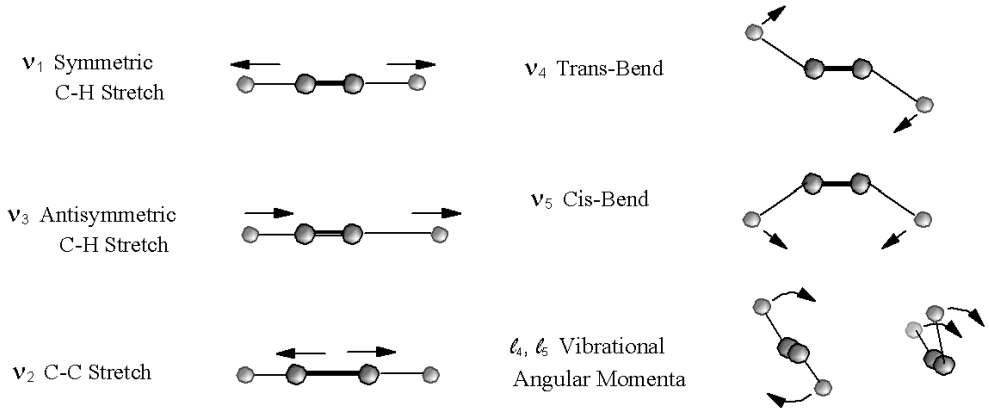

FIGURE 4.2 Normal vibrational modes of C_2H_2, with ν_4 and ν_5 being doubly degenerate. Also shown schematically are the two vibrational angular momenta.

The existing stretch-bend effective Hamiltonians all conserve three polyad numbers:

$$N_t = 5n_1 + 3n_2 + 5n_3 + n_4 + n_5 \tag{4.1a}$$

$$N_s = n_1 + n_2 + n_3 \tag{4.1b}$$

$$\ell = \ell_4 + \ell_5 \tag{4.1c}$$

N_t is the "total" quantum number, representing the approximate integer ratio among the normal mode frequencies. Using the frequencies of [89] in units of cm^{-1}, the ratio is

$$\omega_1 : \omega_2 : \omega_3 : \omega_4 : \omega_5 = 3371.66 : 1974.76 : 3288.75 : 608.50 : 729.18 \approx 5 : 3 : 5 : 1 : 1$$

N_s is the total number of stretching quanta. In the absence of rotational excitation ($J = 0$), ℓ denotes the total angular momentum of the molecule, which is always conserved [1]. The inversion symmetry (gerade/ungerade), parity (+/-) and total angular momentum J are also conserved [93]. Each polyad can therefore be labeled as $[N_t, N_s, \ell]^{g/u}$.

4.2 C_2H_2 Pure Bending System

4.2.1 Quantum Effective Hamiltonian

The pure bending states with ($N_s = 0$) form a separate subsystem among the $[N_t, N_s, \ell]^{g/u}$ polyads. In the remainder of Chapter 4, these polyads are labeled by $[N_b, \ell]^{g/u}$ with

$$N_b = N_t = n_4 + n_5 \tag{4.2}$$

Field *et al.* produced the latest pure bending effective Hamiltonian. The data used in their fit includes both energies and intensity information from FTIR and DF experiments [83]. The high-lying levels were obtained from DF spectra

[1]Incidentally, all three polyad numbers remain good for the isotopomer $^{13}C_2H_2$ [90]. The doubly deuterated C_2D_2 conserves N_s and ℓ [91]. Experimental spectra also suggest the existence of polyad structure in the monodeuterated C_2HD [92].

with a frequency resolution of 2 cm^{-1}, and unresolved $\ell = 0/2$ states. These levels are as much as 15,000 cm^{-1} above the ground vibrational state. The parameters in this Hamiltonian are listed in Table 4.1.

TABLE 4.1 Parameters in pure bending effective Hamiltonian, from [83]. The parameters are in units of cm^{-1}.

ω_4	608.657	y_{555}	0.00955
ω_5	729.137	g_{44}	0.677
x_{44}	3.483	g_{45}	6.670
x_{45}	-2.256	g_{55}	3.535
x_{55}	-2.389	S_{45}	-8.574
y_{444}	-0.03060	r^0_{45}	-6.193
y_{445}	0.0242	r_{445}	0.0304
y_{455}	0.0072	r_{545}	0.0110

Using the normal mode basis $|n_4^{\ell_4}, n_5^{\ell_5}\rangle$ ($(n_i \geq |\ell_i|)$) as the ZOS, the fitting Hamiltonian has a diagonal part H_0 and three resonance couplings.

$$\hat{H}_{bend} = \hat{H}_0 + \hat{V}_{DDI} + \hat{V}_\ell + \hat{V}_{DDII} \tag{4.3}$$

$$\hat{H}_0 = \omega_4 n_4 + \omega_5 n_5 + x_{44} n_4^2 + x_{45} n_4 n_5 + x_{55} n_5^2 + y_{444} n_4^3 + y_{445} n_4^2 n_5 + y_{455} n_4 n_5^2 + y_{555} n_5^3 + g_{44} \ell_4^2 + g_{45} \ell_4 \ell_5 + g_{55} \ell_5^2 \tag{4.4}$$

1. A Darling-Dennison [94] resonance (DD-I):

$$\langle n_4^{\ell_4}, n_5^{\ell_5} | \hat{V}_{DDI} | n_4 - 2^{\ell_4}, n_5 + 2^{\ell_5} \rangle = \frac{S_{45}}{4} \left[(n_4^2 - \ell_4^2)(n_5 + \ell_5 + 2)(n_5 - \ell_5 + 2) \right]^{1/2} \tag{4.5}$$

2. An ℓ-resonance:

$$\langle n_4^{\ell_4}, n_5^{\ell_5} | \hat{V}_\ell | n_4^{\ell_4 \mp 2}, n_5^{\ell_5 \pm 2} \rangle = \frac{R_{45}}{4} \left[(n_4 \mp \ell_4)(n_4 \pm \ell_4 + 2)(n_5 \pm \ell_5)(n_5 \mp \ell_5 + 2) \right]^{1/2} \tag{4.6}$$

with $R_{45} = r^0_{45} + r_{445}(n_4 - 1) + r_{545}(n_5 - 1)$.

3. Another Darling-Dennison resonance (DD-II), which is weaker than the other two:

$$\langle n_4^{\ell_4}, n_5^{\ell_5} | \hat{V}_{DDII} | n_4 - 2^{\ell_4 \mp 2}, n_5 + 2^{\ell_5 \pm 2} \rangle = \frac{R_{45} + 2g_{45}}{16} \times$$
$$[(n_4 \pm \ell_4)(n_4 \pm \ell_4 - 2)(n_5 \pm \ell_5 + 2)(n_5 \pm \ell_5 + 4)]^{1/2} \tag{4.7}$$

Fig. 4.3 illustrates the manner these resonances act within a polyad. The resonances are shown as lines connecting pairs of ZOS. $\hat{V}_{DDI}$ couples within each column (same ℓ_4, ℓ_5), while $\hat{V}_\ell$ couples within each row (same n_4, n_5). $\hat{V}_{DDII}$ in eqn. (4.7) contains couplings along the diagonal directions. With both $\hat{V}_{DDI}$ and $\hat{V}_\ell$, or $\hat{V}_{DDII}$ alone, all ZOS in a polyad $[N_b, \ell]^{g/u}$ are connected into an inseparable network.

Alternatively, $\hat{H}_{bend}$ can be written with raising/lowering operators, which act on the normal-mode trans- and cis- 2-dimensional oscillators. The symmetry-adapted operators $\hat{a}^\dagger_{4d}, \hat{a}^\dagger_{4g}, \hat{a}_{4d}, \hat{a}_{4g}$ and $\hat{a}^\dagger_{5d}, \hat{a}^\dagger_{5g}, \hat{a}_{5d}, \hat{a}_{5g}$ [2] are defined according to [95] as

$$\hat{a}^\dagger_{id} | n_i^{\ell_i} \rangle = \sqrt{\frac{n_i + \ell_i + 2}{2}} | n_i + 1^{\ell_i + 1} \rangle, \qquad \hat{a}^\dagger_{ig} | n_i^{\ell_i} \rangle = \sqrt{\frac{n_i - \ell_i + 2}{2}} | n_i + 1^{\ell_i - 1} \rangle \tag{4.8}$$

$$\hat{a}_{id} | n_i^{\ell_i} \rangle = \sqrt{\frac{n_i + \ell_i}{2}} | n_i - 1^{\ell_i - 1} \rangle, \qquad \hat{a}_{ig} | n_i^{\ell_i} \rangle = \sqrt{\frac{n_i - \ell_i}{2}} | n_i - 1^{\ell_i + 1} \rangle \tag{4.9}$$

[2] The g (gauche/left) and d (droit/right) subscripts are named according to the manner they affect the vibrational angular momentum.

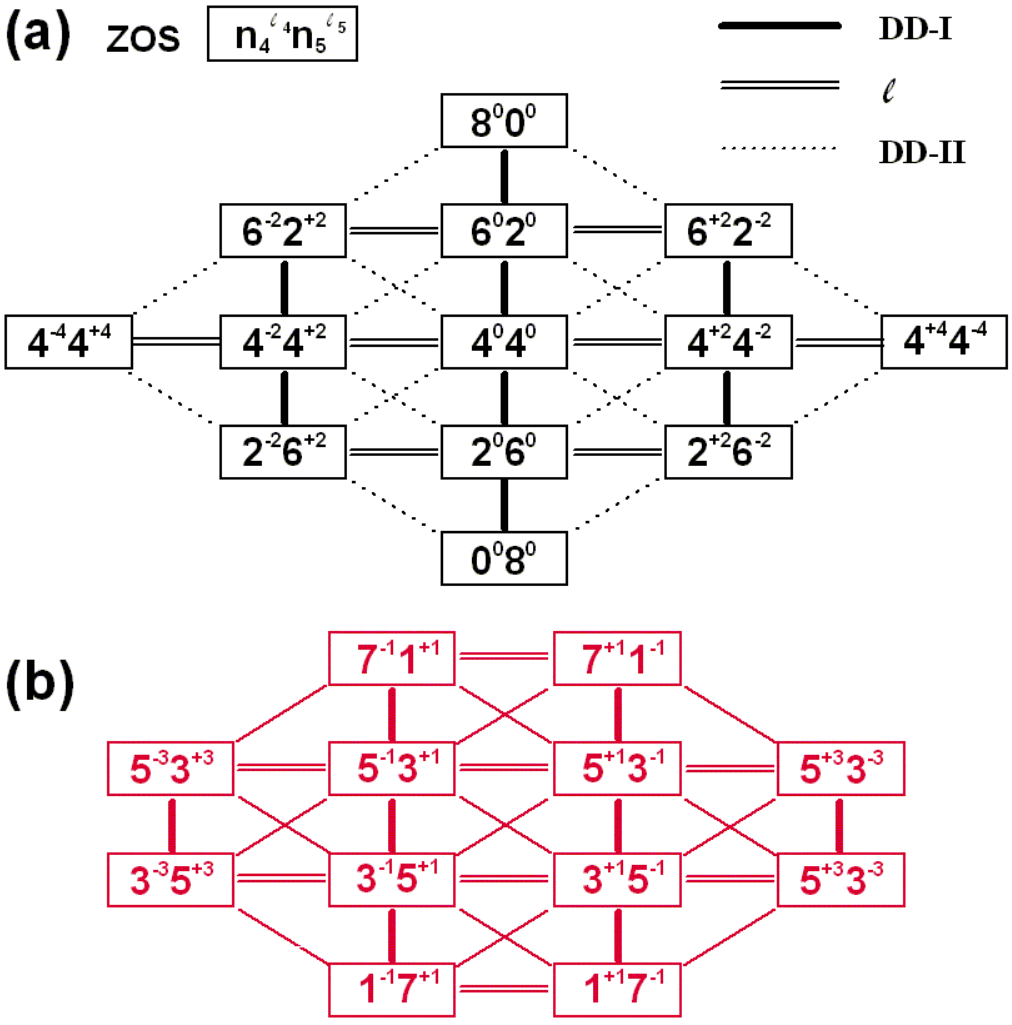

FIGURE 4.3 Resonance couplings within a pure bending polyad $[8, 0]$. Panel (a) displays the g states and panel (b) the u states.

The zero-order part of $\hat{H}_{bend}$ can be expressed with

$$n_i = \hat{a}^\dagger_{id}\hat{a_{id}} + \hat{a}^\dagger_{ig}\hat{a}_{ig}, \qquad \ell_i = \hat{a}^\dagger_{id}\hat{a}_{id} - \hat{a}^\dagger_{ig}\hat{a}_{ig} \tag{4.10}$$

and the resonance terms as

$$\hat{V}_{DDI} = S_{45}[\hat{a}^\dagger_{4d}\hat{a}^\dagger_{4g}\hat{a}_{5d}\hat{a}_{5g} + \hat{a}_{4d}\hat{a}_{4g}\hat{a}^\dagger_{5d}\hat{a}^\dagger_{5g}] \tag{4.11}$$

$$\hat{V}_{\ell} = R_{45}[\hat{a}_{4d}\hat{a}^\dagger_{4g}\hat{a}^\dagger_{5d}\hat{a}_{5g} + \hat{a}^\dagger_{4d}\hat{a}_{4g}\hat{a}^\dagger_{5d}\hat{a}_{5g}] \tag{4.12}$$

$$\begin{aligned}\hat{V}_{DDII} = \frac{R_{45}+2g_{45}}{4}[&\hat{a}^\dagger_{4d}\hat{a}^\dagger_{4d}\hat{a}_{5d}\hat{a}_{5d} + \hat{a}^\dagger_{4g}\hat{a}^\dagger_{4g}\hat{a}_{5g}\hat{a}_{5g} \\ &+ \hat{a}_{4d}\hat{a}_{4g}\hat{a}^\dagger_{5d}\hat{a}^\dagger_{5d} + \hat{a}_{4g}\hat{a}_{4g}\hat{a}^\dagger_{5g}\hat{a}^\dagger_{5g}]\end{aligned} \tag{4.13}$$

4.2.2 Classical Hamiltonian

Next, a classical Hamiltonian is obtained from $\hat{H}_{bend}$ using Heisenberg's Correspondence Principle of eqn. (2.11). The result is expressed in canonical action-angle type variables I_i, ϕ_i ($i = 4d, 4g, 5d, 5g$). The actions are related to the zero-order quantum numbers by

$$I_{4d} = (n_4 + 1 + \ell_4)/2, \qquad I_{4g} = (n_4 + 1 - \ell_4)/2 \tag{4.14}$$

$$I_{5d} = (n_5 + 1 + \ell_5)/2, \qquad I_{5g} = (n_5 + 1 - \ell_5)/2 \tag{4.15}$$

Corresponding to N_b and ℓ, there are two conserved classical actions:

$$I_{4d} + I_{4g} + I_{5d} + I_{5g} = n_4 + n_5 + 2 = N_b + 2 \tag{4.16}$$

$$I_{4d} - I_{4g} + I_{5d} - I_{5g} = \ell_4 + \ell_5 = \ell \tag{4.17}$$

In order to reduce the dimensionality of the phase space, the following canonical transformation is useful [3]

$$
\begin{aligned}
K_a &= \frac{I_{4d}+I_{4g}+I_{5d}+I_{5g}}{2} = \frac{N_b+2}{2} & \theta_a &= \frac{\phi_{4d}+\phi_{4g}+\phi_{5d}+\phi_{5g}}{2} \\
K_b &= \frac{I_{4d}-I_{4g}+I_{5d}-I_{5g}}{2} = \frac{\ell}{2} & \theta_b &= \frac{\phi_{4d}-\phi_{4g}+\phi_{5d}-\phi_{5g}}{2} \\
J_a &= \frac{I_{4d}+I_{4g}-I_{5d}-I_{5g}}{2} = \frac{n_4-n_5}{2} & \psi_a &= \frac{\phi_{4d}+\phi_{4g}-\phi_{5d}-\phi_{5g}}{2} \\
J_b &= \frac{I_{4d}-I_{4g}-I_{5d}+I_{5g}}{2} = \frac{\ell_4-\ell_5}{2} & \psi_b &= \frac{\phi_{4d}-\phi_{4g}-\phi_{5d}+\phi_{5g}}{2}
\end{aligned}
\tag{4.18}
$$

The resulting classical Hamiltonian is

$$
\begin{aligned}
H(K_a,K_b,J_a,J_b,\psi_a,\psi_b) &= \omega_4(K_a+J_a-1)+\omega_5(K_a-J_a-1) \\
&+ x_{44}(K_a+J_a-1)^2 + x_{45}(K_a+J_a-1)(K_a-J_a-1) + x_{55}(K_a-J_a-1)^2 \\
&+ y_{444}(K_a+J_a-1)^3 + y_{445}(K_a+J_a-1)^2(K_a-J_a-1) \\
&+ y_{455}(K_a+J_a-1)(K_a-J_a-1)^2 + y_{555}(K_a-J_a-1)^3 \\
&+ g_{44}(K_b+J_b)^2 + g_{45}({K_b}^2-{J_b}^2) + g_{55}(K_b-J_b)^2 \\
&+ \frac{S_{45}}{2}\Big[(K_a^2-K_b^2)^2+(J_a^2-J_b^2)^2-2(K_a^2+K_b^2)(J_a^2+J_b^2)-8K_aK_bJ_aJ_b\Big]^{\frac{1}{2}}\cos[2\psi_a] \\
&+ \frac{R^*_{45}}{2}\Big[(K_a^2-K_b^2)^2+(J_a^2-J_b^2)^2-2(K_a^2+K_b^2)(J_a^2+J_b^2)-8K_aK_bJ_aJ_b\Big]^{\frac{1}{2}}\cos[2\psi_b] \\
&+ \frac{1}{8}[R^*_{45}+2g_{45}]\{[(K_a+K_b)^2-(J_a-J_b)^2]\cos[2(\psi_a-\psi_b)]+ \\
&\quad [(K_a-K_b)^2-(J_a+J_b)^2]\cos[2(\psi_a+\psi_b)]\}
\end{aligned}
\tag{4.19}
$$

with

$$
R^*_{45} = r^0_{45} + r_{445}(K_a+J_a-2) + r_{545}(K_a-J_a-2) \tag{4.20}
$$

---

[3] These new coordinates are defined in the same way as Jacobson *et al.* in [66]. The only difference is that our actions are expanded by a factor of 2, while the angles are reduced by a factor of $1/2$. Such a difference is trivial, except ours are more compatible to the single-resonance analysis of § 4.4.1 .

Since K_a and K_b are constants of motion, their conjugate angles θ_a, θ_b are the cyclic variables and therefore absent from the Hamiltonian. However, they do evolve in time with

$$\dot{\theta_a} = \frac{\partial H}{\partial K_a} \tag{4.21}$$

$$\dot{\theta_b} = \frac{\partial H}{\partial K_b} \tag{4.22}$$

The reduced phase space $(J_a, \psi_a, J_b, \psi_b)$ is four-dimensional. The equations of motion in it are:

$$\dot{\psi_a} = \frac{\partial H}{\partial J_a}, \qquad \dot{J_a} = -\frac{\partial H}{\partial \psi_a} \tag{4.23}$$

$$\dot{\psi_b} = \frac{\partial H}{\partial J_b}, \qquad \dot{J_b} = -\frac{\partial H}{\partial \psi_b} \tag{4.24}$$

The parameters in Table 4.1 apply to $\ell = 0,\ 2$, which from eqns. (4.18) correspond to $K_b = 0,\ \frac{1}{2}$, respectively. This thesis will focus on these cases. For $\ell = 0$, $K_b = 0$ and thus eqn. (4.19) becomes

$$H_{bend}(K_a, J_a, J_b, \psi_a, \psi_b) = H_0 + V_{DDI} + V_\ell + V_{DDII} + V_{DDII}^{'} \tag{4.25}$$

with

$$\begin{aligned} H_0 = {} & \omega_4(K_a + J_a - 1) + \omega_5(K_a - J_a - 1) + x_{44}(K_a + J_a - 1)^2 \\ & + x_{45}(K_a + J_a - 1)(K_a - J_a - 1) + x_{55}(K_a - J_a - 1)^2 + y_{444}(K_a + J_a - 1)^3 \\ & + y_{445}(K_a + J_a - 1)^2(K_a - J_a - 1) + y_{455}(K_a + J_a - 1)(K_a - J_a - 1)^2 \\ & + y_{555}(K_a - J_a - 1)^3 + (g_{44} - g_{45} + g_{55})J_b^2 \end{aligned} \tag{4.26}$$

and

$$V_{DDI} = \frac{S_{45}}{2}\left[K_a^4 + (J_a^2 - J_b^2)^2 - 2K_a^2(J_a^2 + J_b^2)\right]^{1/2}\cos[2\psi_a] \tag{4.27}$$

$$V_{\ell} = \frac{R_{45}^*}{2}\left[K_a^4 + (J_a^2 - J_b^2)^2 - 2K_a^2(J_a^2 + J_b^2)\right]^{1/2}\cos[2\psi_b] \tag{4.28}$$

$$V_{DDII} = \frac{1}{8}(R_{45}^* + 2g_{45})[K_a^2 - (J_a - J_b)^2]\cos[2(\psi_a - \psi_b)] \tag{4.29}$$

$$V_{DDII}^{'} = \frac{1}{8}(R_{45}^* + 2g_{45})[K_a^2 - (J_a + J_b)^2]\cos[2(\psi_a + \psi_b)] \tag{4.30}$$

4.3 Critical Points Analysis

Following the method outlined in Chapter 3, the critical points in the reduced phase space are expected to indicate the changes in vibrational modes. In this section, we explicitly solve for the critical points for $\ell = 0$ in eqn. (4.25) and their bifurcations with variation of N_b. Four new families of critical points are found at increasing N_b when the initially stable normal modes become unstable in distinct bifurcations. Two of the new families, namely the Local and Counter Rotator critical points, are linearly bi-stable (EE). They correspond to new stable modes of bending vibration.

Readers not interested in details of the calculation may skip the next subsection and go directly to § 4.4.2 for the results.

4.3.1 Computational Details

The critical points of eqn. (4.25) are defined by four simultaneous equations:

$$\dot{J}_a = -\frac{\partial H}{\partial \psi_a} = 0 \tag{4.31}$$

$$\dot{J}_b = -\frac{\partial H}{\partial \psi_b} = 0 \tag{4.32}$$

$$\dot{\psi}_a = \frac{\partial H}{\partial J_a} = 0 \tag{4.33}$$

$$\dot{\psi}_b = \frac{\partial H}{\partial J_b} = 0 \tag{4.34}$$

To simplify the notation we let

$$\Lambda = [K_a^4 - 2K_a^2(J_a^2 + J_b^2) + (J_a^2 - J_b^2)^2]^{1/2} \tag{4.35}$$

The left sides of eqns. (4.31-4.34) become

$$\begin{aligned}
\frac{\partial H}{\partial \psi_a} =& -\Lambda S_{45}\sin[2\psi_a] - \frac{1}{4}(R^*_{45} + 2g_{45})\{[K_a^2 - (J_a - J_b)^2]\sin[2(\psi_a - \psi_b)] + \\
& [K_a^2 - (J_a + J_b)^2]\sin[2(\psi_a + \psi_b)]\}
\end{aligned} \tag{4.36}$$

$$\begin{aligned}
\frac{\partial H}{\partial \psi_b} =& -\Lambda R^*_{45}\sin[2\psi_b] + \frac{1}{4}(R^*_{45} + 2g_{45})\{[K_a^2 - (J_a - J_b)^2]\sin[2(\psi_a - \psi_b)] - \\
& [K_a^2 - (J_a + J_b)^2]\sin[2(\psi_a + \psi_b)]\}
\end{aligned} \tag{4.37}$$

$$\begin{aligned}
\frac{\partial H}{\partial J_a} =& \frac{\partial H_0}{\partial J_a} - \frac{J_a}{\Lambda}(K_a^2 - J_a^2 + J_b^2)(S_{45}\cos[2\psi_a] + R^*_{45}\cos[2\psi_b]) + \Lambda(r_{445} - r_{545})\cos[2\psi_b] \\
& - \frac{R^*_{45} + 2g_{45}}{4}\{(J_a - J_b)\cos[2(\psi_a - \psi_b)] + (J_a + J_b)\cos[2(\psi_a + \psi_b)]\} \\
& + \frac{r_{445} - r_{545}}{2}\{2J_aJ_b\sin[2\psi_a]\sin[2\psi_b] + (K_a^2 - J_a^2 - J_b^2)\cos[2\psi_a]\cos[2\psi_b]\}
\end{aligned} \tag{4.38}$$

$$\begin{aligned}
\frac{\partial H}{\partial J_b} =& 2(g_{44} - g_{45} + g_{55})J_b - \frac{J_b}{\Lambda}(K_a^2 + J_a^2 - J_b^2)(S_{45}\cos[2\psi_a] + R^*_{45}\cos[2\psi_b]) \\
& + \frac{R^*_{45} + 2g_{45}}{4}\{(J_a - J_b)\cos[2(\psi_a - \psi_b)] - (J_a + J_b)\cos[2(\psi_a + \psi_b)]\}
\end{aligned} \tag{4.39}$$

A visual inspection of the first two equations (4.36, 4.37) reveals a *sufficient condition* [4] for both of them to vanish:

$$\sin[2\psi_a] = \sin[2\psi_b] = 0 \tag{4.40}$$

or

$$(\psi_a, \psi_b) = (\frac{m\pi}{2}, \frac{n\pi}{2}) \qquad \text{with } m, n = 0, 1, 2, 3 \tag{4.41}$$

Eqn. (4.41) leads to the 16 combinations of (ψ_a, ψ_b) in Table 4.2. The remaining two equations (4.38, 4.39) are then solved for J_a and J_b, with (ψ_a, ψ_b) held at these discrete values. Eqns. (4.38, 4.39) are invariant with regard to the transformations

$$\psi_a \rightarrow \psi_a + \pi \tag{4.42}$$

$$\psi_b \rightarrow \psi_b + \pi \tag{4.43}$$

It is then sufficient to consider only one entry out of each row in Table 4.2. Here we use:

$$(\psi_a, \psi_b) = (0,0)\,, \left(0, \frac{\pi}{2}\right), \left(\frac{\pi}{2}, 0\right), \left(\frac{\pi}{2}, \frac{\pi}{2}\right) \tag{4.44}$$

Given the (ψ_a, ψ_b) values of Table 4.2, eqn. (4.39) is further simplified as:

$$\frac{\partial H}{\partial J_b} = J_b\{2(g_{44} - g_{45} + g_{55}) - \frac{K_a^2 + J_a^2 - J_b^2}{\Lambda}(S_{45}\cos[2\psi_a] + R_{45}^*\cos[2\psi_b]) - \frac{R_{45}^* + 2g_{45}}{2}\cos[2\psi_a]\cos[2\psi_b]\} = 0 \tag{4.45}$$

[4] An additional root search was carried out, and no extra critical points were found beyond the ones discussed here.

TABLE 4.2 (ψ_a, ψ_b) values of bending critical points.

(ψ_a, ψ_b)	(ψ_a, ψ_b)	(ψ_a, ψ_b)	(ψ_a, ψ_b)
(0, 0)	(0, π)	(π, 0)	(π, π)
(0, $\frac{\pi}{2}$)	(0, $\frac{3\pi}{2}$)	(π, $\frac{\pi}{2}$)	(π, $\frac{3\pi}{2}$)
($\frac{\pi}{2}$, 0)	($\frac{3\pi}{2}$, π)	($\frac{\pi}{2}$, 0)	($\frac{3\pi}{2}$, π)
($\frac{\pi}{2}$, $\frac{\pi}{2}$)	($\frac{\pi}{2}$, $\frac{3\pi}{2}$)	($\frac{3\pi}{2}$, $\frac{\pi}{2}$)	($\frac{3\pi}{2}$, $\frac{3\pi}{2}$)

All terms on the right-hand side are proportional to J_b. The other multiplier (the sum of terms between the curly brackets) can be numerically shown to be always positive. Hence eqn. (4.34) has the trivial solution:

$$J_b = 0 \tag{4.46}$$

The last equation (4.33) is then solved analytically on a personal computer using the software *Mathematica* [96].

At each critical point, the linear stability is determined by the eigenvalues of the stability matrix described in § 3.3.1. Here the matrix is 4×4 in size, and the possible stability types are bi-stable (EE), bi-unstable (HH), stable-unstable (EH), mixed (MM) and degenerate [16].

Special consideration of the critical points is required where $|J_a|+|J_b| = K_a$. At these points, the values of ψ_a and ψ_b are indeterminate as the denominator Λ in eqns. (4.38, 4.39) vanishes. The (J_a, ψ_a, J_b, ψ_b) coordinate system becomes singular at these locations. Alternative coordinates are required to evaluate (1) whether a point is critical point or not, and if yes, (2) its linear stability. The

technical details are discussed in Appendix B. Only the following four prove to be truly critical points:

$$J_a = \pm K_a, J_b = 0 \quad \text{with (EE) stability} \tag{4.47}$$

$$J_a = 0, J_b = \pm K_a \quad \text{with (MM) stability} \tag{4.48}$$

4.3.2 Results of the $[N_b, 0]$ Polyads

Normal Modes at Low N_b Up to $N_b = 6$, there are two critical points at $J_a = \pm K_a$ with (EE) stability. They correspond to the normal **Trans** and **Cis** modes. This picture is consistent with the usual assumption that small-amplitude vibrations near equilibrium are dominated by the normal modes.

Bifurcation at Higher N_b With increasing polyad number N_b as well as energy, four bifurcations occur to **Trans** and **Cis** critical points. Four new families of critical points called the *Local* (**L**), *Precessional* (**Pre**), *Orthogonal* (**Orth**) and *Counter Rotator* (**CR**) emerge out of the normal mode critical points at the points of the bifurcations. The analytical solutions of these families are listed in Table 4.3 and eqns. (4.49-4.52).

TABLE 4.3 New families of critical points in the pure bending Hamiltonian.

Name	(ψ_a, ψ_b)	Stability
Local	$(0, 0)$	(EE)
Orthogonal	$\left(0, \frac{\pi}{2}\right)$	(EH)
Precessional	$\left(\frac{\pi}{2}, 0\right)$	(HH)
Counter Rotator	$\left(\frac{\pi}{2}, \frac{\pi}{2}\right)$	(EE)

$$\text{Local:} \quad J_a = 21.166 - 0.584K_a - 0.2681\sqrt{4091.902 + 42.376K_a - K_a^2} \tag{4.49}$$

$$\text{Orth:} \quad J_a = 24.876 - 0.496K_a - 0.8227\sqrt{531.865 + 32.598K_a - K_a^2} \tag{4.50}$$

$$\text{Pre:} \quad J_a = 10.920 - 0.564K_a - 0.4603\sqrt{-276.741 + 93.490K_a - K_a^2} \tag{4.51}$$

$$\text{CR:} \quad J_a = -18.312 - 0.536K_a + 0.6344\sqrt{309.356 + 143.457K_a - K_a^2} \tag{4.52}$$

At each of the four bifurcation points, either **Trans** or **Cis** changes its stability, and gives birth to one new family of critical points in the following manner

$$\textbf{Trans}\ (\text{EE}) \xrightarrow{N_b=7.63} \textbf{Trans}\ (\text{EH}) + \textbf{L}\ (\text{EE}) \tag{4.53a}$$

$$\textbf{Cis}\ (\text{EE}) \xrightarrow{N_b=9.56} \textbf{Cis}\ (\text{EH}) + \textbf{CR}\ (\text{EE}) \tag{4.53b}$$

$$\textbf{Trans}\ (\text{EH}) \xrightarrow{N_b=9.77} \textbf{Trans}\ (\text{HH}) + \textbf{Orth}\ (\text{EH}) \tag{4.53c}$$

$$\textbf{Trans}\ (\text{HH}) \xrightarrow{N_b=14.56} \textbf{Trans}\ (\text{EH}) + \textbf{Pre}\ (\text{HH}) \tag{4.53d}$$

The **Trans** family undergoes three consecutive bifurcations while the **Cis** family undergoes one. All six families involved in these bifurcations have $J_b = 0$,

and thus $\ell_4 = \ell_5 = 0$. The ratio J_a/K_a is presented in Fig. 4.4 as a function of N_b [5]. The ($J_a/K_a = \pm 1$) line corresponds to **Trans**/**Cis** critical points, respectively. At each bifurcation point, the new family appears at $J_a = \pm K_a$. Then they migrate towards J_a/K_a =0 with increasing N_b. This trend reflects increasingly equal mixing between the **Trans** and **Cis** modes in the new motions, which will be explained in detail below.

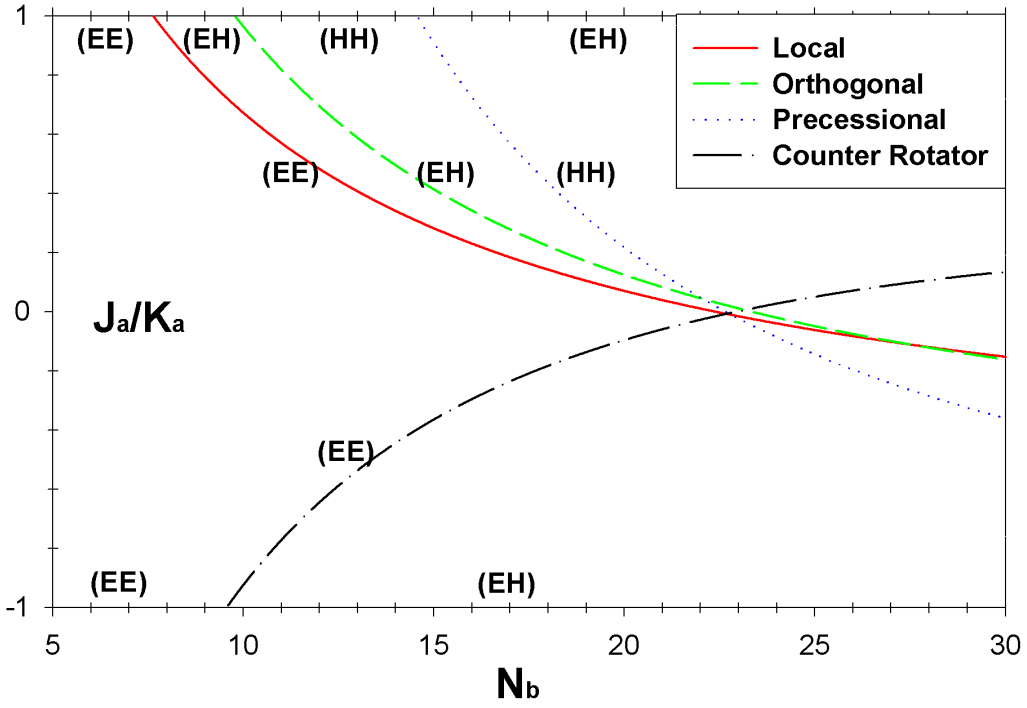

FIGURE 4.4 Bifurcation of critical points in $[N_b, 0]$ bending polyads. The four new families of critical points are shown on the figure, while the **Trans** and **Cis** coincide with the $J_a/K_a = \pm 1$ lines. Their stability before/after each bifurcation is also indicated on the figure.

Trajectories in the Full Phase Space The critical points in the reduced phase

[5]In Fig. 4.4, the bifurcation is calculated up to $N_b = 30$, although the effective Hamiltonian is based on spectra up to only $N_b = 22$.

space have two cyclic angles (θ_a, θ_b) that are absent from the Hamiltonian. θ_a corresponds to an overall translation in time while θ_b corresponds to a rotation of the system around the C-C axis [66]. According to the general argument in § 3.3.2, in the full phase space these critical points are quasiperiodic on a 2-dimensional invariant torus.

However, the $[N_b, 0]$ polyads have $K_b = 0$ and thus the frequency of θ_b is no longer physical. A proper analogy is that when one "shrinks" to zero the tube thickness of the invariant torus, quasiperiodic trajectories on its surface are reduced to *periodic orbits* with a single frequency $\dot{\theta}_a$. At the critical points the frequency of θ_b is zero when we substitute in $K_b = J_b = 0$:

$$\dot{\theta_b} = \left(\frac{\partial H}{\partial K_b}\right) = 2J_b(g_{44} + g_{45} + g_{55}) - \frac{S_{45}J_b\cos[2\psi_a] + R^*_{45}J_b\cos[2\psi_b]}{\Lambda}\times$$
$$(K_a^2 + J_a^2 - J_b^2) - \frac{R^*_{45} + 2g_{45}}{2}J_b\cos[2\psi_a]\cos[2\psi_b] = 0 \qquad (4.54)$$

This leaves only θ_a with non-zero frequency. Therefore, critical points found in the $[N_b, 0]$ polyads correspond to POs in the full phase space.

Visualization of Critical Point POs In order to understand the motions in a more intuitive manner, the periodic orbits in action-angle coordinates are transformed to the Cartesian coordinate. This is done by assuming each normal mode to be a 2-dimensional harmonic oscillator. Following the method in [66], the

normal Cartesian coordinates are:

$$x_4 = [(K_a + K_b + J_a - J_b)/\omega_4]^{1/2} \cos[(\theta_a + \theta_b + \psi_a - \psi_b)/2] + [(K_a - K_b + J_a + J_b)/\omega_4]^{1/2} \cos[(\theta_a - \theta_b + \psi_a + \psi_b)/2] \quad (4.55a)$$

$$y_4 = [(K_a + K_b + J_a - J_b)/\omega_4]^{1/2} \sin[(\theta_a + \theta_b + \psi_a - \psi_b)/2] - [(K_a - K_b + J_a + J_b)/\omega_4]^{1/2} \sin[(\theta_a - \theta_b + \psi_a + \psi_b)/2] \quad (4.55b)$$

$$x_5 = [(K_a + K_b - J_a + J_b)/\omega_5]^{1/2} \cos[(\theta_a + \theta_b - \psi_a + \psi_b)/2] + [(K_a - K_b - J_a - J_b)/\omega_5]^{1/2} \cos[(\theta_a - \theta_b - \psi_a - \psi_b)/2] \quad (4.55c)$$

$$y_5 = [(K_a + K_b - J_a + J_b)/\omega_5]^{1/2} \sin[(\theta_a + \theta_b - \psi_a + \psi_b)/2] - [(K_a - K_b - J_a - J_b)/\omega_5]^{1/2} \sin[(\theta_a - \theta_b - \psi_a - \psi_b)/2] \quad (4.55d)$$

These are related to the local coordinates (x_1, y_1, x_2, y_2) shown in Fig. 4.5 by

$$x_1 = x_4 + x_5, \qquad y_1 = y_4 + y_5 \quad (4.56)$$

$$x_2 = -x_4 + x_5, \qquad y_2 = -y_4 + y_5 \quad (4.57)$$

In order to visualize the resulting POs in 3-dimensional space, they are converted into animations with the modeling software *Bryce 4*. The animations for N_b =22 are included on the accompanying CD-ROM in *QuickTime 4* format [97]. Fig. 4.6 illustrates these animations by superimposing some of the still frames. The trajectories of **L** and **Pre** are both planar and resemble their namesakes in [76]. **L** has most of the amplitude of bending in one C-H bending oscillator (bender) while the other C-H bender has very little. **Pre** has the two C-H benders at equal

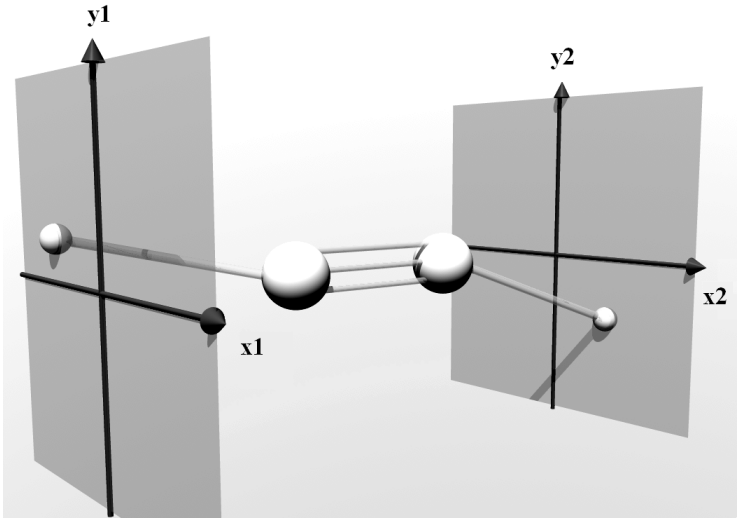

FIGURE 4.5 Cartesian bending coordinates, as defined in eqns. (4.56,4.57).

amplitude but out of phase by $\pi/2$. For **Orth**, the two benders vibrate on planes orthogonal to each other, and reach their turning points in phase. For **CR**, the two hydrogens rotate in ellipses (circles) in opposite directions at the two ends of the molecule.

Immediately after each bifurcation, the trajectories resemble the respective "parent" normal mode motions. In Fig. 4.4, this is where the new family of critical points is still close to $J_a = \pm K_a$. As the family migrates towards J_a/K_a =0, the Cartesian trajectory more and more resembles the ideal motion in Fig. 4.6. For example, the **L** trajectory initially resembles a slightly asymmetrical trans bend. Then the imbalance of amplitude between the two C-H benders increases with

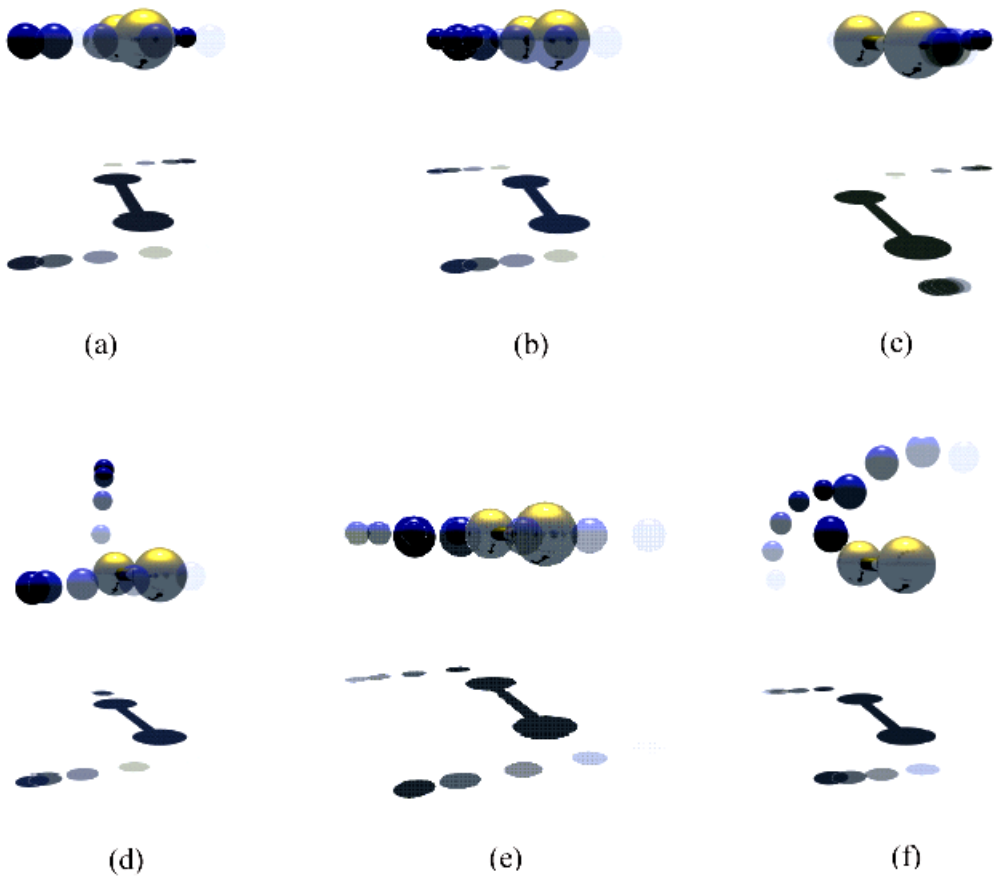

FIGURE 4.6 Cartesian periodic orbits corresponding to critical points in $[22, 0]$ polyad, produced from still frames in the computer animation. The carbon and hydrogen atoms are represented by the large and small spheres, respectively. The panels refer to (a) **Trans**; (b) **Cis**; (c) **L**; (d) **Orth**; (e) **Pre**; (f) **CR** critical points.

N_b. Finally, at N_b =22 where $J_a/K_a \approx 0$, almost all the amplitude is in one of the two oscillators.

An examination of the V_{DDI} and V_ℓ terms in (4.27, 4.28) reveals that both contribute negatively to the Hamiltonian when $(\psi_a, \psi_b) = (0, 0)$, and most positively when (ψ_a, ψ_b) = $(\pi/2, \pi/2)$. The **L** and **CR** critical points correspond to the global extrema points of the reduced Hamiltonian. **L** has the lowest energy while **CR** has the highest. Hence, the **L** and **CR** are stable modes of vibration because

of the limited phase space volume at the top and bottom of the energy range (§ 3.3.2).

In summary, critical points analysis of the $[N_b, 0]$ polyads yields four new families of critical points, in addition to the **Trans** and **Cis** normal families. The low-energy (EE) stability of **Trans** and **Cis** is destroyed in their first bifurcations. Due to the special condition $K_b = \ell = 0$, the frequency of one cyclic angle $\dot{\theta}_b$ vanishes for all critical points. Therefore, they correspond to POs in the full phase space.

4.3.3 Results of the $[N_b, \ell]$ Polyads

The $\ell \neq 0$ cases have not been considered by any other research groups. The critical point analysis, in contrast, can be extended to arbitrary ℓ values (although the validity of the effective Hamiltonian beyond $\ell = 2$ is questionable due to a lack of supporting experimental data). Here we present critical points in the $[N_b, 2]$, $[N_b, 6]$ and $[N_b, 10]$ polyad series (with $K_b = \ell/2 = 1, 3, 5$, respectively) as preliminary predictions, and as a demonstration of this significant extension of our methods.

Similar to the $\ell = 0$ case, eqns. (4.33, 4.34) are solved with (ψ_a, ψ_b) held fixed at the four values listed in (4.44). However, it is no longer true that eqn. (4.34) has the trivial solution $J_b = 0$, as in the $\ell = 0$ case. Instead, (4.33, 4.34) must be solved simultaneously for J_a and J_b values. The solutions are numerically found by first transforming these equations into a polynomial form, then solving

them using the homotopy continuation package *PHCpack* [98]. This package has no limitation on the number and form of polynomials to solve, and can be used with no preliminary knowledge about the solutions. The solutions are further subject to the constraint

$$K_a - K_b \geq |J_a + J_b|, \qquad\qquad K_a + K_b \geq |J_a - J_b|$$

in order that the actions I_{4d}, I_{4g}, I_{5d} and I_{5g} in eqn. (4.18) are all non-negative.

The $J_a/K_a, J_b/K_a$ values of non-normal critical points are plotted against N_b in Fig. 4.7. The solutions for each of the 4 (ψ_a, ψ_b) conditions are named in the same way as for the $\ell = 0$ case (Table 4.3). In panels (a), (c) and (e), all families branch out of the **Trans** and **Cis** normal modes in a manner similar to the $\ell = 0$ results (Fig. 4.4). The lower panels illustrate that these critical points are not restricted to $J_b = 0$. Instead, they diverge from $J_b = 0$ with increasing ℓ.

The close resemblance between Fig. 4.4 and panel (a) of Fig. 4.7 is consistent with the observation that in DF spectra the $\ell = 0/2$ states have indistinguishable intensity patterns. Were the dynamics vastly different for these two ℓ values, the resulting fractionation patterns of the bright states are expected to be different. At higher ℓ values, our analysis reveals interesting bifurcation structures, which awaits further interpretation. Even though the quantitative predictions here are limited by the validity of the effective Hamiltonian, we nevertheless expect the vibrational dynamics with sufficiently high ℓ to become qualitatively different from the $\ell = 0$ case.

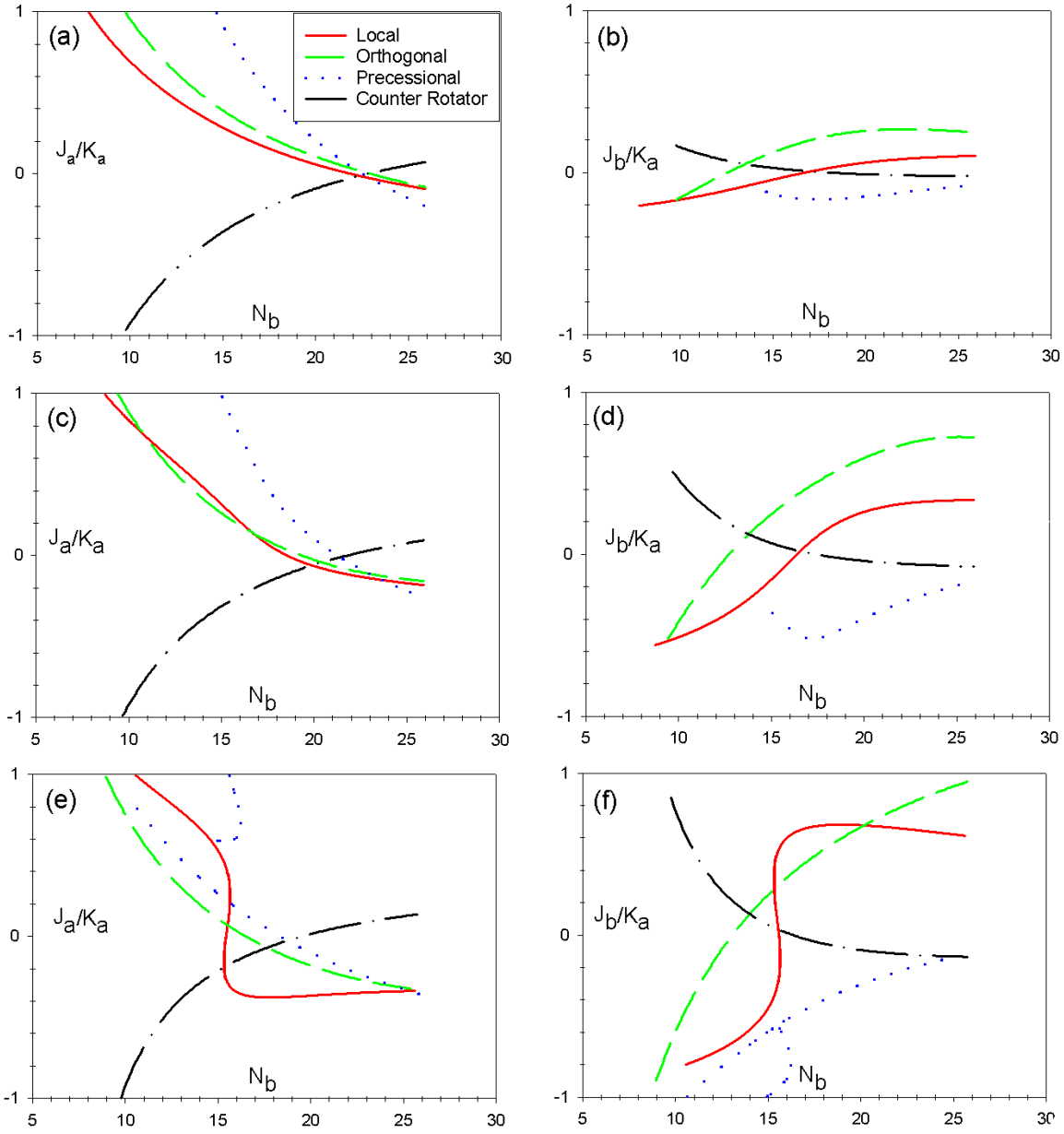

FIGURE 4.7 Bifurcation of critical points in $[N_b, \ell]$ bending polyads. Panels (a), (b): $\ell = 2$; (c), (d): $\ell = 6$; (e), (f): $\ell = 10$. The upper panels display J_a/K_a vs. N_b, while the lower panels display J_b/K_a vs. N_b values.

In spite of their similarity, the physical trajectories corresponding to the $\ell = 0$ and $\ell \neq 0$ critical points have different natures. In the former case they are periodic orbits and in the latter quasiperiodic orbits on 2-dimensional invariant tori. The claim made by Jacobson *et al.* that "a fixed point in the abstract action-angle space ... must lift to a periodic orbit in the physical coordinates of the molecule ... that lies on a full dimension torus" [66] is accurate only when applied to the $\ell = 0$ case. Generally, there exist as many independent frequencies as the number of additional constants of motion (polyad numbers). *It is the critical points in reduced phase space, not the POs in the full phase space, that are the centers of phase space organization.*

4.4 Discussion of Bifurcation Results

4.4.1 Comparison with Other Studies

The pure bending Hamiltonian was analyzed by Jacobson *et al.* in a numerical manner. They first visually examined sequences of SOS to identify stable fixed points at the center of regular phase space regions. The stable fixed points are then followed while the energy is varied *within the same polyad* N_b. A "family tree" of these fixed points is then built within N_b =16 [99] and $N_b = 22$ [66]. They found a *local* fixed point at the bottom and a *counter rotator* fixed point at the top energy end of these polyads. The fixed points were used to assign eigenstates based on the nodal pattern of the semiclassical wavefunctions.

The local and counter rotator fixed points correspond to our critical points with the same names, as they occupy the same phase space region [6]. There is another fixed point these authors called the "M_2 mode", which appears to be related to our **Orth** family of critical points. Reproduced in Fig. 4.8 from Jacobson *et al.* is the stable M_2 PO trajectory they found in $N_b = 22$. The motion qualitatively resembles panel (d) of Fig. 4.6, with the two C-H bonds bending in phase with each other. Jacobson *et al.* observed numerically that this PO family becomes unstable below $14,161$ cm^{-1} within this polyad, which is consistent with our **Orth** critical point with (EH) stability at energy $14,114$ cm^{-1}. At this stage, we believe that the M_2 family (both the stable and unstable segments) is formed by *secondary* POs surrounding the **Orth** critical point, which corresponds to a *primary* PO [39]. This speculation remains to be verified numerically.

We have to mention that Champion *et al.* had deduced the existence of **L**, **CR** and **Orth**-types of modes as idealized cases using Lie algebraic analysis of the same bending Hamiltonian [73], even though they did not perform a bifurcation analysis with variable polyad numbers. Moreover, the **L** and **CR** modes are independently verified in *ab initio* quantum eigenfunction calculations [86] as well as numerical PO search on molecular PES [75].

According to our analysis, the **Pre** family is bi-unstable and therefore ex-

[6]Specifically, in [66] the local mode states are localized around (ψ_a, ψ_b)=$(0, 0)$, and the counter rotator mode states are around (π, π). Their ψ_a and ψ_b are defined as twice ours.

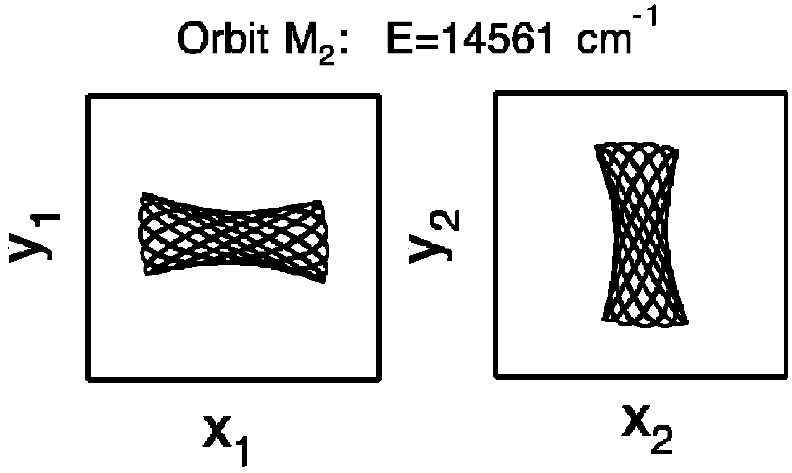

FIGURE 4.8 The M_2 trajectories calculated by Jacobson *et al.* in Fig. 3 of [66], with N_b =22.

pected to be surrounded by chaos. Thus this family is not apparent in the study by Jacobson *et al.* , which relies on inspection of SOS for *regular* regions. Their SOS (reproduced below as Fig. 4.9) at nearby energies shows only a strongly chaotic region.

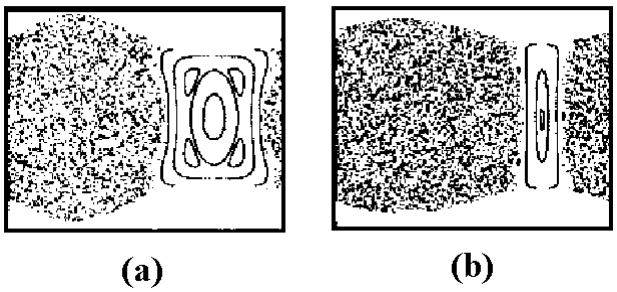

FIGURE 4.9 SOS near the **Pre** critical point, calculated by Jacobson *et al.* and adapted from Fig. 1 of [99].

4.4.2 Summary of Method

Compared to the procedure of Jacobson *et al.* , our critical points analysis is much more efficient in picking out new and relevant phase space structures. In the former, a large number of SOS taken at different directions and energy are examined. In contrast, finding critical points in the reduced phase space involves solving simultaneous analytic equations. Yet, in the current case, almost all the significant observations from inspecting the SOS (specifically, those with manifestation in the quantum wavefunctions) can be obtained through four families of critical points.

In the reduced Hamiltonian, time evolutions of the cyclic variable(s) are formally factored out and not considered as the essential part of dynamics. The critical points are determined in a uniform manner, regardless of how many (≥ 1) polyad numbers there are. Hence, we are able to carry the same critical points analysis to both $\ell = 0$ and $\ell \neq 0$ cases. At high ℓ values, the latter cases display additional bifurcations that have not been observed elsewhere.

Moreover, the usage of SOS is almost exclusively reserved for 2 DOF systems. With 3 DOF, the phase space is 6-dimensional. A 2-dimensional surface does not have the correct dimensionality to divide it. Therefore, such a surface is at most limited to short times because the trajectories soon stop intersecting it [100]. The generalized SOS are 4-dimensional "hyper slices" whose visualization is not trivial [101]. Analytic detection of interesting dynamics (without visual

inspection) becomes essential for analyzing systems with 3 or more DOF. The critical points analysis is such a choice. The number of equations scales *linearly* with the DOF, and it is theoretically possible to find all the roots in a comprehensive and accurate manner. The resulting critical points then enables a guided exploration of the phase space using other techniques, including visualization.

4.5 Effect of Single DD-I or ℓ Resonance

In this section, we propose an interpretation of the bifurcations in the full 4 DOF H_{bend} in terms of the individual resonances, namely the DD-I and the ℓ resonances. The DD-II is ignored due to its relative weakness. With either of these resonances alone, a $[N_b, \ell]$ polyad is further separated into subpolyads. The DD-I subpolyads are along the columns in Fig. 4.3, while the ℓ resonance subpolyads are along the rows. The corresponding Hamiltonians $H_0 + V_{DDI}$ and $H_0 + V_\ell$ both have two modes connected by a $2:2$ resonance.

These Hamiltonians can be analyzed using the method described in Chapter 3.1. The $H_0 + V_{DDI}$ Hamiltonian (H_{DDI}) is parameterized by two reduced phase space variables J_a, ψ_a according to eqns. (4.18). Within each subpolyad, these parameters define a DD-I PPS. Similarly, the $H_0 + V_\ell$ Hamiltonian (H_ℓ) is parameterized by J_b and ψ_b, which define an ℓ PPS for each subpolyad. For simplicity, we only consider the $[N_b, 0]$ polyads without the high-order coefficients y_{ijk}, r_{445} and r_{545}. Then the DD-I PPS has radius $K_a - |J_b|$ while the ℓ PPS has

radius $K_a - |J_a|$.

Fig. 4.10 presents the zero-order DD-I and ℓ PPS, and the semiclassical trajectories on them. With only the H_0 term, this is a trivial case because the Hamiltonian does not depend on ψ_a or ψ_b. All semiclassical trajectories of H_0 can be regarded as the "composition" between one DD-I trajectory and one ℓ trajectory, as labeled in the figure. The critical points on the PPS are where

$$\frac{\partial H_{DDI}}{\partial J_a} = \frac{\partial H_{DDI}}{\partial \psi_a} = 0 \qquad \text{or} \qquad \frac{\partial H_\ell}{\partial J_b} = \frac{\partial H_\ell}{\partial \psi_b} = 0 \tag{4.58}$$

In the zero-order case, the only critical points are the north and south poles of each PPS.

The DD-I and ℓ PPS for polyads $[4,0]$, $[12,0]$ and $[20,0]$ are presented in Figs. 4.11-4.13. Note that the two sets of spheres do not coexist within the same Hamiltonian. The zero-order quantum numbers on these figures are no longer meaningful in labeling the trajectories in H_{DDI} and H_ℓ, since n_4, n_5 (or ℓ_4, ℓ_5) are mixed by the resonance term. As the DD-I and ℓ PPS do not qualitatively change across the subpolyads with same N_b, in the latter two figures the number of PPS is reduced to make the figure legible.

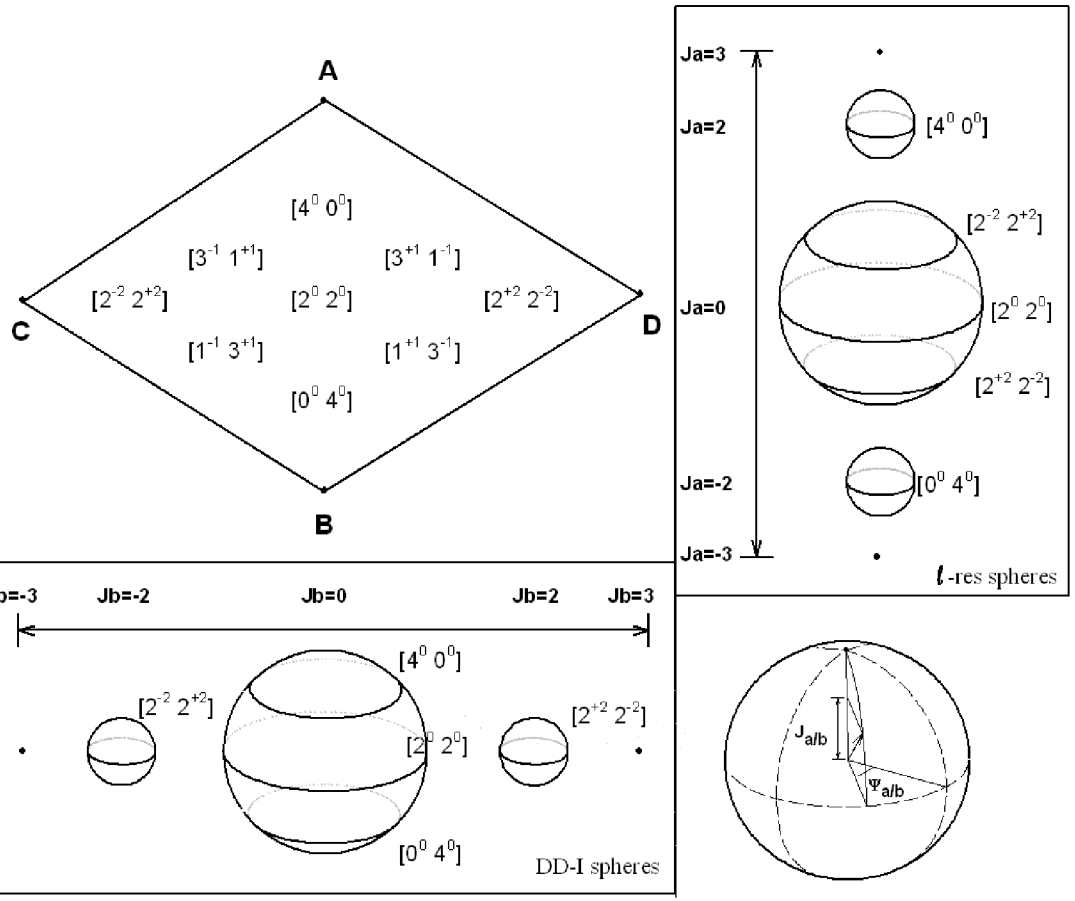

FIGURE 4.10 Quantum states and PPS of the zero-order system H_0. Corresponding to each column is a DD-I PPS parameterized by (J_a, ψ_a). Corresponding to each row is an ℓ PPS parameterized by (J_a, ψ_a). The sphere shrinks to a point at the corners A, B, C and D, where J_a or J_b vanishes.

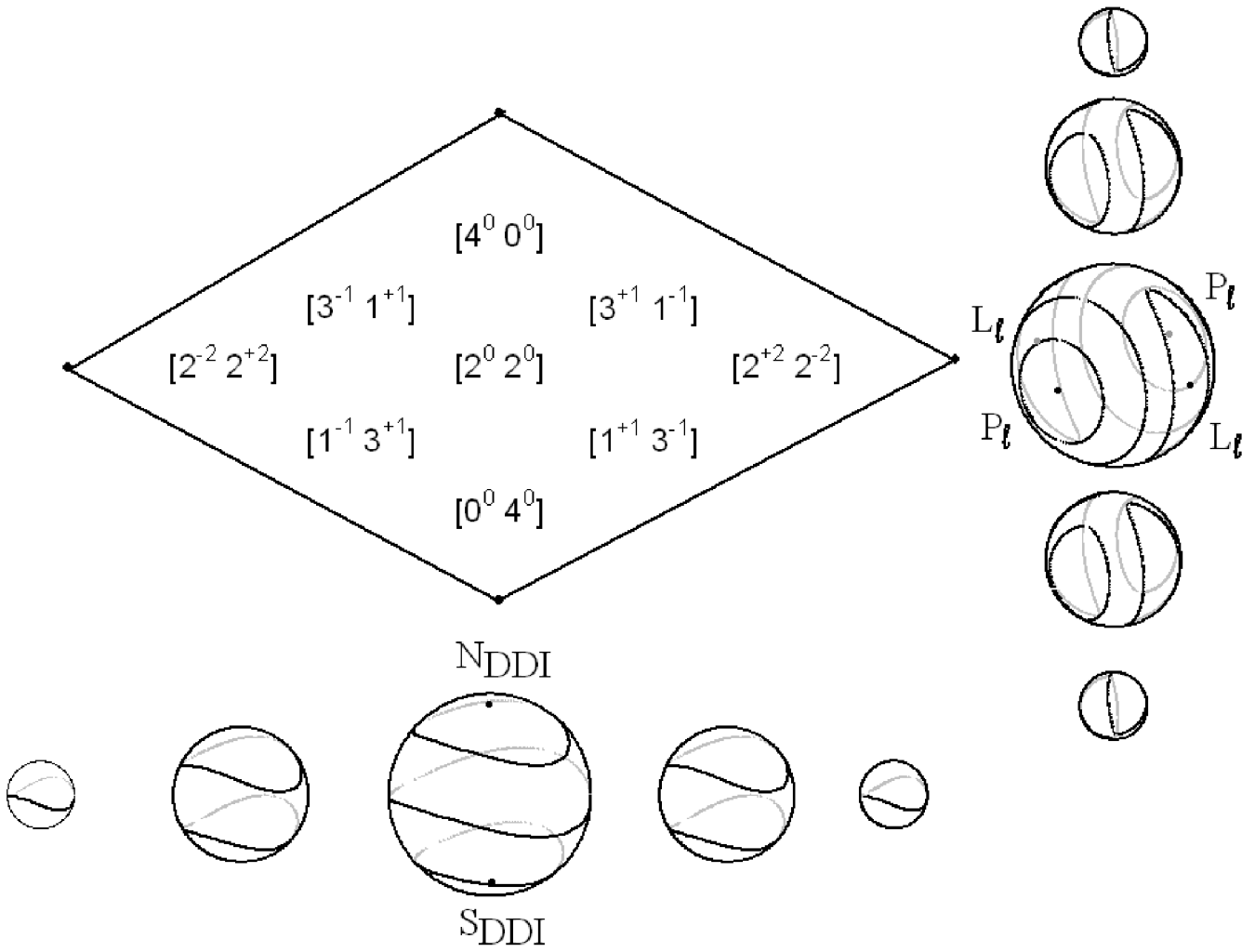

FIGURE 4.11 DD-I and ℓ resonance PPS in $[4, 0]$ polyad.

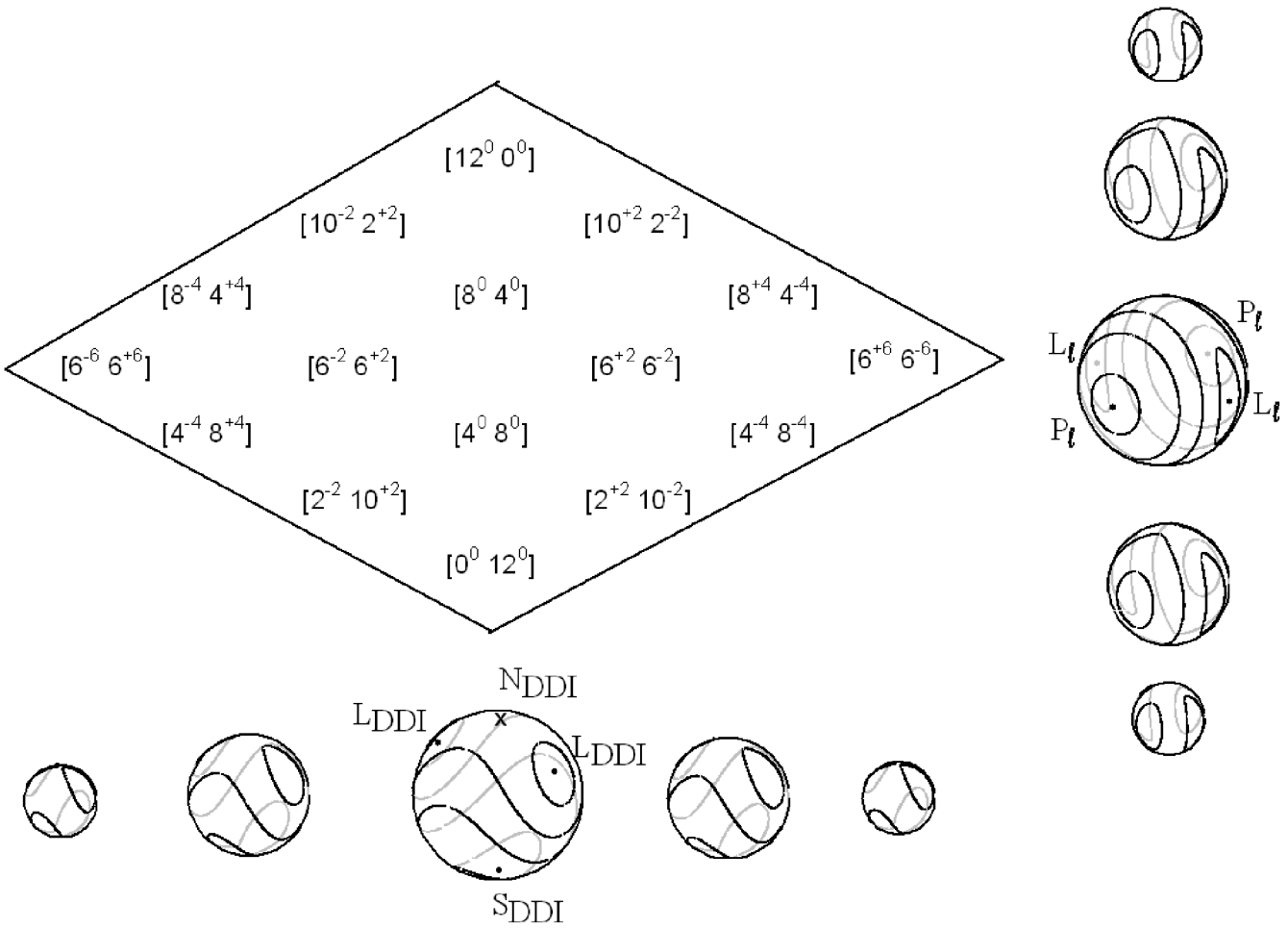

FIGURE 4.12 DD-I and ℓ resonance PPS in $[12, 0]$ polyad. Only selected PPS are shown.

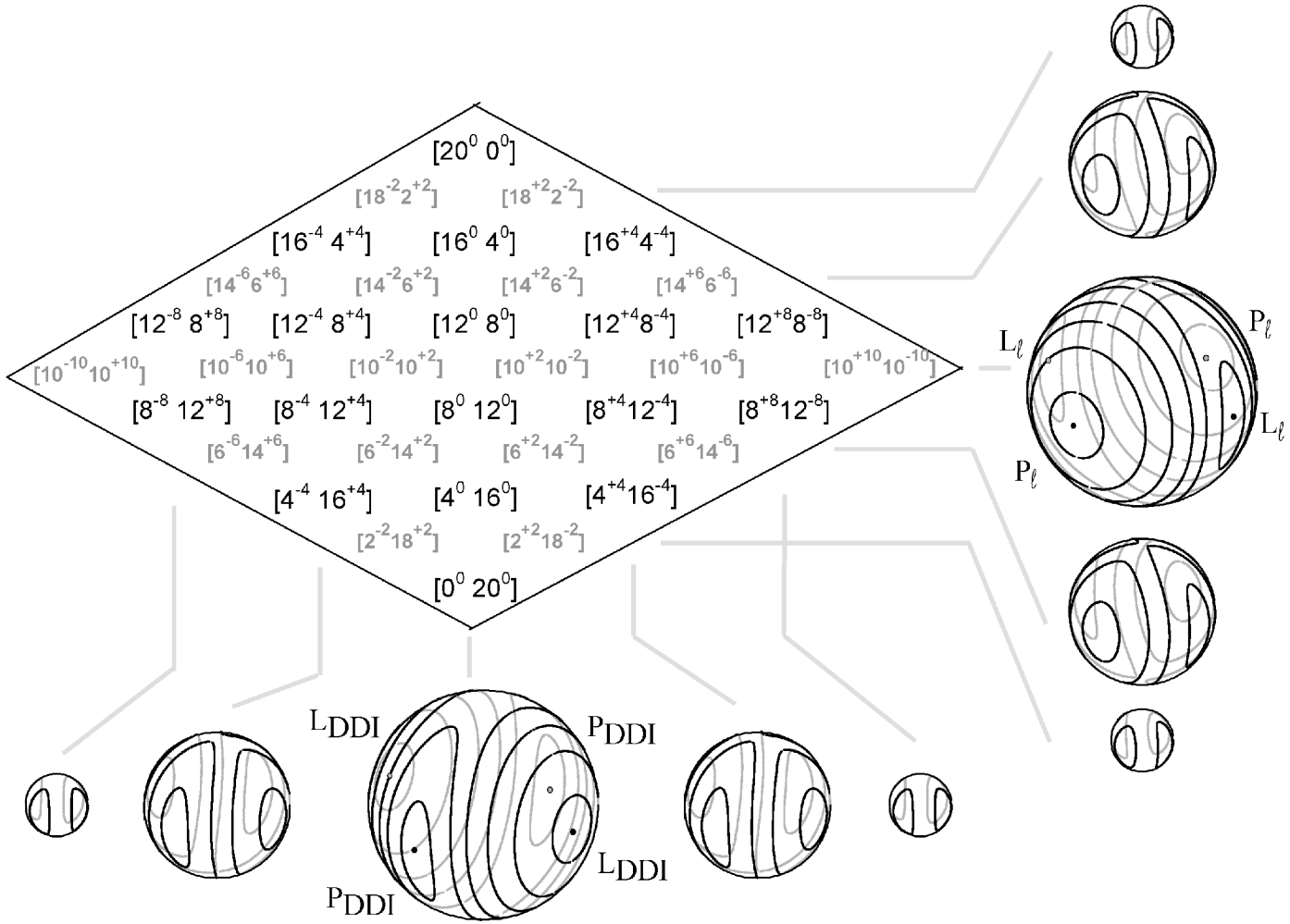

FIGURE 4.13 DD-I and ℓ resonance PPS in $[20, 0]$ polyad. Only selected PPS are shown, as indicated by the grey lines.

The H_{DDI} System This Hamiltonian had been considered previously by Rose and Kellman [76] with slightly different parameters, with the same qualitative results. A comparison across Figs. 4.11-4.13 shows that as N_b increases, two new families of critical points emerge in two bifurcations. Between N_b =6 - 8 (Figs. 4.11, 4.12), two *local* mode critical points L_{DDI} are born at the north pole of the PPS onto the great circle ($\psi_a = 0, \pi$). Then between N_b =14 -16 (Figs. 4.12, 4.13) two *precessional*-type critical points P_{DDI} emerge at the south pole of the PPS onto another great circle ($\psi_a = \frac{\pi}{2}, \frac{3\pi}{2}$). Both L_{DDI} and P_{DDI} migrate towards the equator of the PPS (where J_a =0) with increasing N_b.

The migration of the L_{DDI} and P_{DDI} is depicted in Fig. 4.14, which plots these critical points in the same manner as Fig. 4.4. Similar to Fig. 4.4, here both critical points in H_{DDI} are born at $J_a/K_a \approx 1$ and migrate towards the equator, finally reaching $J_a/K_a = 0$ at about $N_b = 20$.

Fig. 4.15 summarizes the structure of the central DD-I PPS (N_b =4-20) on the $2:2$ catastrophe map. The control parameters $\delta_{DDI}, \beta'_{DDI}$ are defined in eqns. (4.1-4.2) of [76]. β' characterizes the strength of the 2:2 resonance, while δ reflects the detuning between the two coupled frequencies. Here, the resonance strength s_{45} is a constant. The trans- and cis- bending frequencies, starting as $\omega_4 < \omega_5$, are tuned towards each other as $x_{55} < 0 < x_{44}$. The representative points on Fig. 4.15 cross two zone boundaries as N_b increases: first the trans- normal critical point

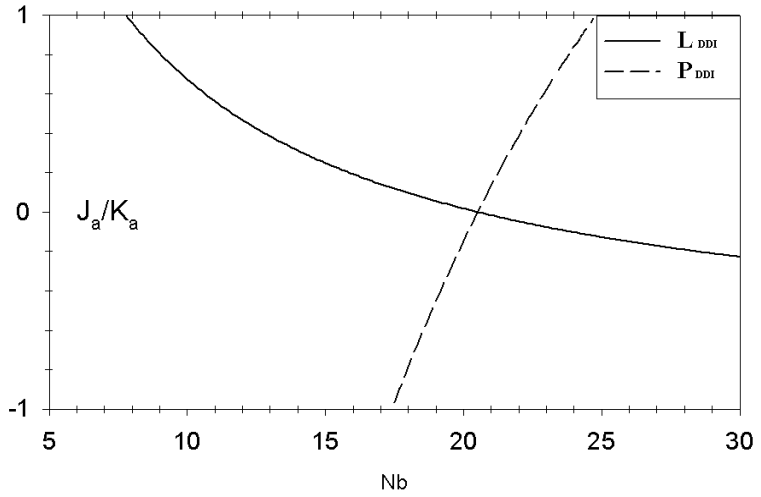

FIGURE 4.14 Bifurcation diagram of H_{DDI}. Only the central column ($\ell_4 = \ell_5 = 0$) of each polyad is shown.

(north pole) is destabilized in a bifurcation, then the cis- normal critical point is destabilized by another bifurcation at higher polyad number.

Ref. [76] assumes a planar model of C_2H_2, and predicts the L_{DDI} and P_{DDI} critical points (see Fig. 1 thereof) to have the same Cartesian motion as the **L** and **Pre** critical points in Fig. 4.6. These two motions can be interpreted in the following simple way. The angle ψ_a is defined as the relative phase between the trans- and cis- normal mode oscillators. When exactly in resonance, these two oscillators have the same frequency. As shown in Fig. 4.17 (a) and (b), superimposing two such oscillators on the same plane with relative phases 0 or π results in only one C-H bending motion being excited (**L**). Changing the relative phase to $\pi/2$ or $3\pi/2$ causes the two C-H benders to be out of phase by $\pi/2$ or $3\pi/2$ (**Pre**).

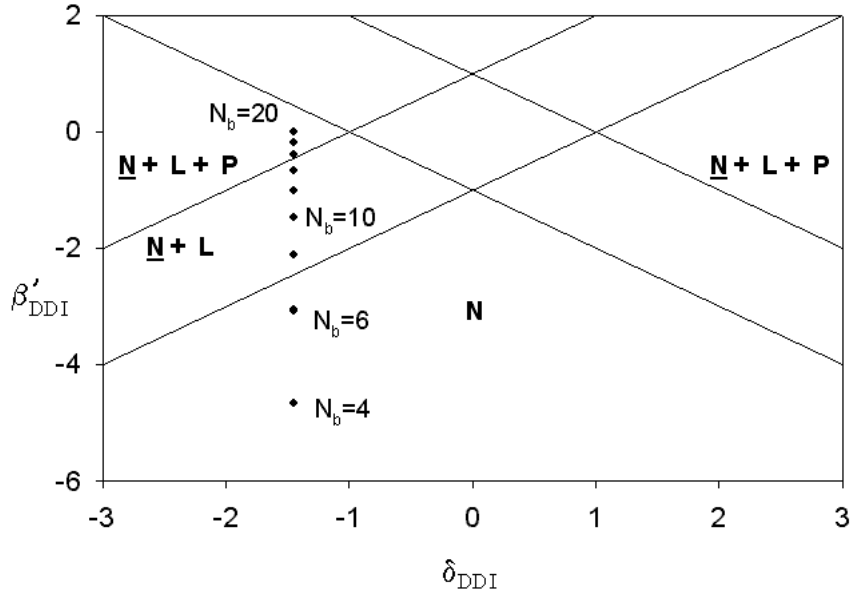

FIGURE 4.15 Catastrophe map of single DDI resonance Hamiltonian H_{DDI}. The representative points are for the central PPS with N_b = 4-20. **N**, **L** and **P** denote the Normal, Local and Precessional critical points. The unstable critical points of a given region are underlined.

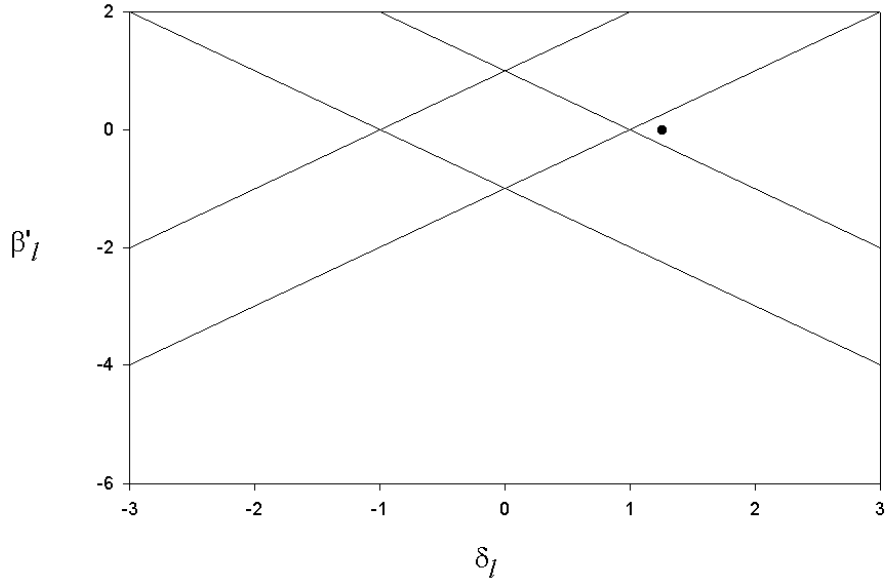

FIGURE 4.16 Catastrophe map of single ℓ resonance Hamiltonian H_ℓ. The zone structures are the same as Fig. 4.15. At all N_b values, the representative points of the central PPS are located at the same point.

The H_ℓ System Unlike H_{DDI}, the Hamiltonian H_ℓ contains a special degeneracy condition. The quantum ZOS $|n_4^{\ell_4}, n_5^{\ell_5}\rangle$ and $|n_4^{-\ell_4}, n_5^{-\ell_5}\rangle$ always have the same energy. This is a consequence of the time reversal symmetry, when the directions of both angular momenta ℓ_4, ℓ_5 are reversed [102]. In other words, the two "frequencies" coupled by V_ℓ are always in exact resonance. Any finite V_ℓ coupling will induce a non-local bifurcation on the zero-order system [15]. Such a bifurcation of critical points is indeed shown in a comparison of the ℓ PPS between Figs. 4.10 and 4.11. When V_ℓ is turned on, both poles of the sphere are unstable. The following two new families are stable critical points:

$$\mathrm{L}_\ell: \quad J_b = 0, \quad \psi_b = 0, \pi \tag{4.59}$$

$$\mathrm{P}_\ell: \quad J_b = 0, \quad \psi_b = \frac{\pi}{2}, \frac{3\pi}{2} \tag{4.60}$$

H_{DDI} and H_ℓ share the same zone structure on the catastrophe map because they are both formally $2:2$ resonances. The coupling strength here is taken to be r_{45}^0 (which is a constant), and $\beta' \equiv 0$. On the catastrophe map, the representative points for the central ℓ subpolyads in Figs. 4.11-4.13 share a single location for all N_b values. This is shown in Fig. 4.16, which is very different from the DD-I case in Fig. 4.15.

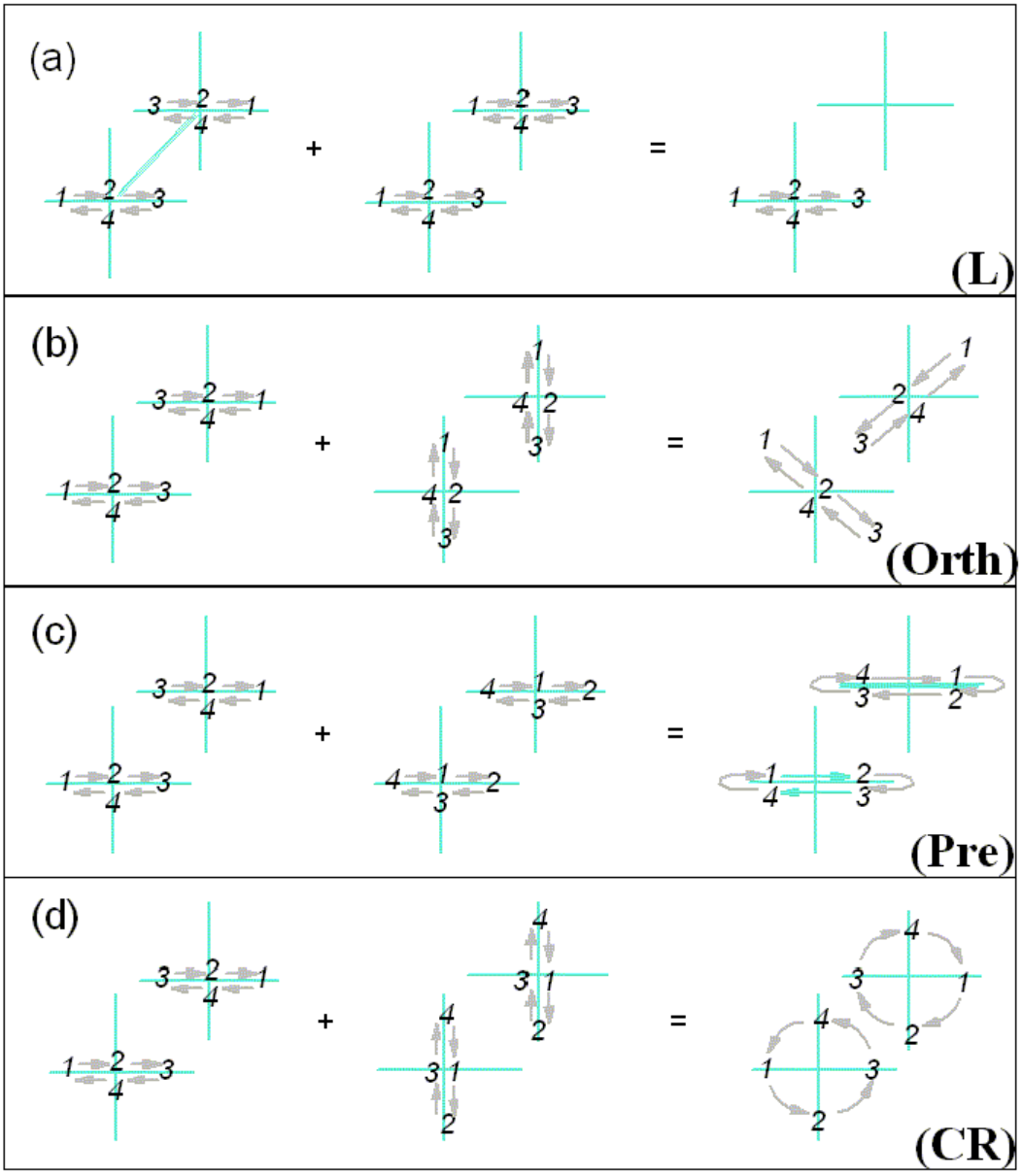

FIGURE 4.17 New bending modes as superposition of the normal trans- and cis- modes. The coordinates are defined as in Fig. 4.5, and the trans- and cis- vibrations are assumed to be at the same frequency and amplitude. In panels (a) - (d), the relative (phase angle, dihedral angle) between the normal mode oscillators are $(0, 0)$, $(0, \pi/2)$, $(\pi/2, 0)$ and $(\pi/2, \pi/2)$ respectively. Superimposing trans- (first column) and cis- (second column) motion result in the four new types of motion found through critical points analysis.

The L_ℓ and P_ℓ modes are formally like the local and precessional modes in the DD-I system, although the angles ψ_a and ψ_b have very different meanings. While ψ_a is the relative phase angle between planar trans- and cis- motions, the physical interpretation of ψ_b is rather complex. When $\ell_4 = \ell_5 = 0$, ψ_b corresponds to the dihedral angle between the two planar normal C-H benders.

Connection with Bifurcations in the Full Hamiltonian A comparison between the critical points in H_{DDI} and H_ℓ and those found in the full H_{bend} of § 4.4 reveals the following connections:

1. The 16 conditions of (ψ_a, ψ_b) for critical points in H_{bend} (Table 4.2) can be produced from combining the great circles on DD-I and ℓ PPS. Table 4.2 can thus be regarded as a set of generalized great circles in H_{bend}.

2. DD-I resonance induces bifurcations in the (J_a, ψ_a) coordinates with increasing N_b. The new L_{DDI} and P_{DDI} then migrate towards $J_a = 0$. The ℓ-resonance, on the other hand, induces L_ℓ and P_ℓ in the (J_b, ψ_b) coordinates as soon as V_ℓ is included. Both new families are located at J_b =0. There is no additional bifurcation in H_ℓ as N_b increases. All these observations are consistent with the results in Fig. 4.4.

3. Superimposing equal amounts of trans- and cis- vibrations at the same frequency, with relative phase angle ψ_a and dihedral angle ψ_b produces the same non-normal Cartesian trajectories as in Fig. 4.6. Superpositions with

(relative phase, dihedral angle) at $(0, 0)$ and $(0, \pi/2)$ result in the **L** and **Orth** type trajectories respectively (see (a), (b) of Fig. 4.17), while $(\pi/2, 0)$ and $(\pi/2, \pi/2)$ result in the **Pre** and **CR** type vibrations (see (c), (d) of Fig. 4.17).

4. Intuitively, the critical points in the full system can be regarded as formed from one critical point in H_{DDI} and one in H_ℓ, in the manner listed in Table 4.4. The bifurcations along N_b are caused by DD-I, while the nature of the four new modes is determined by both DD-I and ℓ terms.

TABLE 4.4 Proposed composition of critical points in H_{bend} from those in H_{DDI} and H_ℓ. The notations in columns 1 and 3 refer to Figs. 4.11-4.13.

H_{DDI} and H_ℓ	H_{bend}	H_{DDI} and H_ℓ	H_{bend}
N_{DDI}, L_ℓ	**Trans**	L_{DDI}, L_ℓ	**L**
N_{DDI}, P_ℓ	**Trans**	P_{DDI}, L_ℓ	**Orth**
S_{DDI}, L_ℓ	**Cis**	L_{DDI}, P_ℓ	**Pre**
S_{DDI}, P_ℓ	**Cis**	P_{DDI}, P_ℓ	**CR**

This composition is only a qualitative one. Most importantly it fails in predicting the stability of critical points in the full system. Although all new critical points in H_{DDI} and H_ℓ are stable, those in H_{bend} exhibit three different types of stability. Only the **L** and **CR** families are bi-stable (EE). These differences are likely to be caused by the fact that in the full Hamiltonian, the two directions (J_a, ψ_a) and (J_b, ψ_b) are strongly coupled to each other instead of forming independent subsystems.

4.6 Quantum Survival Probability of Bending States

Due to its resemblance to the transition state of Fig. 4.1, the local bending mode is expected to play an important role in the isomerization process. Carter *et al.* recently performed a Car-Parrinello calculation of the acetylene-vinylidene system [103]. Dozens of classical trajectories are integrated, with the force field at each step obtained from *ab initio* calculation. Surprisingly, many trajectories go back and forth across the potential barrier many times before settling in the acetylene well. The authors give a kinematic explanation: The time interval between the hydrogen crossing the barrier and swinging back is not long enough for the energy in the reaction coordinate to dissipate effectively. This interpretation reconciles the discrepancy of vinylidene lifetime measured at two different timescales in earlier studies – 0.04-4.6 ps in [104,105] and 3.5 μs in [106]. The picosecond timescale is believed to be that of the initial decay of vinylidene, while the microsecond is the decay time averaged over many recrossings.

In the frequency domain, such a "recurring state" is decoupled from the rest of the vibrational manifold. This is supported by the observation of Levin *et al.* [106]. In their Coulomb explosion experiment, while the vinylidene molecules have energy well above the reaction barrier, the estimated dilution factor (more on this later) is only $\approx$ 0.5, indicating that this is coupled to one other state. Schork and Köppel compared the intrinsic lifetime of vinylidene to the local density of acetylene vibrational states, and concluded that extensive IVR is

unlikely, at least for the lowest vibrational state of vinylidene [107]. In addition, Srivastava *et al.* also suggested the acetylene-vinylidene isomerization is going to be far from the RRKM limit due to the relatively low density of states [108].

The survival probability $P(t)$ has been an important tool in characterizing the dynamics of quantum states [72,109]. For a quantum state $|\Psi\rangle$ written as an expansion in the eigenstate basis

$$|\Psi(t)\rangle = \sum c_i \, e^{-iE_i t/\hbar} |\phi_i\rangle \tag{4.61}$$

$P(t)$ is defined as the overlap between $|\Psi(0)\rangle$ and $|\Psi(t)\rangle$:

$$\begin{aligned} P(t) =& |\langle \Psi(t)|\Psi(0)\rangle|^2 = |(\sum_i \langle \phi_i | c_i^* e^{iE_i t/\hbar})(\sum_j c_j |\phi_j\rangle)|^2 \\ =& (\sum_i |c_i|^2 \cos[E_i t/\hbar])^2 + (\sum_j |c_j|^2 \sin[E_j t/\hbar])^2 \\ =& \sum_i |c_i|^4 + 2 \sum_{i,j;i\neq j} |c_i|^2 |c_j|^2 \cos[(E_i - E_j)t/\hbar] \end{aligned} \tag{4.62}$$

The survival probability of an eigenstate is trivial: $P(t) \equiv 1$. For other initial states, the rate of the initial decay from $P(0) = 1$ is determined by the states to which $|\Psi\rangle$ is *directly* coupled [110]. Later oscillations (quantum beats) in $P(t)$ reflect the (usually partial) recurrence of the initial state. Finally, the long time average $\sum |c_i|^4$, also known as the *dilution factor* [3], gives an estimate of the number of states participating in the IVR of the initial state.

$P(t)$ is the quantum analogue of the classical autocorrelation function [111]. For an eigenstate, $P(t) \equiv 1$. Otherwise when the state $P(t)$ remains near unity for

a sufficiently long time, then $|\Psi\rangle$ is strongly localized in some representation (as opposed to spreading over all space). In the statistical (RRKM) limit, the value of $P(t)$ is approximately equal to the local density of states that are symmetry-allowed to couple to the initial state.

In § 3.3.2, we hypothesized that the extremum critical points correspond to localized states. In order to test this claim in the case of the C_2H_2 bending Hamiltonian, $P(t)$ of states corresponding to **Trans**, **Cis**, **L** and **CR** critical points are calculated for polyads $N_b = 2$ to 20. While the **Trans** and **Cis** states are the normal ZOS $|n_4^0, 0^0\rangle$ and $|0^0, n_5^0\rangle$, the **L** and **CR** states have to be constructed. Here we use the method described by Field *et al.* in [72], which also contains calculation of $P(t)$ for selected **L** states. The **L** and **CR** states are defined as [7]:

$$|\mathrm{L}_n(0)\rangle = \frac{1}{2^{n/2}}(\hat{a}_{4d}^\dagger + \hat{a}_{5d}^\dagger)(\hat{a}_{4g}^\dagger + \hat{a}_{5g}^\dagger)^{\frac{n}{2}}|0^0, 0^0\rangle \tag{4.63}$$

$$|\mathrm{CR}_n(0)\rangle = \frac{1}{2^{n/2}}(\hat{a}_{4d}^\dagger + \hat{a}_{5d}^\dagger)(\hat{a}_{4d}^\dagger - \hat{a}_{5d}^\dagger)^{\frac{n}{2}}|0^0, 0^0\rangle \tag{4.64}$$

These are the "perfect" **L** and **CR** states in the sense of containing equal amounts of trans- and cis- components.

Fig. 4.18 shows the $P(t)$ values for the first 4 picoseconds. Similar results had been obtained by Jacobson *et al.* in Fig. 3 in [83]. In panels (a) and (b), up to N_b =6, the **Trans** and **Cis** states have $P(t) \approx 1$, indicating that these ZOS overtone states will remain localized. At N_b =10, the periodic oscillations become stronger,

[7] A derivation for the **L** state can also be found in § 5.3.2. of [112].

but the recurrences still reach close to 1. The stability appears to be lost for the **Trans** state at N_b =10 and for the **Cis** state at N_b =14. These changes only happen after their respective critical points become unstable in the two bifurcations of Fig. 4.4: $N_b = 8$ for **Trans** and N_b =10 for **Cis**. However, even at $N_b = 22$ their dilution factors are still 0.4 and 0.3 for $|22^0, 0^0\rangle$ and $|0^0, 22^0\rangle$, respectively. Any ZOS in the $[22, 0]^g$ polyad is coupled to the other 71 ZOS. Had the IVR been purely statistical, the dilution factor would have been $\frac{1}{72}$, an order of magnitude smaller than the dilution factors of trans- and cis- overtones. This suggests the vibrational dynamics are far from the RRKM limit, even after then normal modes have been destabilized.

In panels (c) and (d) of Fig. 4.18, before $N_b = 14$ the $P(t)$ evolution of **L** and **CR** states remain strongly oscillating. The almost sinusoidal oscillation between 0 and 1 of **L** and **CR** at N_b =2 is due to the fact that each state there is coupled to another **L** or **CR** states that is degenerate to it. Between N_b =18-22, both **L** and **CR** states have $P(t)$ oscillating slightly under unity. On the bifurcation diagram of Fig. 4.4, this corresponds to ($J_a = 0$) which is where the (EE)-type critical points **L** and **CR** approach their "prefect" shape in the Cartesian coordinates. Hence, quantum wavefunctions localize around these now stable modes. Similar conclusions were reached by Jacobson *et al.* through a visual match between the classical periodic orbits and semiclassical wavefunctions in [66,99].

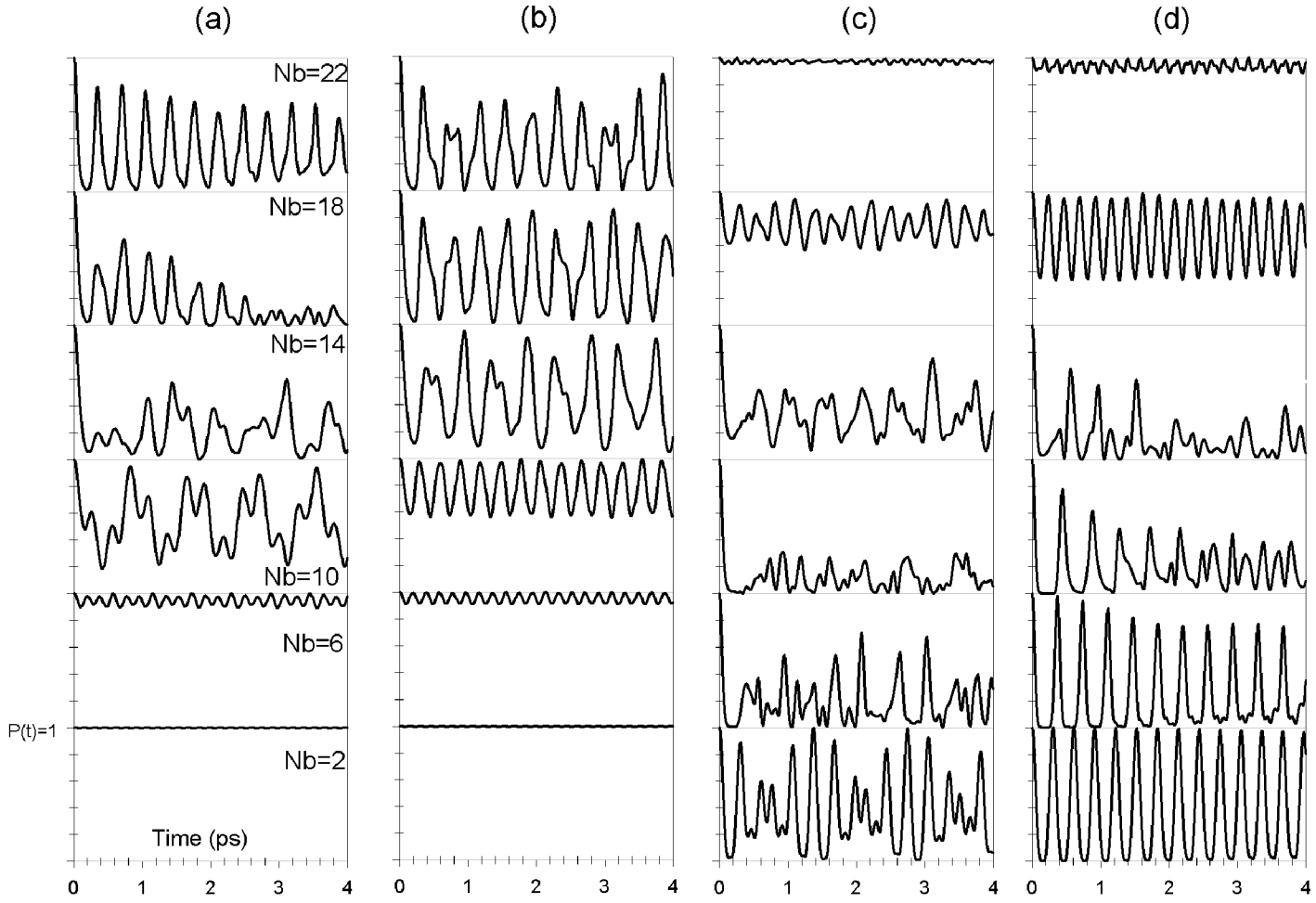

FIGURE 4.18 Survival probability of selected bending states. Panels (a) - (d) display the P(t) of **Trans**, **Cis**, **L** and **CR** states with N_b = 2 - 22, respectively.

The states in Fig. 4.18 with near unity $P(t)$ are in agreement with the (EE)-type critical points found in the classical analysis. They closely resemble the highly excited local bending modes of acetylene [72]. $P(t)$ of **L** states in Fig. 4.18 shows a lack of IVR, which is similar to the behavior of the isomerization states discussed in [106]. The only difference is that the pure bending acetylene states presumably are still below the isomerization barrier. With additional vibrational energy in the stretching DOF, these states or the superposition of several such states will be capable of going back and forth across the barrier many times with clearly non-RRKM dynamics.

4.7 Summary and Conclusion

The critical points analysis is performed on the C_2H_2 pure bending effective Hamiltonian. In the $[N_b, 0]$ polyads, 4 new families of critical points (**L**, **Orth**, **Pre** and **CR**) are born out of the normal **Trans** and **Cis** critical points in distinct bifurcations as N_b is increased. The bifurcation points where the new families are born correspond to qualitative changes in the classical phase space structure. 3-dimensional computer animations give visual insight into the nature of their motions in Cartesian space. Similar bifurcation structure is obtained for the $[N_b, \ell]$ polyads ($\ell = 2, 6, 10$).

Three new types of critical points in $[N_b, 0]$ are consistent with the results of other researchers who had used more elaborate methods. The bi-unstable **Pre**

family, on the other hand, can only be uncovered through an explicit search of critical points like ours, as presented in this thesis.

Separate consideration of the DD-I or ℓ resonances alone qualitatively accounts for the origin and nature of these four new modes. Using the method of § 3.1, the dynamics induced by DD-I or ℓ resonance alone is analyzed. Combining the critical points in the single-resonance Hamiltonians yields the same types of motion as those obtained as critical points in the full bending Hamiltonian.

The calculated quantum survival probability shows the break down of the normal modes description at intermediate polyad, as well as the emergence of local and counter rotator modes as new stable modes of vibration. These results demonstrate that the classical phase space structure is indeed reflected in the dynamics of the corresponding quantum system.

CHAPTER V

BIFURCATION ANALYSIS OF C_2H_2 STRETCH-BEND

5.1 Introduction

Beyond the pure bending subsystem, the next step is extending the critical point analysis to all 7 vibrational DOF of C_2H_2 (4 bending DOF and 3 stretching DOF) explicitly. In such a high-dimensional system, an analytic detection method would be far more superior to both visual inspection and numerical search.

5.1.1 The Effective Hamiltonian

Three stretch-bend effective Hamiltonians of C_2H_2 have been published up to date [89,113,114]. In all of them, the resonance couplings conserve the 3 polyad numbers $[N_{tot}, N_s, \ell]^{g/u}$ in eqns. (4.1).

In this chapter, we use the Hamiltonian of Herman *et al.* from reference [89], since it is the only one whose dynamics has been studied outside the experimental spectra [77,79]. It contains 8 resonances: The Darling-Dennison type $K_{11/33}$ resonance coupling between the two normal C-H stretch modes, the $K_{44/55}$ (DD-I in Chapter 4) between the two normal bending modes, the ℓ resonance r_{45}, and $K_{3/245}$, $K_{1/244}$, $K_{1/255}$, $K_{14/35}$, $K_{33/1244}$ resonances which couple between the stretch and bend DOF. This coupling structure is illustrated in Fig. 5.1. In

a typical stretch-bend polyad, the normal ZOS $|n_1, n_2, n_3, n_4^{\ell_4}, n_5^{\ell_5}\rangle$ are all coupled together by a complex web of resonances in this Hamiltonian. There are only two exceptions. The pure bending polyads analyzed in Chapter 4 form an isolated subsystem. The C-C stretch overtones $|0, n_2, 0, 0^0, 0^0\rangle$ are not coupled by any resonance, therefore they are eigenstates of the effective Hamiltonian.

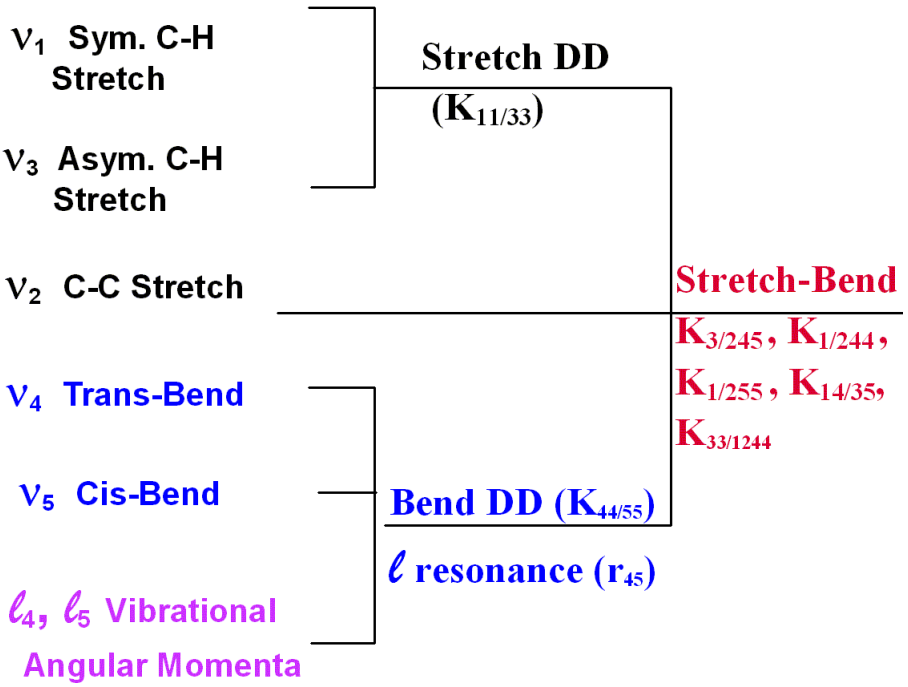

FIGURE 5.1 Resonance couplings in the stretch-bend effective Hamiltonian of [89].

In producing all the effective Hamiltonians in [89,113,114], the fitting is based on only a small part of the states predicted by the polyad model. A high-lying polyad typically contains dozens of states, out of which only a few have been

experimentally detected and included in the fit. This allows for some uncertainty in the high-order coefficients in these fits. Especially lacking are states that contain both stretching ($N_s \geq 1$) excitation and high bending excitation ($n_4 + n_5 \geq 12$).

Using Heisenberg's Correspondence Principle in eqn. (2.11), the 7 DOF quantum Hamiltonian in [89] is transformed to a classical one with 14 action-angle variables: (τ_i, ϕ_i) for $i = 1 - 5$ and (κ_j, χ_j) for $j = 4 - 5$. The actions are related to the zero-order quantum numbers by

$$\tau_i = n_i + \frac{1}{2} \qquad \text{for } i = 1, 2, 3 \tag{5.1}$$

$$\tau_j = n_j + 1 \qquad \text{for } j = 4, 5 \tag{5.2}$$

$$\kappa_k = \ell_k \qquad \text{for } k = 4, 5 \tag{5.3}$$

To simplify our analysis, the last five high-order parameters in Table 5.1: $y_{244}, K_{33/1244}, k_4, r_{445}, r_{545}$ are ignored from all subsequent analysis. The classical Hamiltonian then has the following form [77]:

$$H_{sb} = H_0 + H_v \tag{5.4}$$

with

$$H_0 = \sum_{i=1}^{5} \omega_i \tau_i + \sum_{i,j=1;i\leq j}^{5} x_{ij}\tau_i\tau_j + \sum_{i,j=1;i\leq j}^{5} g_{ij}\kappa_i\kappa_j \tag{5.5}$$

$$\begin{aligned}
H_v =& \frac{K_{1133}}{2}\tau_1\tau_3\cos[2(\phi_1-\phi_3)] \\
&+ \frac{K_{3/245}}{4}\sqrt{\tau_2\tau_3}\{\sqrt{(\tau_4-\kappa_4)(\tau_5+\kappa_5)}\cos[\phi_2-\phi_3+\phi_4-\chi_4+\phi_5+\chi_5] \\
&\quad + \sqrt{(\tau_4+\kappa_4)(\tau_5-\kappa_5)}\cos[\phi_2-\phi_3+\phi_4+\chi_4+\phi_5-\chi_5]\} \\
&+ \frac{K_{1/244}}{2}\sqrt{\tau_1\tau_2(\tau_4^2-\kappa_4^2)}\cos[\phi_1-\phi_2-2\phi_4] \\
&+ \frac{K_{1/255}}{2}\sqrt{\tau_1\tau_2(\tau_5^2-\kappa_5^2)}\cos[\phi_1-\phi_2-2\phi_5] \\
&+ \frac{K_{14/35}}{2}\sqrt{\tau_1\tau_3}\{\sqrt{(\tau_4-\kappa_4)(\tau_5-\kappa_5)}\cos[\phi_1-\phi_3+\phi_4-\chi_4-\phi_5+\chi_5] \\
&\quad + \sqrt{(\tau_4+\kappa_4)(\tau_5+\kappa_5)}\cos[\phi_1-\phi_3+\phi_4+\chi_4-\phi_5-\chi_5]\} \\
&+ \frac{K_{44/55}}{2}\sqrt{(\tau_4^2-\kappa_4^2)(\tau_5^2-\kappa_5^2)}\cos[2(\phi_4-\phi_5)] \\
&+ \frac{r_{45}}{2}\sqrt{(\tau_4^2-\kappa_4^2)(\tau_5^2-\kappa_5^2)}\cos[2(\chi_4-\chi_5)]
\end{aligned} \tag{5.6}$$

The values of the parameters in the above equations are listed in Table 5.1 [1]. The 3 polyad numbers correspond to 3 classical constants of motion:

$$P = 5\tau_1 + 3\tau_2 + 5\tau_3 + \tau_4 + \tau_5 = N_t + \frac{15}{2} \tag{5.7}$$

$$R = \tau_1 + \tau_2 + \tau_3 = N_s + \frac{3}{2} \tag{5.8}$$

$$L = \kappa_4 + \kappa_5 = \ell \tag{5.9}$$

---

[1] It was found later that the $K_{14/35}$ value appear as 29.044 in [89] and 29.944 in [77], which is a minor discrepancy compared to its later revision to 15.66 and 16.614 in [113] and [114], respectively.

TABLE 5.1 C_2H_2 stretch-bend effective Hamiltonian from [89] and published in [77] for the classical Hamiltonian . The parameters are in units of cm^{-1}.

ω_1	3501.537	x_{15}	-10.09	x_{45}	-2.311	$K_{14/35}$	29.944
ω_2	2013.425	x_{22}	-7.802	x_{55}	-2.492	$K_{44/55}$	-12.909
ω_3	3417.644	x_{23}	-5.882	g_{44}	0.4181	r_{45}	-6.09
ω_4	621.692	x_{24}	-12.841	g_{45}	6.603	—	—
ω_5	746.773	x_{25}	-1.829	g_{55}	3.676	y_{244}	0.1522
x_{11}	-24.758	x_{33}	-27.483	$K_{11/33}$	-102.816	$K_{33/1244}$	6.38
x_{12}	-11.199	x_{34}	-10.617	$K_{3/245}$	-16.698	k_4	-1.315
x_{13}	-103.386	x_{35}	-8.676	$K_{1/244}$	6.379	r_{445}	0.1255
x_{14}	-12.98	x_{44}	3.595	$K_{1/255}$	6.379	r_{455}	-0.225

5.1.2 Overview of Existing Studies

To our knowledge, no stretch-bend effective Hamiltonians has been analyzed with all the resonances included. To date we are aware of only three studies of the effective Hamiltonian, all of which are limited either to special cases or by truncation of resonance terms.

- Pals and Gaspard [77] investigated the classical trajectories' recurrences. The study did include the stretching DOF. However, they were mostly focused on the pure bending subsystem, for which the Poincaré surface of section is readily applicable.

- Hasegawa and Someda [79] analyzed the quantum dynamics using a perturbative method. The focus was the short-time evolution of 3 types of

quantum ZOS: $|0,0,0,n_4^0,0^0\rangle$ (part of pure bending subsystem), $|1,3,0,6^0,0^0\rangle$ and $|0,0,n_3,0^0,0^0\rangle$.

- Kellman *et al.* investigated the planar system ($\ell_4 = \ell_5 = 0$) with 3 resonances: $K_{11/33}, K_{3/245}$ and $K_{44/55}$ in a diabatic correlation approach [115]. A series of states termed the "primary subpolyad" are identified, which carries most of the intensity in the experimental spectra. The states are then fit to a single-resonance Hamiltonian, with which the spectral patterns are interpreted.

Due to the dimensionality of the problem, none of these studies explicitly considered all the major resonances in the effective Hamiltonian. In contrast, the approach presented in this thesis is designed to be dimensionality-independent. Therefore we believe it is more suitable for analyzing the stretch-bend acetylene system.

5.2 Preliminary Considerations

In Chapter 4 it was shown that the normal bending modes are destabilized at increased internal energy (polyad numbers) by the resonance couplings, and new stable bending modes are born in the bifurcations. A similar destruction of the normal modes is expected in the stretch-bend system with sufficient excitation and coupling. Independent theoretical investigations such as the PO search by Prosmiti and Farantos [116] also suggest that the highly excited stretch-bend system retains some regularity, which could be caused by new modes of vibration.

5.2.1 The Stretch Overtone Polyads

The critical points analysis starts with solving for all critical points in the 4 DOF (7 DOF - 3 polyad numbers) reduced classical Hamiltonian. In order to obtain preliminary results, we focus on a single series of polyads of interest, as opposed to varying all three polyad numbers $[P, R, L]$ independently.

Of the 5 normal modes of C_2H_2 (see Fig. 4.2), the pure bending subsystem was analyzed in Chapter 4, and the C-C stretch (τ_2) overtones are isolated. This leaves the obvious question: what could happen to the two C-H normal stretches as they are excited to higher energy? Although the C-H stretching dynamics has been actively studied using two-mode models [24,74], their coupling to the other vibrational modes remains little known. This motivates us to investigate the polyad series, which includes the symmetric and antisymmetric C-H stretch overtones:

$$\{\tau_1, \tau_2, \tau_3, \tau_4, \tau_5, \kappa_4, \kappa_5\} = \{\tau_1, 0, 0, 0, 0, 0, 0\}, \{0, 0, \tau_3, 0, 0, 0, 0\} \tag{5.10}$$

Although quantization requires that the action in each mode exceed the zero-order energy ($\tau_i \geq d_i/2$), this constraint is ignored in the current purely classical analysis. The polyads containing them are found by substituting eqn. (5.10) into eqns. (5.7-5.9) to give

$$P = 5R, L = \ell = 0 \tag{5.11}$$

These $[P, R, \ell] = [5R, R, 0]$ polyads are henceforward referred to as the *stretch overtone polyads*. The upper limit of R in this study is set at 8.0, as the effective Hamiltonian in [113] includes up to 6 quanta of C-H overtones excitation ($R = 7.5$).

5.2.2 Stability of the Normal C-H Stretch Mode

The first consideration is the stability of the normal C-H stretch modes. For this purpose, the classical trajectories very close to the normal mode overtones in eqn. (5.10) are integrated. The overtone itself is stable if the deviation of nearby trajectories remains small. The onset of large-amplitude oscillations indicates the destabilization of the corresponding overtone trajectory.

From the results in Fig. 5.2, the symmetric stretch overtone τ_1 remains stable to at least τ_1 =6.5 (n_1 =6). In contrast, the antisymmetric τ_3 overtone is unstable even at $\tau_3 = 1.5$, which corresponds to 1 quanta of n_3 excitation. Two resonances may be responsible for the destabilization of τ_3 overtones: $K_{11/33}$ and $K_{3/245}$.

$K_{11/33}$ Resonance The $K_{11/33}$ single resonance system

$$H_{11/33} = H_0 + \frac{K_{1133}}{2}\tau_1\tau_3\cos[2(\phi_1 - \phi_3)] \tag{5.12}$$

is analyzed for the stretch overtone polyads with the method described in § 3.1, with $m : n = 2 : 2$. After the other actions (τ_2, τ_4 τ_5, κ_4, κ_5) are set to be zero,

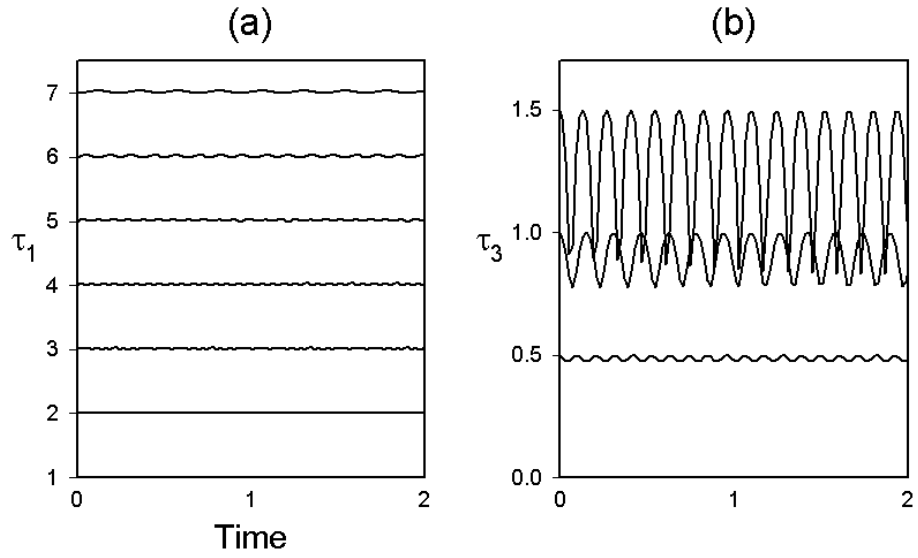

FIGURE 5.2 Classical stability of C-H normal stretch overtones. Panel (a) and (b) are the τ_1 and τ_3 values of trajectories very close to the respective overtone conditions in eqn. (5.10).

(τ_1, τ_3) form a two-mode system with $R = \tau_1 + \tau_3$. The 2 DOF reduced phase space (PPS) are described be canonical variables I_z, ψ:

$$I_z = \frac{\tau_1 - \tau_3}{2}, \qquad \psi = \phi_1 - \phi_3 \tag{5.13}$$

The constant energy contours (at arbitrary energy) of the Hamiltonian in the (I_z, ψ) space are plotted in Fig. 5.3 for R = 2 - 8. Each of these panels is the Mecartor projection of the corresponding PPS, as in Fig. 3.1 (a) of Chapter 3. The contours display the same qualitative features as the semiclassical trajectories. The top and bottom of I_z represent the τ_1 and τ_3 overtones, respectively. The stable critical points at $\psi = 0, \pi$ and 2π are the stable (E) local mode critical points. The points at 0 and 2π are identified with each other, and they are degenerate with the one at π, since the two local C-H stretches are equivalent. The existence

of local C-H stretch in C_2H_2 has been proposed in previous studies of the two coupled C-H stretch oscillators [117].

The horizontal curves at the top of all panels of Fig. 5.3 indicate that the τ_1 overtone is a stable critical point. The τ_3 overtone, in contrast, becomes *unstable* on the PPS from $\tau_3 = 2$ onward. These qualitative results are consistent with the stability observed in Fig. 5.2.

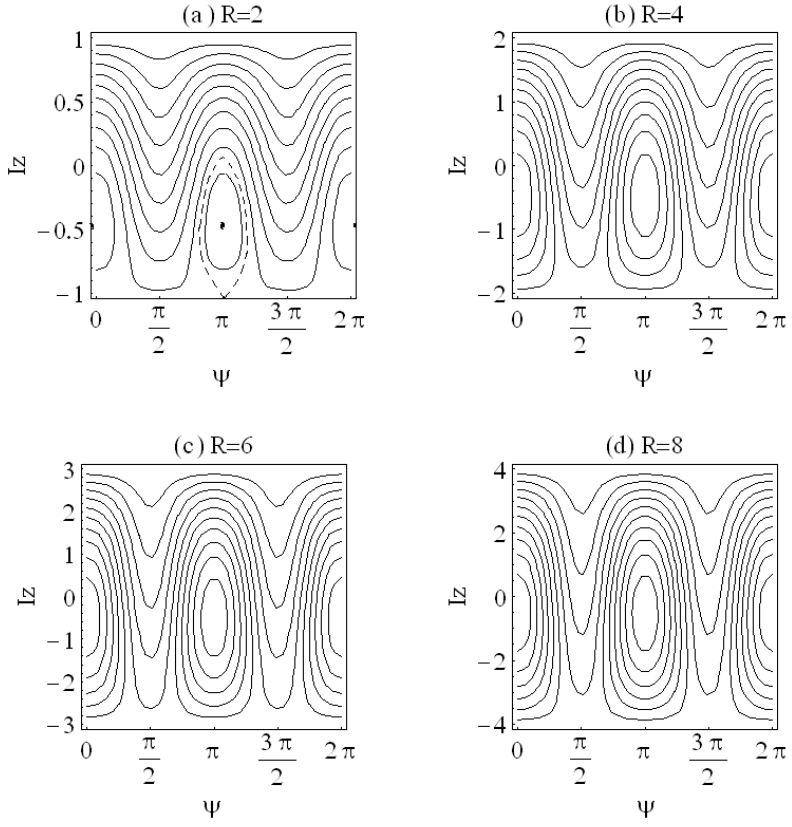

FIGURE 5.3 Phase space structure of single $K_{11/33}$ resonance Hamiltonian, as illustrated by the constant energy contours. In panels (a)-(d) $R = 2$, 4, 6 and 8. The dashed line in panel (a) labels the separatrix crossing the unstable τ_3 overtones, while the black ovals at $\psi = 0, \pi, 2\pi$ indicate the new stable local mode critical point.

$K_{3/245}$ Resonance The classical $K_{3/245}$ resonance system

$$H_{3/245} = H_0 + \frac{K_{3/245}}{4}\sqrt{\tau_2\tau_3}\{\sqrt{(\tau_4-\kappa_4)(\tau_5+\kappa_5)}\cos[\phi_2-\phi_3+\phi_4-\chi_4+\phi_5+\chi_5] + \sqrt{(\tau_4+\kappa_4)(\tau_5-\kappa_5)}\cos[\phi_2-\phi_3+\phi_4+\chi_4+\phi_5-\chi_5]\} \quad (5.14)$$

was formally analyzed by Rose and Kellman in [80]. However they did not give any result concerning the actual parameters in C_2H_2. Here the same type of analysis is carried out for the stretch overtone polyads, with actions (τ_1, κ_4, κ_5) taken to be zero [2]. The τ_3 overtones are then contained in the action space with

$$\tau_2 = \tau_4 = \tau_5 = R - \tau_3 \quad (5.15)$$

Because the derivation in [80] failed to use the proper d_i for the doubly-degenerate bends, the canonical variables (J, φ) [3] of the 2 DOF reduced Hamiltonian are redefined as:

$$J = 14\tau_2 + \tau_3 - 7\tau_4 - 7\tau_5, \qquad \varphi = \phi_3 - \phi_2 - \phi_4 - \phi_5 \quad (5.16)$$

The arbitrary constant energy contours in (J, φ) space are plotted in Fig. 5.4. The top of each panel (maximum J) corresponds to the τ_3 overtones and the bottom to ($\tau_2 = \tau_4 = \tau_5 \neq 0, \tau_3 = 0$). At very low energy, the $K_{3/245}$ resonance induces a bifurcation of the τ_3 overtone, creating a stable critical point at $\varphi = \pi$. However, the overtone itself remains stable at higher R.

---

[2] In [80], the elimination of κ_i from consideration is not rigorous, since the $K_{3/245}$ resonance does couple ℓ_4, ℓ_5, and therefore κ_4, κ_5.

[3] The notations are intentionally different those used in the $K_{11/33}$ case (eqn. 5.13) to avoid confusion.

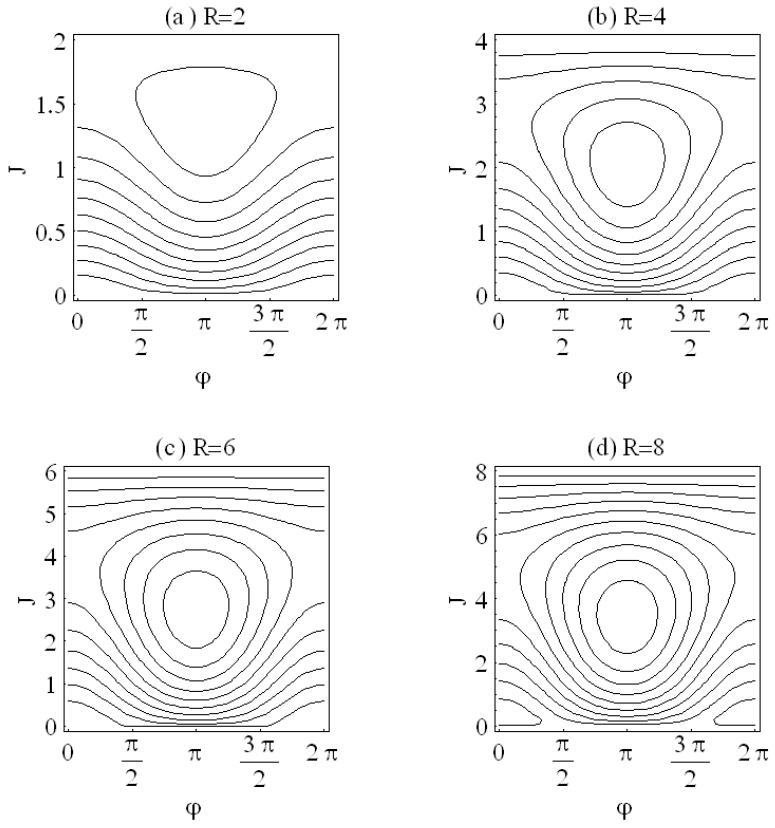

FIGURE 5.4 Phase space portraits of single $K_{3/245}$ resonance Hamiltonian. The contour lines are plotted at arbitrary energy, rather than at the quantized energies for the actual eigenstates. In panels (a)-(d) $R = 2$, 4, 6 and 8.

From the above separate consideration of $K_{11/33}$ and $K_{3/245}$ resonances, below $R = 2$ the $K_{11/33}$ resonance first destabilizes the antisymmetric τ_3 C-H stretch overtones, and the *local* C-H stretch becomes the stable mode of C-H stretch.

5.2.3 Effect of Stretch-Bend Resonances

After its creation, the local C-H stretch mode can be further perturbed by the stretch-bend resonances, and thus coupled to the bending DOF. Of the four stretch-bend resonances ($K_{3/245}$, $K_{1/244}$, $K_{1/255}$ and $K_{14/35}$), it is unlikely that they are all equally important in any given part of a stretch overtone polyad. As a qualitative estimate, we use a simplified version of Chirikov analysis [118]. When κ_4, κ_5 are left out of consideration, the "strength" of each of the 5 resonances (except the ℓ resonance) can be measured by how far the zero-order frequencies $\omega_i = \partial H_0/\partial \tau_i$ are tuned towards the integer ratio m_i which is specified in a given resonance. At the exact integer ratio, ω_i satisfy [119]:

$$\sum_i m_i \frac{\partial H_0}{\partial \tau_i} = 0 \tag{5.17}$$

The vector with integer components $\{m_1, m_2, m_3, m_4, m_5\}$ corresponds to the resonance vectors mentioned in § 2.1. In this case they are:

$$K_{11/33} : \{2, 0, -2, 0, 0\}, \quad K_{3/245} : \{0, -1, 1, -1, -1\}, \quad K_{1/244} : \{1, -1, 0, -2, 0\},$$

$$K_{1/255} : \{1, -1, 0, 0, -2\}, \quad K_{14/35} : \{1, 0, -1, 1, -1\}$$

For each resonance, the center of its resonance zone is a 4-dimensional hypersurface in the $\{\tau_1, \tau_2, \tau_3, \tau_4, \tau_5\}$ space. However because of the conservation of P and R, only 3 of the actions can be independently varied within a polyad. It

is therefore possible to represent these hypersurfaces as 2-dimensional surfaces, which are referred to as *resonance planes* in a 3-dimensional volume (J_1, J_2, J_3)

$$J_1 = \tau_1 - \tau_3 \qquad \in [-R, R] \tag{5.18}$$

$$J_2 = \tau_2 \qquad \in [0, R] \tag{5.19}$$

$$J_3 = \tau_4 - \tau_5 \qquad \in [-2R, 2R] \tag{5.20}$$

which is also constrained by the requirement that all the τ_i are non-negative.

Fig. 5.5 depicts the 2D resonance planes in (J_1, J_2, J_3) that satisfy eqn. (5.17) for each resonance. The panels in this figure indicate that the C-H stretch system (thick line) is first reached by the $K_{11/33}$ resonance plane (red). The $K_{11/33}$ plane is next intersected by the $K_{1/244}$ plane (magenta). The $K_{3/245}$ and $K_{1/255}$ planes are located at the further side of the (J_1, J_2, J_3) space and can only interact with the C-H stretch system via $K_{11/33}$ and other resonance planes. Because the $K_{14/35}$ resonance term vanishes in the absence of bending excitation, the $K_{14/35}$ its plane (navy) also cannot directly interact with the stretch subsystem.

5.3 Critical Points Analysis

Based on the results of § 5.2.2 - 5.2.3, in this subsection we compute critical points in the following three cases:

1. The (τ_1, τ_3) subsystem with $K_{11/33}$ resonance;

2. The $(\tau_1, \tau_2, \tau_3, \tau_4)$ subsystem with $K_{11/33} + K_{1/244}$ resonances;

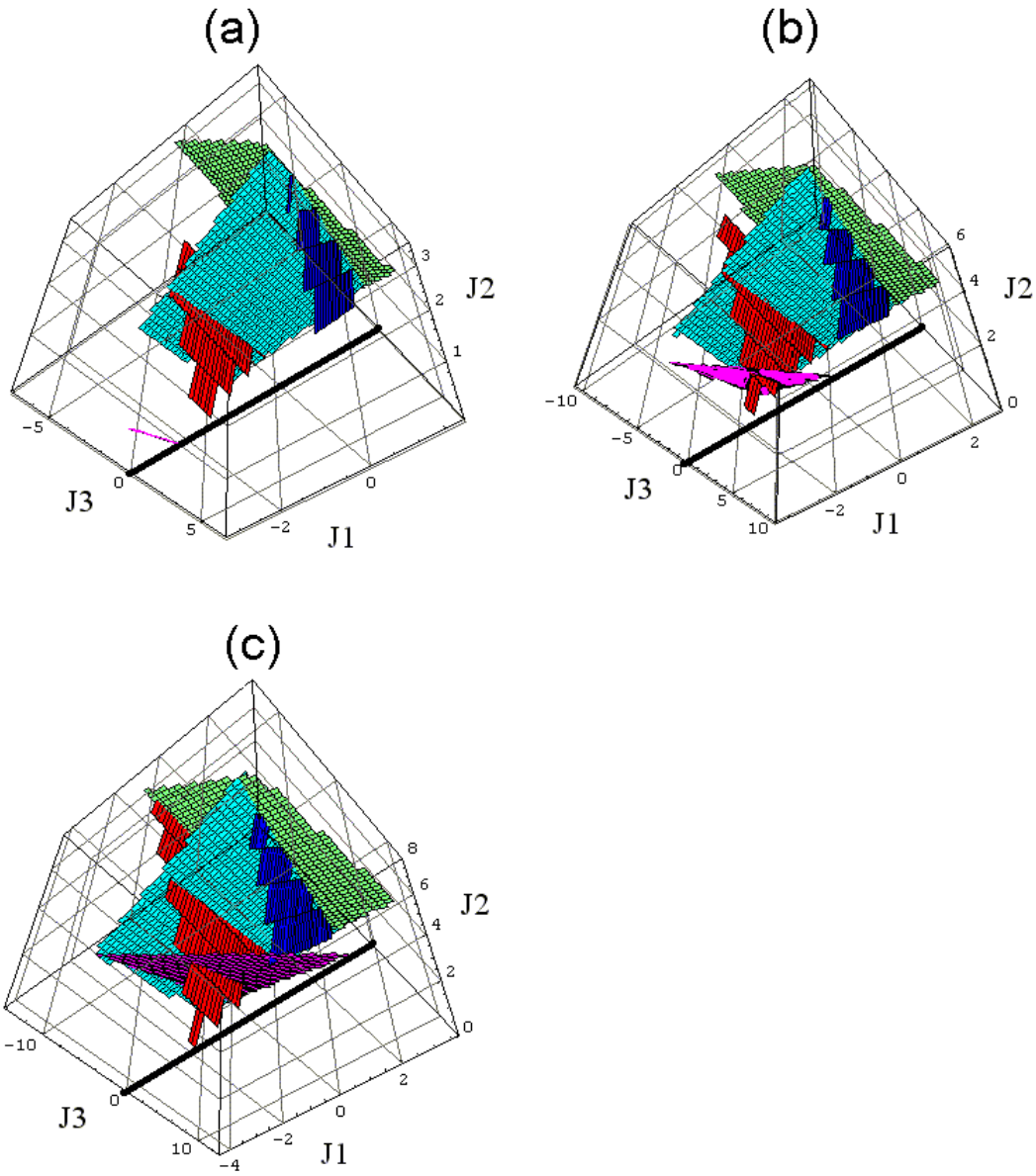

FIGURE 5.5 Frequency resonance planes in stretch overtone polyads. Panels (a), (b) and (c) display the cases with $R = 4$, 6 and 8, respectively. The color coding is: $K_{11/33}$ (red), $K_{3/245}$ (turquoise), $K_{1/244}$ (magenta), $K_{1/255}$ (green), $K_{14/35}$ (navy). The C-H stretch subsystem is indicated by the thick black line.

3. The full H_{sb} of eqn. (5.6) with all 7 resonance couplings.

5.3.1 Computational Details

Using the procedure described in Appendix A, a canonical transformation is selected that expresses the Hamiltonian H_{sb} in the following new action-angle variables: 3 pairs of trivial action-angle variables (P, θ_P, R, θ_R, L, θ_L) for the polyad numbers (defined in 5.7-5.9) and their conjugate angles, and 4 pairs of non-trivial ones (I_1, Ψ_1, I_2, Ψ_2, I_3, Ψ_3, I_4, Ψ_4) which span the 8-dimensional reduced phase space. The angles $\Psi_1 - \Psi_4$ are chosen to correspond to the $K_{11/33}$, $K_{1/244}$, $K_{44/55}$ and ℓ resonances, respectively. The simplest canonical transformation we have found so far is:

$$I_1 = 12\tau_1 + 8\tau_2 + 11\tau_3 + 2\tau_4 + 2\tau_5 + 2\kappa_4 + 2\kappa_5, \qquad \Psi_1 = \phi_1 - \phi_3 \tag{5.21}$$

$$I_2 = 6\tau_1 + 3\tau_+ 6\tau_3 + \tau_4 + \tau_5 + \kappa_4 + \kappa_5, \qquad \Psi_2 = \phi_1 - \phi_2 - 2\phi_4 \tag{5.22}$$

$$I_3 = 6\tau_1 + 4\tau_2 + 6\tau_3 + \tau_4 + \kappa_4 + \kappa_5, \qquad \Psi_3 = \phi_4 - \phi_5 \tag{5.23}$$

$$I_4 = -12\tau_1 - 8\tau_2 - 12\tau_3 - 2\tau_4 - 2\tau_5 - \kappa_4 - 2\kappa_5, \qquad \Psi_4 = \chi_4 - \chi_5 \tag{5.24}$$

Ψ_1 is the relative phase angle between the symmetric τ_1 and antisymmetric τ_3 oscillators. Ψ_3 and Ψ_4 are identical to ψ_a and ψ_b in Chapter 4, respectively.

Critical points in the reduced phase space are defined by:

$$\frac{\partial H_{sb}}{\partial \Psi_1} = \frac{\partial H_{sb}}{\partial \Psi_2} = \frac{\partial H_{sb}}{\partial \Psi_3} = \frac{\partial H_{sb}}{\partial \Psi_4} = 0 \tag{5.25}$$

$$\frac{\partial H_{sb}}{\partial I_1} = \frac{\partial H_{sb}}{\partial I_2} = \frac{\partial H_{sb}}{\partial I_3} = \frac{\partial H_{sb}}{\partial I_4} = 0 \tag{5.26}$$

In eqns. (5.25), Ψ_i only appear in the form of $\cos$ functions. Similarly to the treatment of the pure bending subsystem (§ 4.3.1), a sufficient condition for them to be simultaneously zero is:

$$\begin{aligned}&\sin[2\Psi_1] = \sin[\Psi_2] = \sin[2\Psi_3] = \sin[2\Psi_4] = \sin[\Psi_2 - 2\Psi_3] \\ &\quad = \cos[\Psi_1 + \Psi_3 \pm \Psi_4] \sin[\Psi_1 + \Psi_3 \mp \Psi_4] = \sin[\Psi_1 - \Psi_2 + \Psi_3 \pm \Psi_4] = 0 \end{aligned} \tag{5.27}$$

One can therefore fix Ψ_i to the discrete values satisfying eqn. (5.27), and solve the remaining 4 equations (5.26) only. The latter are first transformed by the following substitution:

$$\begin{gathered} u_1 = \sqrt{\tau_1}, u_2 = \sqrt{\tau_2}, u_3 = \sqrt{\tau_3}, \\ u_4 = \sqrt{\tau_4 + \kappa_4}, u_5 = \sqrt{\tau_4 - \kappa_4}, u_6 = \sqrt{\tau_5 + \kappa_5}, u_7 = \sqrt{\tau_5 - \kappa_5} \end{gathered} \tag{5.28}$$

and then multiplying appropriate factors to remove their denominators. The

result is 7 simultaneous polynomial equations with 7 unknowns $u_1 - u_7$:

$$\sqrt{u_1 u_3}\ \frac{\partial H}{\partial I_1}(u_i) = 0 \tag{5.29}$$

$$\sqrt{u_1 u_2 u_4 u_5}\ \frac{\partial H}{\partial I_2}(u_i) = 0 \tag{5.30}$$

$$\sqrt{u_4 u_5 u_6 u_7}\ \frac{\partial H}{\partial I_3}(u_i) = 0 \tag{5.31}$$

$$\sqrt{u_4 u_5 u_6 u_7}\ \frac{\partial H}{\partial I_4}(u_i) = 0 \tag{5.32}$$

$$5u_1^2 + 3u_2^2 + 5u_3^2 + \frac{1}{2}(u_4^2 + u_5^2 + u_6^2 + u_7^2) = P \tag{5.33}$$

$$u_1^2 + u_2^2 + u_3^2 = R \tag{5.34}$$

$$u_4^2 - u_5^2 + u_6^2 - u_7^2 = 0 \tag{5.35}$$

The unknowns are then solved with *PHCpack* [98].

Treatment of Subsystems When any of the u_i variables vanishes, at least one of eqns. (5.29-5.32) becomes unphysical . This happens when there is zero action in any normal mode τ_i, or when $\tau_j = \pm\kappa_j$.

Special consideration is required for these cases. The contributions from the resonance(s) involved with the vanishing action would also vanish from the Hamiltonian. The equations defining the critical points have to be adjusted accordingly. As an example, in the treatment of H_2O system, the two O-H normal stretch critical point families have no bend action [16]. In deriving these families, the bending-dependent terms including the stretch-bend Fermi resonances have to be removed. Critical points in the resulting 2 DOF subsystem correspond to these normal stretch modes.

In this chapter we only consider the two subsystems outlined at the end of § 5.2.2. In order to locate *all* the possible critical points in the stretch-bend system, theoretically all combinations of $u_i = 0$ have to be considered one by one. In each case, the relevant zero-order and resonance terms in the classical Hamiltonian are removed. A new canonical transformation (Appendix A) may be necessary so that the new angles correspond to the remaining resonances.

5.3.2 Results

The resulting critical points consist of families of curves in the (τ, κ) 7-dimensional action space, parameterized by the polyad number R. Associated with each family is a discrete set of Ψ_i values. Incidentally, all these solutions have $\kappa_4 = \kappa_5 = 0$. Visualizing the rest of the action space $\tau_1 - \tau_5$ is still a challenging task. In Fig. 5.6, we graph them in 5 separate panels with each τ_i versus R separately. Only those with significant τ_i are calculated and displayed here. In the $K_{11/33}$ subsystem, $\tau_2 = \tau_4 = \tau_5 = \kappa_4 = \kappa_5 = 0$. In the $K_{11/33} + K_{1/244}$ subsystem, $\tau_5 = \kappa_4 = \kappa_5 = 0$.

With $R \in [2, 8]$, we found one family for the $K_{11/33}$ subsystem corresponding to the local C-H stretch, two families for the $(\tau_1, \tau_2, \tau_3, \tau_4)$ system, and two families for the full Hamiltonian.

When there is only $K_{11/33}$ resonance coupling (τ_1, τ_3), one family of stable

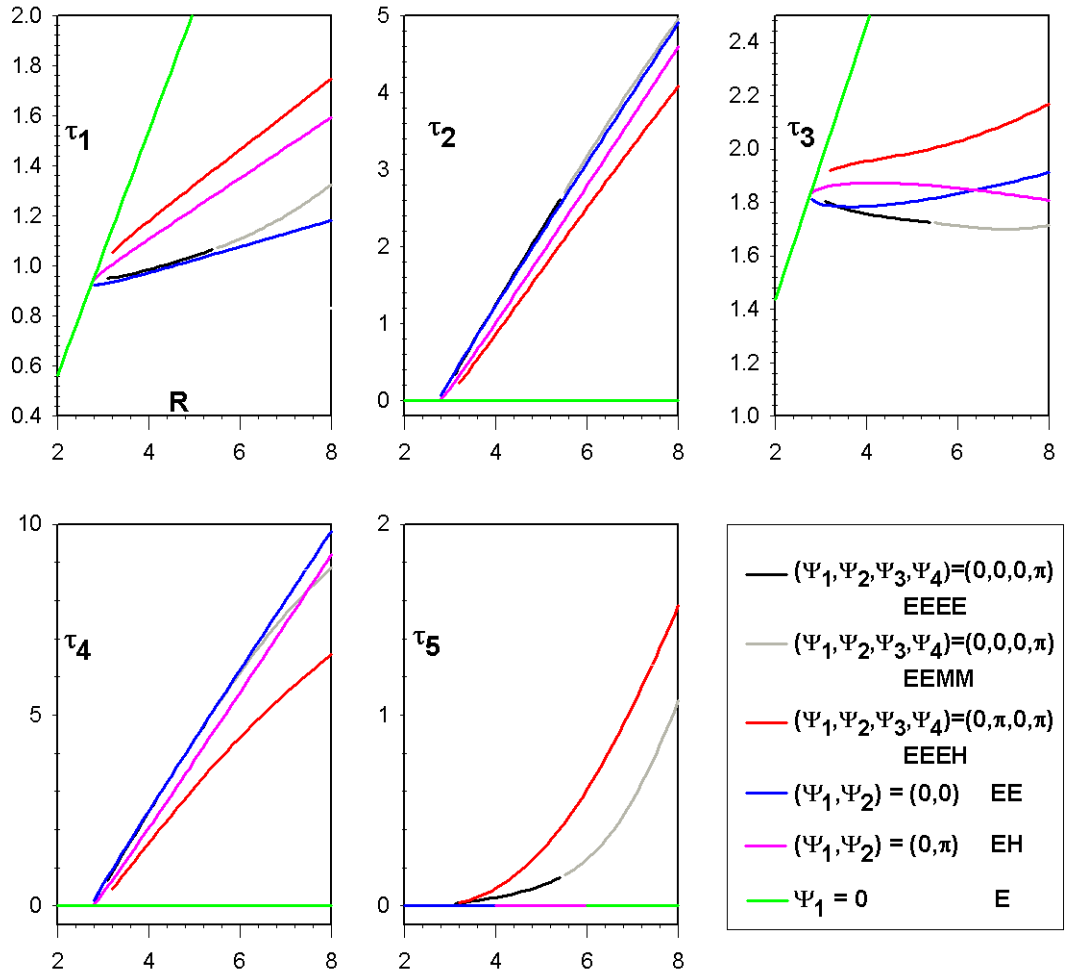

FIGURE 5.6 Families of critical points in stretch overtone polyads $[5R, R, 0]$. Black, grey and red: critical points in H_{sb}. Navy and magenta: the $K_{11/33}+K_{1/244}$ system with $\tau_5 = 0$. Green: The $K_{11/33}$ system, with $\tau_2 = \tau_4 = \tau_5 = 0$.

(E) critical points bifurcates out of the τ_3 overtone. The new family has

$$\Psi_1 = 0 \tag{5.36}$$

which is the local C-H stretch mode indicated on the previous Fig. 5.3.

When both $K_{11/33} + K_{1/244}$ are included and $\tau_5 = \kappa_5 = 0$, the sub-Hamiltonian employs four variables $(I_1, I_2, \Psi_1, \Psi_2)$. Two new families of critical points are created at:

$$(\Psi_1, \Psi_2) = (0, 0), (0, \pi) \tag{5.37}$$

the $(0, 0)$ family has (EE) stability and the $(0, \pi)$ family has (EH) stability. The C-H stretching motion of these critical points is qualitatively like the local C-H stretch motion, because the Ψ_1 value for both families is the same as in eqn. (5.36). The Ψ_2 angle, as the phase angle of a three-mode resonance $K_{1/244}$, is not yet given a clear physical meaning.

In the full H_{sb}, solving the critical point equations (5.29-5.35) results in two more families of critical points with

$$(\Psi_1, \Psi_2, \Psi_3, \Psi_4) = (0, 0, 0, \pi), (0, \pi, 0, \pi) \tag{5.38}$$

Although there is no explicit constraint, both of these families have $\kappa_4 = \kappa_5 = 0$. The $(0, 0, 0, \pi)$ family start with (EEEE) stability and switches to (EEMM) at $R = 5.45$. The $(0, \pi, 0, \pi)$ family has (EEEH) stability for up to $R = 8$. These two families also have the $\Psi_1 = 0$ indicating local-type C-H stretch. The values of two

other angles $\Psi_3 = 0, \Psi_4 = \pi$, according to Table 4.2 of Chapter 4, suggest that the bending motion is of the local type.

A striking feature is that the critical points in both the $K_{11/33} + K_{1/244}$ and full Hamiltonian bifurcate out of the local C-H stretch (green line in Fig. 5.6). The latter then bifurcates out of the τ_3 (antisymmetric C-H stretch) overtones. We believe that the critical points in Fig. 5.6 correspond to novel types of dynamics in the respective stretch overtone polyads.

Unlike the case of $[N_b, 0]$ pure bending polyads, these critical points in the stretch-bend Hamiltonian do not correspond to POs in the full phase space, but quasiperiodic orbits with 3 frequencies:

$$\dot{\theta}_P = \frac{\partial H_{sb}}{\partial P}, \dot{\theta}_R = \frac{\partial H_{sb}}{\partial R}, \dot{\theta}_\ell = \frac{\partial H_{sb}}{\partial \ell} \tag{5.39}$$

This is a direct result of the multiple polyad numbers, as explained in § 3.3.2.

5.4 Summary

A critical points analysis is performed on the C_2H_2 stretch-bend effective Hamiltonian in order to clarify the fate of normal C-H stretch mode under increasing excitation. The preliminary results indicate that the antisymmetric normal C-H stretch -s first destabilized by $K_{11/33}$ resonance to produce the local C-H stretch. Then the local stretch bifurcates into at least 4 families of stretch-bend critical points at higher excitation, with the inclusion of stretch-bend resonances.

Such an observation suggests that the stretch-bend dynamics could be influences by a chain of bifurcations each induced by certain resonances.

We are currently working to clarify the physical meaning of these critical points, and their role in the classical phase space. In addition, a more complete classification, including all the subsystems (combinations of $\tau_i = 0$) is in progress.

CHAPTER VI

CONCLUSIONS AND FUTURE DIRECTIONS

6.1 Conclusions

A generalized method of critical points analysis is proposed for analyzing highly excited intramolecular vibrational dynamics. The classical form of effective Hamiltonian with polyad numbers is canonically transformed to reduce the dimensionality. The critical points in the reduced phase space are systematically found as roots of analytic equations. Their number and stability are followed as the polyad number(s) is varied, forming a bifurcation structure. Critical points with all-stable stability type are expected to indicate regions of regular (quasi-periodic) motion, which correspond to quantum modes of vibration. A change in the number and/or stability of these critical points, called a bifurcation, constitutes the most important invariant structure in phase space. These bifurcations indicate qualitative changes in both the classical and quantum dynamics of the system.

This analysis is carried out in the C_2H_2 pure bending system. Four new families of critical points besides the normal mode ones are found to be born in bifurcations at higher excitation energy. The two bi-stable families **L** and **CR** correspond to the new quantum modes, which dominate the top and bottom

of the polyad after the normal modes are destabilized by the bifurcations. These new families are qualitatively interpreted as superpositions of collective resonance modes caused by DD-I and ℓ resonances acting individually.

Critical point bifurcation analysis is extended to the stretch-bend effective Hamiltonian. Preliminary results are presented and discussed for polyads $[5R, R, 0]$, which contain the stretch overtones. With increasing stretch polyad number R, the antisymmetric C-H normal stretch overtone states are first substituted by the local C-H stretching as the stable mode, in a bifurcation induced by $K_{11/33}$ resonance. Then $K_{1/244}$ resonances and other resonance couplings set in sequentially, creating new families of critical points. These critical points are expected to correspond to novel modes of stretch-bend vibration.

6.2 Summary of Contributions

In this thesis we have

1. Introduced a generalized critical points analysis method that can explore systems beyond the scope of existing methods. The cases with multiple polyad numbers are explicitly considered in the analysis for the first time.

2. Found four important modes of vibration in the acetylene pure bending system, and provided a qualitative explanation in terms of single resonances.

3. Studied for the first time the effect of multiple resonances in the stretch-bend C_2H_2 system. The preliminary critical point analysis suggests a series

of resonances that act sequentially to couple the C-H stretching overtones to the remaining DOF.

6.3 Future Directions

The comprehensive critical points analysis of the full acetylene stretch-bend remains to be finished. Then the critical points could be used to assign the strongly perturbed eigenstates, such as the approximately half of the observed levels in polyads $[4, 20, 0]^{u+}$ and $[5, 25, 0]^{u+}$. These levels appear as neither a normal ZOS, nor attributable to perturbation from a single resonance [113].

The generalized critical points analysis has opened the door to analyzing the dynamics of many more systems with polyad structure. These systems include other C_2H_2 isotopomers, formaldehyde (H_2CO) [120], methane (CH_4) [121] and even myoglobin [122]. The last case suggests that even in large molecules, it is possible for a few coupled modes to be isolated from the rest of the molecule, for a (relatively) prolonged time. These new systems will greatly expand the usefulness of the polyad Hamiltonian model.

New mathematical inquiries also arise from this thesis regarding the mathematical theory of relative equilibria (see § 3.3.3). Most of the relevant mathematical studies up to date consider only rigorously conserved symmetries, such as the angular momentum of an isolated body. However, then considering molecules, because of the approximate nature of the effective Hamiltonian and polyad num-

bers, the structural stability of the dynamical features gleaned from the critical point analysis remain to be clarified. Specifically, it would be of great practical importance to understand how much the real molecular Hamiltonian with relatively small polyad-breaking terms differ in dynamics, compared to those from the polyad Hamiltonian.

APPENDIX A

CANONICAL TRANSFORMATION

This appendix explicitly derives the canonical transformation that results in a reduction of the classical Hamiltonian with polyad number(s). The application of eqns. (2.11) to an N-mode quantum effective Hamiltonian (2.1) results in a classical Hamiltonian with N pairs of action-angle variables (τ_i, ϕ_i)

$$H(\tau_i, \phi_i) = H_0(\tau_i) + H_v(\tau_i, \phi_i) \tag{A.1}$$

Each resonance coupling in H_v can be expressed as an N-vector. Let there be M $(M \leq N)$ resonance vectors that are linearly independent of each other:

$$\vec{V}_i = \{N_{i1}, N_{i2}, \ldots, N_{iN}\} \quad \text{for i=}1, \ldots, M \tag{A.2}$$

There exist a total number of (N-M) polyad numbers ([25] and [26])

$$\vec{P}_j = \{P_{j1}, P_{j2}, \ldots, P_{jN}\} \quad \text{for j=}1, \ldots, (N-M) \tag{A.3}$$

which correspond to vectors perpendicular to all $\vec{V}_i$:

$$\vec{P}_j \cdot \vec{V}_i = 0 \tag{A.4}$$

The next step in simplifying eqn. (A.1) is finding a canonical transformation which (1) linearly combines τ_i into M new actions I_i, and $(N-M)$ polyad

numbers P_j; (2) linearly combines ϕ_i into M angles Ψ_i conjugate to I_i, and $(N-M)$ cyclic angle θ_j. After this transformation, the Hamiltonian has only $2(N-M)$ nontrivial coordinates:

$$H(I_i, \Psi_i) = H_0(I_i, P_j) + H_v(I_i, \Psi_i, P_j) \tag{A.5}$$

This transformation can be expressed in matrix notation as

$$\begin{pmatrix} \Psi_1 \\ \cdots \\ \Psi_M \\ \theta_1 \\ \cdots \\ \theta_{N-M} \\ I_1 \\ \cdots \\ I_M \\ P_1 \\ \cdots \\ P_{N-M} \end{pmatrix} = \begin{pmatrix} A & 0 \\ 0 & B \end{pmatrix} \begin{pmatrix} \phi_1 \\ \cdots \\ \cdots \\ \cdots \\ \cdots \\ \phi_N \\ \tau_1 \\ \cdots \\ \cdots \\ \cdots \\ \cdots \\ \tau_N \end{pmatrix} \tag{A.6}$$

Both A and B are $N \times N$ matrices. The first M rows of A are the $\vec{V}_i$ vectors in eqn. (A.2), while the last $(N-M)$ rows of B are the $\vec{P}_j$ vectors in eqn. (A.3). Using the symplectic formulation of canonical transformations from Chapter 9.3 of [32], we require:

$$\begin{pmatrix} A & 0 \\ 0 & B \end{pmatrix} \begin{pmatrix} 0 & -E_N \\ E_N & 0 \end{pmatrix} \begin{pmatrix} A & 0 \\ 0 & B \end{pmatrix}^T = \begin{pmatrix} 0 & -E_N \\ E_N & 0 \end{pmatrix} \tag{A.7}$$

This can be reduced to the following equations:

$$AB^T = BA^T = E_N \tag{A.8}$$

In solving for the unknown elements in matrices A and B, there are usually more unknowns than the number of independent equations. The transformation then is not uniquely determined.

Nevertheless, the Hamiltonian dynamics cannot be dependent on the choice of coordinate system. Consider a critical point in coordinates (I_i, Ψ_i) where

$$\frac{\partial H}{\partial \Psi_i} = \frac{\partial H}{\partial I_i} = 0 \tag{A.9}$$

In an alternative coordinate system (J_i, Φ_i), the critical point equations can be derived using the chain rule from calculus:

$$\begin{pmatrix} \frac{\partial H}{\partial J_1} \\ \cdots \\ \frac{\partial H}{\partial J_M} \end{pmatrix} = \begin{pmatrix} \frac{\partial I_1}{\partial J_1} & \cdots & \frac{\partial I_M}{\partial J_1} \\ \cdots & \cdots & \cdots \\ \frac{\partial I_1}{\partial J_M} & \cdots & \frac{\partial I_M}{\partial J_M} \end{pmatrix} \begin{pmatrix} \frac{\partial H}{\partial I_1} \\ \cdots \\ \frac{\partial H}{\partial I_M} \end{pmatrix} = 0 \tag{A.10}$$

$$\begin{pmatrix} \frac{\partial H}{\partial \Phi_1} \\ \cdots \\ \frac{\partial H}{\partial \Phi_M} \end{pmatrix} = \begin{pmatrix} \frac{\partial \Psi_1}{\partial \Phi_1} & \cdots & \frac{\partial \Psi_M}{\partial \Phi_1} \\ \cdots & \cdots & \cdots \\ \frac{\partial \Psi_1}{\partial \Phi_M} & \cdots & \frac{\partial \Psi_M}{\partial \Phi_M} \end{pmatrix} \begin{pmatrix} \frac{\partial H}{\partial \Psi_1} \\ \cdots \\ \frac{\partial H}{\partial \Psi_M} \end{pmatrix} = 0 \tag{A.11}$$

The two square matrices are determined by the transformation between (I_i, Ψ_i) and (J_i, Φ_i). Due to eqn. (A.9), the two column vectors in the middle portion of the above two equations would vanish. Therefore the two column vectors on the left, $\left(\frac{\partial H}{\partial J_i}\right)$ and $\left(\frac{\partial H}{\partial \Phi_i}\right)$ must also vanish. This shows the critical points are indeed invariant under an alternative choice of canonical transformation.

Apart from the uncertainty in the canonical transformation, there is also uncertainty in choosing the polyad numbers P_j, which leads to non-unique definition of the cyclic angles θ_j. As an important consequence, the $N - M$ frequencies $\dot{\theta}$ mentioned associated with a critical point (see § 3.3.3) are also arbitrary, as

their values are subject to linear combinations under a different choice of P_j. A preferred definition is not evident from the general consideration [1]. Additional system-specific constraints (such as relating $\dot{\theta}$ variables to the vibrational frequencies in the Cartesian coordinates) are often necessary to address the choice of a non-unique set of action-angle variables.

In summary, when reducing the classical Hamiltonian using the polyad number(s), there are freedom in choosing both the polyad number(s) and the canonical transformation. However, physical behaviors should not be dependent on a particular choice of coordinate system. The above analysis shows rigorously that this is indeed the case: different choices in canonical variables lead to the same critical points in the reduced phase space.

[1]The only exceptions are some trivial cases. For example, if a normal mode i is *uncoupled*, then intuitively ϕ_i is a preferred cyclic variable.

APPENDIX B

TOPOLOGY OF $[N_b, 0]$ PURE BENDING PHASE SPACE

B.1. The Poincaré-Hopf Index Theorem

The *Poincaré-Hopf Index Theorem* [123] was initially proposed by Poincaré and later extended by Hopf. This theorem provides a constraint on the possible combination of the critical points in the reduced phase space. It states that *"The index of a vector field with finitely many zeros on a compact, oriented manifold is the same as the Euler characteristic of the manifold"* [36].

In a Hamiltonian system, the manifold is the phase space while the vector field is the flow generated by the equations of motion. An index g_i is assigned to each critical point (i.e. a zero of the vector field) based on its linear stability. According to the Poincaré-Hopf index theorem, *the sum of all indices g_i is equal to the Euler characteristics χ.* χ is also known as the *topological index* since it is entirely determined by the topology of the manifold.

A critical point is non-degenerate if all eigenvalues of its stability matrix A in eqn. (3.13). At such a point, $g_i = \pm 1$ according to one of the following two equivalent criteria: (1) $(-1)^n$, with n the number of eigenvalues with positive real

part; (2) the sign of the determinant of A. Examples of g_i in 1-3 DOF Hamiltonian systems are listed in Table B.1.

TABLE B.1 Stability index of critical points in 1-3 DOF Hamiltonian systems.

Linear Stability	g_i	Linear Stability	g_i
E	+1	EEE	+1
H	-1	EEH	-1
EE	+1	EHH	+1
EH	-1	HHH	-1
HH	+1	EMM	+1
MM	+1	HMM	-1

On a 2-dimensional manifold, χ is related to the number of "holes" (genus) h on the manifold:

$$\chi = 2 - 2h$$

Therefore a torus (with one "hole") has $\chi = 0$ while a sphere (with no "hole") has $\chi = 2$. The spherical case has been used by the Kellman group to check the consistency of critical points on the polyad phase sphere. It is especially helpful in deducing the stability of critical points at the poles [47]. Fig. B.1 demonstrates this using the PPS of Fig 3.4 of Chapter 2. Spheres 1 and 4 both have two stable critical points, while sphere 3 has 3 stable and 1 unstable (H) critical points. In all three cases, the sum of the stability indices (see Table B.1) equals 2, the topological index of a sphere.

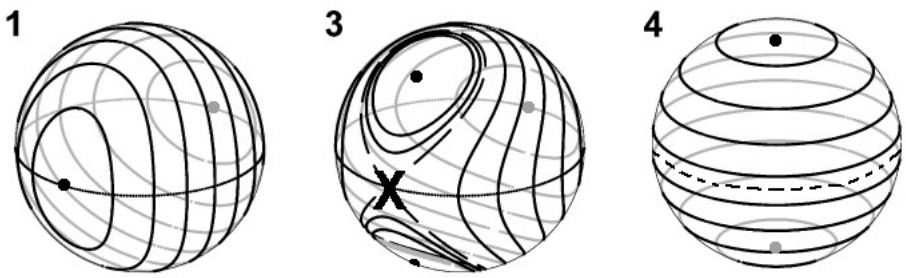

FIGURE B.1 Conservation of topological index on the PPS. The phase spheres are selected from Fig 3.4 of Chapter 3. A large dot indicates a stable (E) critical point and the "X" in sphere 3 indicates an unstable (H) critical point.

The application of the Poincaré-Hopf Theorem to higher dimensional manifolds is challenging, due the lack of means of direct visualization [1]. A few known cases are summarized in Table B.2.

TABLE B.2 Topological indices of 2- and 4-dimensional manifolds, from [125].

Symbol	Manifold	χ
S^2	2-sphere	2
T^2	2-torus	0
S^4	4-sphere	2
T^4	4-torus	4

B.2. Topology of $[N_b, 0]$ Bending Phase Space

This subsection proposes a topological description of the critical points found in the C_2H_2 pure bending polyads $[N_b, 0]$.

[1] An exception is in the 3-dimensional configuration space of *ab initio* electron density, such as in [124].

Currently, there is no sign (such as the display of monodromy [126]) that the topology of C_2H_2 pure bending phase space changes with the polyad number N_b. First, we consider the low polyad end with $N_b \leq 7$, before any bifurcation takes place. At this end, there are no critical points except possibly where $|J_a| + |J_b| = K_a$. In Chapter 4, these locations appear in Figs. 4.10-4.13 as the boundary of the diamond-shaped space. Here this space is schematically illustrated in Fig. B.2, . Because the coordinate system is singular at these locations, the Hamiltonian H_{bend} is transformed to a local-mode representation using the *x-K relationship* described in Chapter 7.6 of [93]. The result is shown in Fig. B.2. It was found that only the four vertices in Fig. B.2 correspond to critical points. Points A and B ($J_a = \pm K_a$, $J_b = 0$) are critical points with (EE) stability; while points C and D ($J_a = 0$, $J_b = \pm K_a$) are critical points with (MM) stability; (3) other points on the boundary are not critical points.

The two $J_b = \pm K_a$ points of (MM) stability correspond to states with maximum ℓ_i in each of the normal mode oscillators: $|(N_b/2)^{\pm(N_b/2)}, (N_b/2)^{\mp(N_b/2)}\rangle$. Since $\ell_i \leq n_i$, there cannot be pure "ℓ_i -overtones" in the form of e.g. the ZOS $|0^{\ell_4}, 0^0\rangle$. These two families of critical points do not participate in the subsequent bifurcations.

At each bifurcation for which $N_b > 0$, the sum of indices will be conserved if (1) each of the classical normal **Trans** and **Cis** motion is doubly-degenerate,

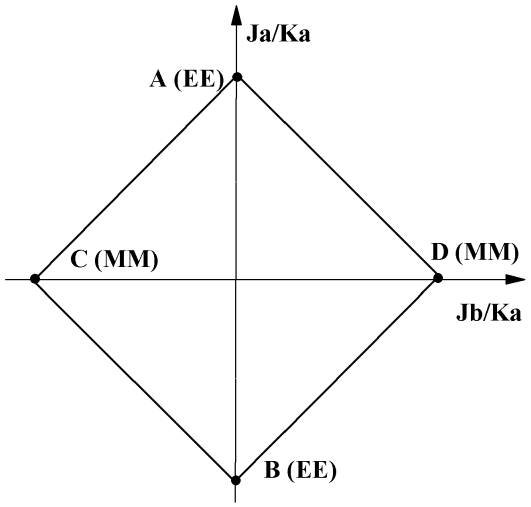

FIGURE B.2 Critical points in $\ell = 0$ bending Hamiltonian at low N_b.

consisting of bending on the x- and y- planes in a given Cartesian coordinate system and (2) the four new families of critical points in Fig. 4.4, each point correspond to four degenerate POs. In classical mechanics, the two carbon and two hydrogen atoms are assumed distinguishable. The quadruply-degenerate POs are related to each other by both a 90^o rotation around the C-C bond and a mirror plane perpendicular to it.

Then the Poincaré-Hopf index theorem can be satisfied in the following manner [2]. Substituting the stability index of each one and their degeneracy into

[2]As points C, D do not participate in the bifurcations, we only consider combinations of the **Trans**, **Cis** against the four new families.

eqns. (4.53), we have before and after each bifurcation:

L, CR: (EE) $\rightarrow$ 4 (EE) + 2(EH) ; $(+2) = 4 \times (+1) + 2 \times (-1)$ (B.1)

Orth: (EH) $\rightarrow$ 4 (EH) + 2(HH) ; $(-2) = 4 \times (-1) + 2 \times (+1)$ (B.2)

Pre: (HH) $\rightarrow$ 4 (HH) + 2(EH) ; $(+2) = 4 \times (+1) + 2 \times (-1)$ (B.3)

Hence in all four bifurcations, the sum of stability indices before and after each bifurcation remains the same.

BIBLIOGRAPHY

[1] J. Kauppinen and J. Partanen. *Fourier Transforms in Spectroscopy*. Wiley-VCH, New York, 2001.

[2] E.B. Wilson Jr., J.C. Decius, and P.C. Cross. *Molecular Vibrations*. Dover, New York, 1980.

[3] D.J. Nesbitt and R.W. Field. Vibrational energy flow in highly excited molecules: role of intramolecular vibrational redistribution. *J. Phys. Chem.*, 100:12735, 1996.

[4] M.M. Law and J.L. Duncan. Anharmonic stretching vibrations expressed as local modes. *Mol. Phys.*, 93:809, 1998.

[5] M.E. Kellman. Algebraic resonance dynamics of the normal/local transition from experimental spectra of ABA triatomics. *J. Chem. Phys.*, 83:3843, 1985.

[6] L. Xiao and M.E. Kellman. Unified semiclassical dynamics for molecular resonance spectra. *J. Chem. Phys.*, 90:6086, 1989.

[7] C. Jung, E. Ziemniak, and H.S. Taylor. Extracting the CH chromophore vibrational dynamics of CHBrClF directly from spectra: Unexpected constants of the motion and symmetries. *J. Chem. Phys.*, 115:2499, 2001.

[8] P.M. Felker and A.H. Zewail. Dynamics of intramolecular vibrational-energy redistribution (IVR). I. Coherence effects. *J. Chem. Phys.*, 82:2961, 1985.

[9] P.J. Robinson and K.A. Holbrook. *Unimolecular Reactions*, chapter 4. Wiley-Interscience, 1972.

[10] B.J. Berne, N. De Leon, and R.O. Rosenberg. Isomerization dynamics and the transition to chaos. *J. Phys. Chem.*, 86:2166, 1982.

[11] P. Brumer and M. Shapiro. *Principles of the quantum control of molecular processes*. Wiley-Interscience, Hoboken, N.J., 2003.

[12] S. Strogatz. The real scientific hero of 1953. *The New York Times Op-Ed*, March 4, 2003.

[13] Y.A. Kuznetsov. *Elements of Applied Bifurcation Theory, Applied Math. Ser., volume 112*. Springer-Verlag, New York, 1995.

[14] T. Poston and L. Stewart. *Catastrophe Theory and Its Applications*. Pitman, London, 1978.

[15] Z. Li, L. Xiao, and M.E. Kellman. Phase space bifurcation structure and the generalized local-normal transition in resonantly coupled vibrations. *J. Chem. Phys.*, 92:2251, 1990.

[16] Z.-M. Lu and M.E. Kellman. Phase space structure of triatomic molecules. *J. Chem. Phys.*, 107:1, 1997.

[17] M.E. Kellman. Dynamical analysis of highly excited vibrational spectra: Progress and prospects. In H.-L. Dai and R.W. Field, editors, *Adv. Ser. Phys. Chem. : Molecular dynamics and spectroscopy by stimulated emission pumping*, volume 4, pages 943–997. World Scientific, Singapore, 1995.

[18] M.E. Kellman. Algebraic methods in spectroscopy. *Ann. Rev. Phys. Chem.*, 46:395, 1995.

[19] M. Joyeux, D. Sugny, V. Tyng, M.E. Kellman, H. Ishikawa, R.W. Field, C. Beck, and R. Schinke. Semiclassical study of the isomerization states of HCP. *J. Chem. Phys.*, 112:4162, 2000.

[20] C.C. Martens and G.S. Ezra. Classical, quantum mechanical, and semiclassical representations of resonant dynamics: A unified treatment. *J. Chem. Phys.*, 87:284, 1987.

[21] C.C. Rankin and M.H. Miller. Classical s matrix for linear reactive collisions of atomic hydrogen + molecular chlorine. *J. Chem. Phys.*, 55:3150, 1971.

[22] C. Jaffé and P. Brumer. Local and normal modes: A classical perspective. *J. Chem. Phys.*, 73:5646, 1980.

[23] S.A.B. Solina, J.P. O Brien, R.W. Field, and W.F. Polik. Dispersed fluorescence spectrum of acetylene from the $\tilde{A}^1A_u$ origin: Recognition of polyads and test of multiresonant effective hamiltonian model for the $\tilde{X}$ state. *J. Phys. Chem.*, 100:7797, 1996.

[24] B.C. Smith and J.S. Winn. The C-H overtone spectra of acetylene: Bend/stretch interactions below 10,000 cm^{-1}. *J. Chem. Phys.*, 89:4638, 1988.

[25] M.E. Kellman. Approximate constants of motion for vibrational spectra of many-oscillator systems with multiple anharmonic resonances. *J. Chem. Phys.*, 93:6630, 1990.

[26] L.E. Fried and G.S. Ezra. Semiclassical quantization using classical perturbation theory: algebraic quantization of multidimensional systems. *J. Chem. Phys.*, 86:6270, 1987.

[27] E.L. Sibert III, W.P. Reinhardt, and J.T. Hynes. Classical dynamics of energy transfer between bonds in ABA molecules. *J. Chem. Phys.*, 77:3583, 1982.

[28] A.B. McCoy and E.L. Sibert III. Quantum, semiclassical and classical dynamics of the bending modes of acetylene. *J. Chem. Phys.*, 105:469, 1996.

[29] D. Sugny, M. Joyeux, and E.L. Sibert III. Investigation of the vibrational dynamics of the HCN/CNH isomers through high order canonical perturbation theory. *J. Chem. Phys.*, 113:7165, 2000.

[30] M. Silva, R. Jongma, R.W. Field, and A.M. Wodtke. The dynamics of "stretched molecules": experimental studies of highly vibrationally excited molecules with stimulated emission pumping. *Ann. Rev. Phys. Chem.*, 52:811, 2001.

[31] M. Tabor. *Chaos and Integrability in Nonlinear Dynamics*. John Wiley and Sons, 1989.

[32] H. Goldstein. *Classical Mechanics*. Addison-Wesley, Reading, MA, 1980.

[33] W. Heisenberg. *Z. Phyz.*, 33:879, 1925. translated in *Sources of Quantum Mechanics*, B. L. van der Waerden Ed. Dover, New York, (1967).

[34] M.S. Child. *Semiclassical Mechanics with Molecular Applications*, chapter 4.2. Oxford: Clarendon Press, New York, 1991.

[35] S. Wiggins. *Global Bifurcations and Chaos, Analytical Methods (Applied Mathematical Sciences, vol. 73)*. Springer-Verlag, New York, 1988.

[36] E.W. Weisstein. *CRC Concise Encyclopedia of Mathematics CD-ROM edition 1.0*. CRC Press, 1999.

[37] J.E. Howard and R.S. MacKay. Calculation of linear stability boundaries for equilibria of Hamiltonian systems. *Phys. Lett. A*, 122:131, 1988.

[38] S.C. Farantos. Exploring molecular vibrations with periodic orbits. *Int. Rev. Phys. Chem*, 15:345, 1996.

[39] S. Keshavamurthy and G.S. Ezra. Eigenstate assignments and the quantum-classical correspondence for highly-excited vibrational states of the Baggot H_2O Hamiltonian. *J. Chem. Phys.*, 107:156, 1997.

[40] M. Henon and C. Heiles. The applicability of the third integral of motion: Some numerical experiments. *Astro. J*, 69:73, 1964.

[41] M. Sutherland. Java applet of Henon-Heiles system. URL: http://thorin.adnc.com/∼topquark/fun/JAVA/henonheiles/henonheiles.html (accessed Oct.14, 2003).

[42] J.W. Helton and M. Tabor. On the classical support of quantum mechanical wavefunctions. *Physica D*, 14:409, 1985.

[43] O. Bohigas, S. Tomsovic, and D. Ullmo. Manifestations of classical phase space structures in quantum mechanics. *Phys. Rep.*, 223:43, 1993. Section 6.2.

[44] W.P. Reinhardt. Regular and irregular correspondences-adiabatic invariants in classical and quantum mechanics. *Prog. Theo. Phys. Supp.*, 116:179, 1994.

[45] E.J. Heller. Bound-state eigenfunctions of classically chaotic Hamiltonian systems: scars of periodic orbits. *Phys. Rev. Lett.*, 53:1515, 1984.

[46] J.M. Gomez Llorente and E. Pollak. Classical dynamics methods for high energy vibrational spectroscopy. *Ann. Rev. Phys. Chem.*, 43:91, 1992.

[47] J. Svitak, V. Tyng, and M.E. Kellman. Bifurcation analysis of higher $m : n$ resonance spectroscopic Hamiltonian. *J. Phys. Chem. A.*, 106:10797, 2002.

[48] J.B. Keller. Corrected Bohr-Sommerfeld quantum conditions for nonseparable system. *Ann. Phys.*, 4:180, 1958.

[49] H. Ishikawa, C. Nagao, N. Mikami, and R.W. Field. Spectroscopic investigation of the generation of "isomerization" states: Eigenvector analysis of the bend-CP stretch polyad. *J. Chem. Phys.*, 109:492, 1998.

[50] J. Svitak, Z. Li, J. Rose, and M.E. Kellman. Spectral patterns and dynamic bifurcation analysis of highly excited vibrational spectra. *J. Chem. Phys.*, 102:4340, 1995.

[51] M.E. Kellman and V. Tyng. Bifurcation effects in coupled Bose-Einstein condensates. *Phys. Rev. A*, 66:013602, 2002.

[52] J.F. Svitak. *Spectral patterns and phase space structure of resonantly coupled molecular vibrations*. PhD thesis, University of Oregon, Eugene, Oregon, 1998.

[53] L. Xiao and M.E. Kellman. Catastrophe map classification of the generalized normal-local transition in Fermi resonance spectra. *J. Chem. Phys.*, 93:5805, 1990.

[54] Z.-M. Lu and M.E. Kellman. Assigning vibrational spectra of chaotic molecules. *Chem. Phys. Lett.*, 247:195, 1995.

[55] J. E. Baggott. Normal modes and local modes in H_2X: beyond the x, K relations. *Mol. Phys.*, 65:739, 1988.

[56] L.V. Vela-Arrevalo and S. Wiggins. Time-frequency analysis of classical trajectories of polyatomic molecules. *Int. J. Bifur. & Chaos*, 11:1359, 2001.

[57] M.M. Guterman and Z.H. Nitecki. *Differential Equations, a first course*. CBS College Publishing, New York, 1984.

[58] R. Abraham and J.E. Marsden. *Foundations of Mechanics, 2nd ed.*, pages 304–308. Benjamin/Cummings, 1978.

[59] M. Krupa. Bifurcations of relative equilibria. *SIAM J. Math. Anal.*, 21:1453, 1990.

[60] G. Gaeta. A splitting lemma for equivariant dynamics. *Lett. Math. Phys.*, 33:313, 1995.

[61] M. Roberts, C. Wulff, and J.S.W. Lamb. Hamiltonian systems near relative equilibria. *J. Diff. Eqn.*, 179:562, 2002.

[62] Ch. van Hecke, D.A. Sadovskii, B.I. Zhilinskii, and V. Boudon. Rotational-vibrational relative equilibria and the structure of quantum energy spectrum of the tetrahedral molecule P_4. *Eur. Phys. J. D*, 17:13, 2001.

[63] I.N. Kozin, R.M. Roberts, and J. Tennyson. Relative equilibria of D_2H^+ and H_2D^+. *Molec. Phys.*, 98:295, 2000.

[64] H.W. Lee. Theory and application of the quantum phase-space distribution functions. *Phys. Rep.*, 259:147, 1995.

[65] G.A. Voth and R.A. Marcus. Semiclassical theory of Fermi resonance between stretching and bending modes in polyatomic molecules. *J. Chem. Phys*, 82:4064, 1985.

[66] M.P. Jacobson, C. Jung, H.S. Taylor, and R.W. Field. State-by-state assignment of the bending spectrum of acetylene at 15,000 cm^{-1}: A case study of quantum-classical correspondence. *J. Chem. Phys.*, 111:600, 1999.

[67] G. Herzberg. *Infrared and Raman Spectra of Polyatomic Molecules*, page 210. Van Nostrand Reinhold Co., New York, 1945.

[68] J. Plíva. Molecular constants for the bending modes of acetylene $^{12}C_2H_2$. *J. Molec. Spectr.*, 44:165, 1972.

[69] E. Abramson, R.W. Field, D. Imre, K.K. Innes, and J.L. Kinsey. Fluorescence and stimulated emission $S_1 - S_0$ spectra of acetylene: Regular and ergodic regions. *J.Chem.Phys.*, 83:453, 1985.

[70] A.B. McCoy and E.L. Sibert III. The bending dynamics of acetylene. *J. Chem. Phys.*, 105:459, 1996.

[71] T.A. Holme and R.D. Levine. Theoretical and computational studies of highly vibrationally excited acetylene. *Chem. Phys.*, 131:169, 1989.

[72] M.P. Jacobson, R.J. Silbey, and R.W. Field. Local mode behavior in the acetylene bending system. *J. Chem. Phys.*, 110:845, 1999.

[73] J.-M. Champion, S. Oss, and M. Abbouti Temsamani. Quantum representations of dynamical systems: new bending modes of acetylene. *Phys. Chem. Comm.*, 3, Article 2, 2000. Online-only journal, Royal Society of Chemistry. URL: http://www.rsc.org/CFmuscat/intermediate_abstract.cfm?FURL=/ej/qu/2000/b001934h/index.htm&TYP=EON (accessed Oct.14, 2003).

[74] K.K. Lehmann. Harmonically coupled, anharmonic oscillator model for the bending modes of acetylene. *J. Chem. Phys.*, 96:8117, 1992.

[75] R. Prosmiti and S.C. Farantos. Periodic orbits and bifurcation diagrams of acetylene/vinylidene revisited. *J. Chem. Phys.*, 118:8275, 2003.

[76] J.P. Rose and M.E. Kellman. Bending dynamics from acetylene spectra: Normal, local, and precessional modes. *J. Chem. Phys.*, 105:10743, 1996.

[77] P. van Ede van der Pals and P. Gaspard. Vibrational time recurrences in a model of acetylene $^{12}C_2H_2$. *J. Chem. Phys.*, 110:5619, 1999.

[78] G. Wu. The influence of the stretch modes on the classical highly excited bend motion with Darling Dennison coupling in acetylene. *Chem. Phys.*, 269:93, 2001.

[79] H. Hasegawa and K. Someda. Derivative state analysis of intramolecular vibrational energy redistribution of acetylene. *J.Chem. Phys.*, 110:11255, 1999.

[80] J.P. Rose and M.E. Kellman. The 2345 multimode resonance in acetylene: A bifurcation analysis. *J. Chem. Phys.*, 103:7255, 1995.

[81] J.P. Rose and M.E. Kellman. Spectral patterns of chaotic acetylene. *J. Phys. Chem. A*, 104:10471, 2000.

[82] J.H. Kiefer, P.S. Mudipalli, A.F. Wagner, and L. Harding. Importance of hindered rotations in the thermal dissociation of small unsaturated molecules: Classical formulation and application to HCN and HCCH. *J. Chem. Phys.*, 105:8075, 1996.

[83] M.P. Jacobson, J.P. O'Brien, R.J. Silbey, and R.W. Field. Pure bending dynamics in the acetylene $\tilde{X}\,^1\Sigma_g^+$ state up to 15,000 cm^{-1} of internal energy. *J. Chem. Phys.*, 109:121, 1998.

[84] N. Chang, M. Shen, and C. Yu. Extended *ab initio* studies of the vinylidene acetylene rearrangement. *J. Chem. Phys.*, 106:3237, 1997.

[85] L. Halonen, M.S. Child, and S. Carter. Potential models and local mode vibrational eigenvalue calculations for acetylene. *Molec. Phys.*, 47:1097, 1982.

[86] D. Xu, G. Li, D. Xie, and H. Guo. Full-dimensional quantum calculations of vibrational energy levels of acetylene (HCCH) up to 13,000 cm^{-1}. *Chem. Phys. Lett.*, 365:480, 2002.

[87] S. Zou, J.M. Bowman, and A. Brown. Full-dimensionality quantum calculations of acetylene vinylidene isomerization. *J. Chem. Phys.*, 118:10012, 2003.

[88] D. Xu, H. Guo, S. Zou, and J.M. Bowman. A scaled *ab initio* potential energy surface for acetylene and vinylidene. *Chem. Phys. Lett.*, 377:582, 2003.

[89] M. Abbouti Temsamani and M. Herman. The vibrational energy levels in acetylene $^{12}C_2H_2$: Towards a regular pattern at higher energies. *J. Chem. Phys.*, 102:6371, 1995.

[90] G. Di Lonardo, L. Fusina, E. Venuti, J.W.C. Johns, M. I. El Idrissi, J. Liévin, and M. Herman. The vibrational energy pattern in acetylene. V. $^{13}C_2H_2$. *J. Chem. Phys.*, 111:1008, 1999.

[91] M. Herman, M.I. El Idrissi, A. Pisarchik, A. Campargue, A.-C. Gaillot, L. Biennier, G. Di Lonardo, and L. Fusina. The vibrational energy levels in acetylene. III. $^{12}C_2D_2$. *J. Chem. Phys.*, 108:1377, 1998.

[92] M. Abbouti Temsamani and M. Herman. Anharmonic resonances in monodeuteroacetylene ($^{12}C_2HD$). *Chem. Phys. Lett.*, 260:253, 1996.

[93] M.P. Jacobson. *Spectroscopic patterns encode unimolecular dynamics*. PhD thesis, Massachusetts Institute of Technology, Cambridge, Massachusetts, 1999.

[94] B.T. Darling and D.M. Dennison. The water vapor molecule. *Phys. Rev.*, 57:128, 1940.

[95] C. Cohen-Tannoudji, B. Diu, and F. Laloë. *Quantum Mechanics, volume 1*, pages 727–741. John Wiley and Sons, New York, 1977.

[96] Mathematica version 4.2. *Wolfram Research Inc.* URL: http://www.wolfram.com/ (accessed Oct.14, 2003).

[97] The content of accompanying CD is also archived on-line at. URL: http://darkwing.uoregon.edu/∼meklab/ (accessed Oct.14, 2003).

[98] J. Verschelde. Algorithm 795 PHCpack: a general-purpose solver for polynomial systems by homotopy continuation. *ACM Trans. Math. Softw.*, 25:251, 1999. URL: http://www.math.uic.edu/∼jan/ (accessed Oct.14, 2003).

[99] C. Jung, H.S. Taylor, and M.P. Jacobson. The acetylene bending spectrum at 10,000 cm^{-1}: Quantum assignments in the midst of classical chaos. *J. Phys. Chem. A.*, 105:681, 2001.

[100] G. Contopolous, S.C. Farantos, H. Papadaki, and C. Polymilis. Complex unstable periodic orbits and their manifestation in classical and quantum dynamics. *Phys. Rev. E*, 50:4399, 1994.

[101] P.A. Patsis and L. Zachilas. Using color and rotation for visualizing four-dimensional Poincaré cross-sections: with applications to the orbital behavior of a three-dimensional Hamiltonian system. *Intl. J. Bifur. & Chaos*, 4:1399, 1994.

[102] D. Jonas. *Spectroscopy of vibrationally hot molecules: hydrogen cyanide and acetylene*. PhD thesis, Massachusetts Institute of Technology, Cambridge, Massachusetts, 1992.

[103] R.L. Hayes, E. Fattal, N. Govind, and E.A. Carter. Long live vinylidene! a new view of the H2C=C: - HCCH rearrangement from *ab initio* molecular dynamics. *J. Am. Chem. Soc.*, 123:641, 2001.

[104] K.M. Ervin, J. Ho, and W.C. Lineberger. A study of the singlet and triplet states of vinylidene by photoelectron spectroscopy of $H_2C{=}C^-$, $D_2C{=}C^-$, and $HDC{=}C^-$. vinylidene acetylene isomerization. *J. Chem. Phys.*, 91:5974, 1989.

[105] T. Carrington Jr., L.M. Hubbard, H.F. Schaefer III, and W.H. Miller. Vinylidene: Potential energy surface and unimolecular reaction dynamics. *J. Chem. Phys.*, 80:4347, 1984.

[106] J. Levin, H. Feldman, A. Baer, D. Ben-Hamu, O. Heber, D. Zajfman, and Z. Vager. Study of unimolecular reactions by Coulomb explosion imaging: the nondecaying vinylidene. *Phys. Rev. Lett.*, 81:3347, 1998.

[107] R. Schork and H. Köppel. Barrier recrossing in the vinylidene-acetylene isomerization reaction: A five-dimensional *ab initio* quantum dynamical investigation. *J. Chem. Phys.*, 115:7907, 2001.

[108] H.K. Srivastava, A. Conjusteau, H. Mabuchi, K.K. Lehmann, G. Scoles, M.L. Silva, and R.W. Field. Rovibrational spectroscopy of the ν =6 manifold in $^{12}C_2H_2$ and $^{13}C_2H_2$. *J. Chem. Phys.*, 113:7376, 2000.

[109] A. Tröllsch and F. Temps. Analysis of vibrationally highly excited bound and resonance states of DCO (X^2A') using an effective polyad Hamiltonian. *Z. Phys. Chem. (Oldenbourg)*, 215:207, 2001.

[110] V. Wong and M. Gruebele. How does vibrational energy flow fill the molecular state space? *J. Phys. Chem. A*, 103:10083, 1999.

[111] W. Siebrand. Recurrence and irreversibility in radiationless transitions. *Chem. Phys. Lett.*, 14:23, 1972.

[112] Z. Duan. *Spectroscopic Study of the acetylene species*. PhD thesis, Massachusetts Institute of Technology, Cambridge, Massachusetts, 2003.

[113] M.I. El Idrissi, J. Liévin, A. Campargue, and M. Herman. The vibrational energy pattern in acetylene (IV): Updated global vibration constants for $^{12}C_2H_2$. *J. Chem. Phys.*, 110:2074, 1999.

[114] K. Hoshina, A. Iwasaki, K. Yamanouchi, M.P. Jacobson, and R.W. Field. The infrared-ultraviolet dispersed fluorescence spectrum of acetylene: New classes of bright states. *J. Chem. Phys.*, 114:7424, 2001.

[115] M.E. Kellman, J.P. Rose, and V. Tyng. Spectral patterns and ultrafast dynamics in planar acetylene. *Eur. Phys. J. D.*, 14:225, 2001.

[116] R. Prosmiti and S.C. Farantos. Periodic orbits, bifurcation diagrams and the spectroscopy of C_2H_2 system. *J. Chem. Phys.*, 103:3299, 1995.

[117] M.S. Child and R.T. Lawton. Local and normal vibrational states: a harmonically coupled anharmonic-oscillator model. *Far. Disc. Chem. Soc.*, 71:273, 1981.

[118] B.V. Chirikov. A universal instability of many-dimensional oscillator systems. *Phys. Rep.*, 52:263, 1979.

[119] D.W. Oxtoby and S.A. Rice. Nonlinear resonance and stochasticity in intramolecular energy exchange. *J. Chem. Phys.*, 65:1676, 1976.

[120] W.F. Polik and J. Ruud van Ommen. The multiresonance hamiltonian model and polyad quantum numbers for highly excited vibrational states. *ACS Symposium Series, Chapter 4*, 678, 1997. American Chemical Socirty.

[121] X.-G. Wang and E.L. Sibert III. A nine-dimensional perturbative treatment of the vibrations of methane and its isotopomers. *J. Chem. Phys*, 111:4510, 1999.

[122] K. Moritsugu, O. Miyashita, and A. Kidera. Temperature dependence of vibrational energy transfer in a protein molecule. *J. Phys. Chem. B*, 107:3309, 2003.

[123] T. Ma and S. Wang. A generalized Poincaré-Hopf index formula and its applications to 2-D incompressible flows. *Nonlinear Analysis: Real World Applications*, 2:467, 2002.

[124] P. Balanarayan and S.R. Gadre. Topography of molecular scalar fields. I. Algorithm and Poincaré-Hopf relation. *J. Chem. Phys.*, 119:5037, 2003.

[125] L. Michel and B.I. Zhilinskii. Symmetry, invariants, topology. I. symmetry, invariants, topology. basic tools. *Phys. Rep.*, 341:11, 2001.

[126] L. Grondin, D.A. Sadovskii, and B.I. Zhilinskii. Monodromy as topological obstruction to global action-angle variables in systems with coupled angular momenta and rearrangement of bands in quantum spectra. *Phys. Rev. A*, 65:012105, 2001.